

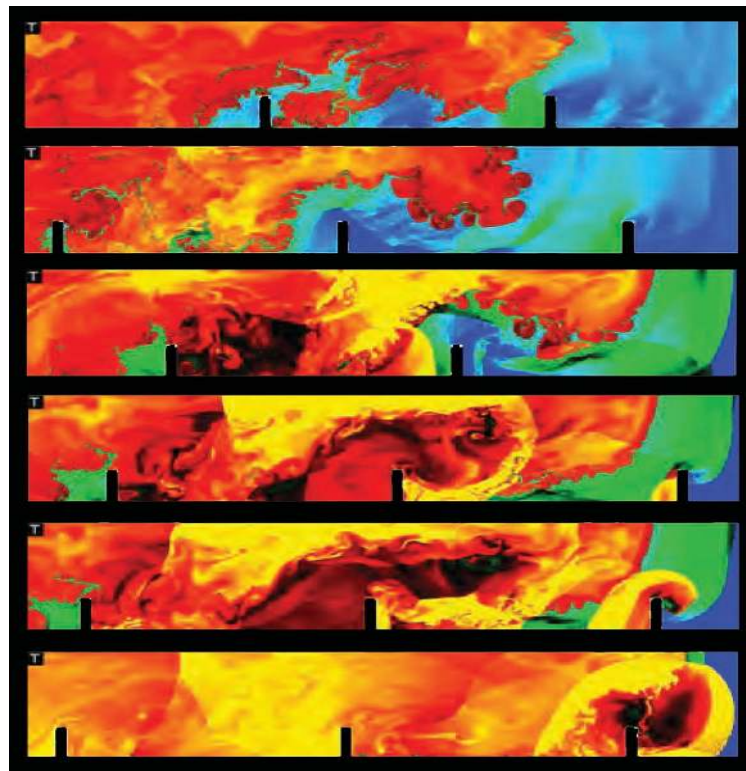


NRL/MR/6400--11-9332

# Deflagrations, Detonations, and the Deflagration-to-Detonation Transition in Methane-Air Mixtures

ELAINE S. ORAN  
VADIM N. GAMEZO  
DAVID A. KESSLER

*Laboratory for Computational Physics and Fluid Dynamics*



April 27, 2011

Approved for public release; distribution is unlimited.

# REPORT DOCUMENTATION PAGE

*Form Approved*  
*OMB No. 0704-0188*

Public reporting burden for this collection of information is estimated to average 1 hour per response, including the time for reviewing instructions, searching existing data sources, gathering and maintaining the data needed, and completing and reviewing this collection of information. Send comments regarding this burden estimate or any other aspect of this collection of information, including suggestions for reducing this burden to Department of Defense, Washington Headquarters Services, Directorate for Information Operations and Reports (0704-0188), 1215 Jefferson Davis Highway, Suite 1204, Arlington, VA 22202-4302. Respondents should be aware that notwithstanding any other provision of law, no person shall be subject to any penalty for failing to comply with a collection of information if it does not display a currently valid OMB control number. **PLEASE DO NOT RETURN YOUR FORM TO THE ABOVE ADDRESS.**

<b>1. REPORT DATE (DD-MM-YYYY)</b> 27-04-2011		<b>2. REPORT TYPE</b> Memorandum		<b>3. DATES COVERED (From - To)</b> March 2008 – February 2011	
<b>4. TITLE AND SUBTITLE</b>  Deflagrations, Detonations, and the Deflagration-to-Detonation Transition in Methane-Air Mixtures				<b>5a. CONTRACT NUMBER</b>	
				<b>5b. GRANT NUMBER</b>	
				<b>5c. PROGRAM ELEMENT NUMBER</b>	
<b>6. AUTHOR(S)</b>  Elaine S. Oran, Vadim N. Gamezo, and David A. Kessler				<b>5d. PROJECT NUMBER</b>	
				<b>5e. TASK NUMBER</b>	
				<b>5f. WORK UNIT NUMBER</b> 64-9633	
<b>7. PERFORMING ORGANIZATION NAME(S) AND ADDRESS(ES)</b>  Naval Research Laboratory 4555 Overlook Avenue, SW Washington, DC 20375-5344				<b>8. PERFORMING ORGANIZATION REPORT NUMBER</b>  NRL/MR/6400--11-9332	
<b>9. SPONSORING / MONITORING AGENCY NAME(S) AND ADDRESS(ES)</b>  National Institute for Occupational Safety and Health Office of Mine Safety and Health Research Pittsburgh Research Laboratory P.O. Box 18070 Pittsburgh, PA 15236				<b>10. SPONSOR / MONITOR'S ACRONYM(S)</b>  NIOSH/OMSHR	
				<b>11. SPONSOR / MONITOR'S REPORT NUMBER(S)</b>	
<b>12. DISTRIBUTION / AVAILABILITY STATEMENT</b>  Approved for public release; distribution is unlimited.					
<b>13. SUPPLEMENTARY NOTES</b>					
<b>14. ABSTRACT</b>  Explosions in mixtures of natural gas (NG) and air have been of intense practical concern for coal mines for many years. Potentially explosive mixtures of NG and air can accumulate in the active ventilated areas or in unventilated sealed areas of these mines. If an ignition source, such as a simple spark, ignites the NG-air mixture and creates a flame, the initially slow-moving flame can become turbulent, accelerate rapidly, develop extremely intense pressure waves, and potentially generate enormous stress on coal mine seals. In this work, we attempt to answer the question: Given a large enough volume of flammable mixture of NG and air, can a weak spark ignition develop into a detonation? Large-scale numerical simulations, in conjunction with experimental work conducted at the National Institute for Occupational Safety and Health's Gas Explosion Test Facility, were performed to address four specific problems: flame acceleration and deflagration-to-detonation transition (DDT) in obstructed channels containing a stoichiometric methane-air mixture, flame acceleration and DDT in fuel-lean and fuel-rich mixtures, effects of spatially varying fuel concentrations on detonations, and stochastic effects on flame acceleration and DDT.					
<b>15. SUBJECT TERMS</b> Detonations      Methane      Deflagration-to-detonation transition Explosions      Coal mines					
<b>16. SECURITY CLASSIFICATION OF:</b>			<b>17. LIMITATION OF ABSTRACT</b>	<b>18. NUMBER OF PAGES</b>	<b>19a. NAME OF RESPONSIBLE PERSON</b>
<b>a. REPORT</b>	<b>b. ABSTRACT</b>	<b>c. THIS PAGE</b>			Elaine S. Oran
Unclassified	Unclassified	Unclassified	UL	124	<b>19b. TELEPHONE NUMBER (include area code)</b> (202) 767-2980

*This work presented in this report was completed under interagency agreement 08FED898342 for the National Institute for Occupational Safety and Health (NIOSH) Office of Mine Safety and Health Research (OMSHR).*

## Contents

Executive Summary . . . . .	E-1
1. Introduction . . . . .	1
Figures 1.1 and 1.2 . . . . .	5
2. Computing Explosions: Background . . . . .	7
2.1. Overview: Evolution of Numerical Methods . . . . .	8
2.2. Previous Numerical Simulations of Coal-Mine Explosions . . . . .	9
2.3. Previous NRL Explosion Simulations: Deflagrations, Detonations, and DDT . . . . .	11
2.3.1. Early Development of Codes: Simulations of Flames and Detonations . . . . .	12
2.3.2. Fundamentals of Deflagration-to-Detonation Transition . . . . .	12
2.3.3. Flame Acceleration and DDT in Channels with Obstacles . . . . .	14
2.3.4. DDT in Large Spaces Containing Obstacles . . . . .	16
2.3.5. Computing DDT: General Observation . . . . .	16
Figures 2.1 – 2.6 . . . . .	18
3. New Results: Flame Acceleration, DDT, and Detonations in Methane-Air Mixtures . . . . .	30
3.1. DDT in Stoichiometric Methane-Air Mixtures (Task 1) . . . . .	28
3.1.1. Development of the Chemical Model: Parameter Calibration . . . . .	28
3.1.2. Description of Numerical Method and Validation of Basic Model . . . . .	33
a. Laminar Flame Structure . . . . .	33
b. Detonation Structure . . . . .	33
3.1.3. Channels with Obstacles . . . . .	36
a. Configuration 7.6 . . . . .	37
b. Configurations 17.4 and 52 . . . . .	38
3.1.4. Sensitivity of the Model to Small Parameter Variations . . . . .	40
Figures 3.1 – 3.16 . . . . .	43
3.2. Stochasticity and Resolution (Task 4) . . . . .	56
3.2.1. Background . . . . .	56
3.2.2. Methane Tests . . . . .	57
a. Laminar Flame Resolution . . . . .	57
b. Background Flow Resolution . . . . .	58
c. Stochasticity, Resolution, and DDT . . . . .	58
Figures 3.17 – 3.20 . . . . .	59
3.3. DDT in Fuel-Lean and Fuel-Rich Mixtures (Task 2) . . . . .	61
3.3.1. Fuel-Lean Model . . . . .	61
3.3.2. Fuel-Rich Model . . . . .	62
3.3.3. Discussion and Other Approaches Under Consideration . . . . .	63
Figures 3.21 – 3.27 . . . . .	65
3.4. Propagation in a Gradient of Fuel Composition (Task 3) . . . . .	69
3.4.1. The Two-Component Model . . . . .	70
a. Calibration for Stoichiometric Mixture . . . . .	71
b. Calibration for Non-Stoichiometric Mixtures . . . . .	72

3.4.2. Detonations in Uniform, High-Activation-Energy Mixtures . . . . .	74
3.4.3. Detonations in a Concentration Gradient . . . . .	76
3.4.4. Conclusions and Future Directions . . . . .	77
Figures 3.28 – 3.42 . . . . .	79
4. Measuring Detonability . . . . .	88
4.1 Background . . . . .	90
4.1.1. Effect of NG Composition on Detonability of NG-Air Mixtures . . . . .	88
4.1.2. Detonability of NG-Air Mixtures . . . . .	89
4.1.3. Experimental Studies of DDT . . . . .	90
4.2. Gas Explosion Test Facility at NIOSH Lake Lynn Laboratory . . . . .	92
4.2.1. Detonation Tube . . . . .	92
4.2.2. Gas Mixing and Analysis . . . . .	93
4.2.3. Ignition . . . . .	94
4.2.4. Baffles . . . . .	94
4.2.5. Diagnostics . . . . .	94
4.2.6. Remote Control System . . . . .	95
Figures 4.1 – 4.4 . . . . .	96
4.3 Interpreting GETF results . . . . .	98
4.3.1. Detonations in NG-Air Mixtures . . . . .	98
4.3.2. DDT in NG-Air Mixtures . . . . .	99
Figures 4.5 – 4.11 . . . . .	100
5. Application to Coal Mining . . . . .	104
5.1. Absolute Detonability . . . . .	104
5.2. Deflagration-to-Detonation Transition . . . . .	105
Figure 5.1 . . . . .	107
6. Future Work . . . . .	108
Acknowledgments . . . . .	110
References . . . . .	111

## Executive Summary

Explosions in mixtures of natural gas (NG) and air have been of intense practical concern for coal mines for many years. Potentially explosive mixtures of NG and air can accumulate in the active ventilated areas or in unventilated sealed areas of these mines. If an ignition source, such as a simple spark, ignites the NG-air mixture and creates a flame, the initially slow-moving flame can become turbulent, accelerate rapidly, develop extremely intense pressure waves, and potentially generate enormous stress on coal mine seals. Recent NIOSH and USACE studies of an explosion at the Sago mine suggested that high pressures and deflagration-to-detonation transition (DDT) can occur in NG-air mixtures in coal mines, and that pressure criteria for seal design may be inadequate.

In this project sponsored by NIOSH-OMSHR, research efforts by NRL focused on a critical, overriding question for coal-mine safety: *Given a large enough volume of a flammable mixture of NG and air, such as may exist in a coal mine, can a weak spark ignition develop into a detonation?*

To address this question, we developed computational models based on the reactive Navier-Stokes equations (RNSE) that can be used to compute combustion waves ranging from low-speed laminar flames, to moderate-speed turbulent flames, to high-speed detonations. The combination of efficient numerical algorithms, adaptive mesh refinement, and one-step reaction kinetics used in these models allows a wide range of scales to be resolved in multidimensional computations. The model parameters were calibrated to reproduce known properties of laminar flames and detonations in various methane-air mixtures, and the RNSE simulations were validated using experimental data on DDT in obstructed channels. The numerical models were used to study four specific problems:

### **1. Flame acceleration and DDT in channels containing a stoichiometric methane-air mixture and obstacles.**

We have shown that it is possible to compute DDT in methane-air mixtures from first principles by solving the RNSE, given enough numerical resolution of critical regions in the system and a chemical model that is valid for the combustion regimes ranging from autoignition to laminar-flame propagation. Flames in obstructed channels accelerate to supersonic velocities and produce shocks. Detonations appear when shocks interacting with obstacles become strong enough to ignite the unburned material. Simulations performed for a number of experimental configurations show good agreement between numerical and experimental results, and thus they can be used as a predictive tool.

### **2. Flame acceleration and DDT in fuel-rich and fuel-lean mixtures in channels with obstacles.**

Simulations performed for rich and lean mixtures showed that the physical events leading to DDT in obstructed channels are essentially the same as those in stoichiometric mixtures. The results show a reasonable agreement with a limited number of available experiments.

### **3. Effects of spatially varying fuel concentrations on detonation propagation.**

A single-step, two-component reaction model for nonuniform methane-air mixtures was developed and used in simulations of a detonation propagating through the concentration gradient in a direction normal to this gradient. The computed reaction-zone structure involved two distinct burning regimes. The leading edge of the reaction zone is an unstable detonation wave with a variable cell size that depends on a local mixture composition. Behind the detonation, the excess fuel and oxidizer that are not

consumed by detonations in rich and lean mixtures, respectively, mix and burn in a turbulent diffusion flame. A series of independent calculations of detonations and flames have been performed to test and validate the single-step, two-component reaction model. We plan to use the same reaction model to study flame acceleration and DDT in mixtures with a nonuniform composition.

#### **4. Effects of stochasticity on flame acceleration and DDT.**

Experimental observations show that DDT is a stochastic process in the sense that there is some uncertainty in time and location for the detonation initiation. In simulations of DDT in obstructed channels, the onset of DDT is also found to vary stochastically, and its location is only predictable with an uncertainty 15-20%, which is about the same as observed in experiments.

The numerical studies were performed by NRL in conjunction with experimental work by NIOSH. The experiments were performed in the Gas Explosion Test Facility (GETF), a new 1.05 m by 72 m detonation tube at the NIOSH Lake Lynn Laboratory. Experiments performed in GETF have now extended the known detonability limits for methane-air mixtures to include mixtures of 5.3% to 15.5% methane in air. They have also shown that DDT can occur in the 1.05 m diameter tube. The NRL team provided expert support for the design and implementation of this facility.

Both computational and experimental studies have made substantial progress toward answering the fundamental question: Is DDT and detonation possible in coal mine tunnels? To provide a definitive, scientifically sound answer, we still need to solve three critical problems:

1. We must prove that numerical models calibrated on small-scale experiments can be extrapolated to the larger geometry of typical coal mine tunnels. Additional validation tests with the 1.05 m tube at NIOSH Lake Lynn Laboratory coupled with a few large scale tests at Lake Lynn Experimental Mine should provide the critical validation data.
2. We must understand and predict flame behavior, DDT and detonation in spatially nonuniform methane-air mixtures that are likely to form in real-life situations.
3. We must understand the mechanism for DDT in smooth channels, which has been observed in experiments but has not been computed with current models, and remains a key unresolved problem in combustion.

## 1. Introduction

Explosions in mixtures of natural gas (NG) and air have been the subject of intense practical concern for many years. Such explosions occur naturally in coal mines where NG accumulates, and accidentally when vessels or pipelines containing NG or liquid NG are ruptured. Thus, maintaining safe conditions in mines and in the processes of extracting, handling, and transporting NG is of major importance to our health and economy. Care must therefore be taken to define and avoid conditions which can lead to these explosions. There are many reviews and references to these types of large-scale explosions (see, for example, [1–4]), and these explicitly show the explosive dangers of NG and other fuels.

Large-scale, gaseous explosions, either natural or accidental, lead to destructive scenarios for which we pay heavily in lives and property. Consider some of the recent large-scale events that we have read and heard about in the media. In 2006, the explosion in the Sago Mine trapped thirteen miners for two days, and only one survived. That same year, there was an explosion in a fuel storage plant in Buncefield, UK, which was heard as far as 20 miles away. Because this explosion occurred late at night, there were only few people in the immediate vicinity and, miraculously, no loss of life. The cost in property and damages in the plant and surrounding houses exceeded a billion dollars. In 2010, there was a large explosion, heard ten miles away, in a power plant being constructed in Middletown, Connecticut. This cost lives, injured many, and cost millions of dollars in damages.

NG explosions, are extremely complex events. In coal mines, explosions can result from ignition of NG accumulated in unventilated, sealed areas. In time, the NG mixes with the ambient air and forms a flammable mixture. It might only take a small spark to ignite NG and create a flame, which then interacts with its environment, accelerates, generates high pressures, and may eventually lead to a detonation. Figure 1.1 (which is discussed more thoroughly in Section 3 of this report) shows how this can occur in a methane-air mixture. The small flame naturally becomes turbulent as it generates pressure waves that reflect from walls of the confining chamber. Eventually, shock waves arise as these waves coalesce, and these continue to interact with the walls and obstacles to create a violent system of shock waves and flames. This complex is a precursor to the formation of a detonation through a process called DDT, the deflagration-to-detonation transition. The most violent type of a steady combustion wave, a detonation, consists of interacting shock waves whose velocities and structure are determined by closely coupled and intense chemical energy release. Detonations are significantly more powerful than flame-generated shocks that occur earlier before the transition. *In summary, the result of a simple spark can be a violent deflagration driving shocks or even more violent detonation waves. Impacts from inert shocks produce high pressures on surrounding walls, and even higher pressures can be generated by detonation impact.*

Thus a simple spark can, in principle, lead to a series of combustion waves and transitions among them that result in enormous stress on internal mine structures, such as the protective seals designed to contain natural gas in unused portions of the mine. For this reason, the possible occurrence of DDT and a detonation in a coal mine must be carefully and scientifically evaluated and understood. The DDT process itself must be understood. We will need to readjust the current small-scale notions of methane detonability to large-scale actualities of confined NG explosions.

Most recently, NIOSH IC9500 [1] examined the fundamental question: *Can high pressures, DDT, or detonations develop in various NG-air mixtures, and what factors control this development?* This report presented results of thermodynamic calculations performed to establish bounds on explosion pressures that can develop from ignition of an explosive NG-air mixture in mine tunnels. It also used empirical rules to establish conservative estimates of the run-up length or distance from ignition point to DDT for an explosion in a mine tunnel. The report also described basic gas-explosion modeling, using commercially available software, which provided information on the pressure-time history that could develop from a NG-air explosion. These models, however, did not contain enough detail to capture the dynamical range of the DDT process or predict detonations, nor could they correctly capture the highest-pressure blast or shock waves. Nevertheless, they were correct in indicating that very high pressures have developed, and this was consistent with the thermodynamic calculations. Another group of studies calculated explosion pressures created by increasingly large explosions of mixtures of NG and air that could form directly behind a leaking seal. None of the codes were designed to be able to predict DDT. They provided guidance for monitoring and establishing the allowable amount of explosive mix that can exist behind a seal of given strength, without taking into account the possibility of detonations.

NIOSH IC9500 led to several critical observations and recommendations. In summary:

1. A detailed picture of the temporal and spatial evolution of the pressure within a typical mining environment did not exist, and the situation was particularly true for environments in which a transition from a deflagration to a detonation (DDT) can occur.
2. DDT was not yet fully understood for conditions typically encountered in mine tunnels.
3. It is important to take action to understand how detonations may arise, quantify their dangers as accurately as possible, and use this information to determine guidelines for protecting mining personnel and the mines themselves.
4. We would like to be able to detect the danger through monitoring before an explosion occurs and take action to mitigate this threat.

Based on these issues and observations, the Laboratory for Computational Physics and Fluid Dynamics (LCP&FD) at the US Naval Research Laboratory (NRL), in close coordination with the NIOSH, OMSHR (*National Institute for Occupational Safety and Health, Office of Mine Safety and Health Research*) undertook an effort to address some of the basic questions of ignition, flame acceleration, and possible DDT in scenarios relevant to coal mines. In the fifteen years prior to the work reported here, researchers in LCP&FD developed a series of numerical simulation tools for describing the behavior of gas-phase explosions and the transition to detonation from first principles. Application of these tools, in conjunction with carefully performed laboratory experiments, has both validated these models as predictive tools and created a body of new knowledge on the behavior of explosions in gaseous fuels. An important component for success in this earlier work was the close ties maintained between experiments and simulations.

Early numerical studies using the LCP&FD capabilities showed how flames in low-pressure mixtures of acetylene or ethylene and air can accelerate and become turbulent due to repeated shock interactions, and how DDT can occur in fuel-air systems. Studies were also performed to uncover the effects of boundary layers and wakes on flame acceleration and possible DDT. All of these early simulations were based on actual laboratory experiments performed at the detonation research facility at the University of Wales at

Aberystwyth, UK, and they had the remarkable result of teaching us fundamental mechanisms and explaining experimental phenomena that were not previously understood. A summary review of the work done up until 2003 is given in [5].

Between 2003 and 2008, the LCP&FD research in flame acceleration and DDT was focused on simulating hydrogen explosions, specifically, the development and acceleration of flames and the transition to detonations in channels with obstructions. The purpose of this work was to produce guidelines for safe design of hydrogen storage facilities. A partial summary of the results of this work is given in [6–8]. An important aspect of the hydrogen-fuel study was the comparison between the calculations and experiments, which were carefully designed to describe the same gases and have the same geometrical configurations. The numerical simulations compared well with experiments and provided many insights into flame development and acceleration, DDT, and detonations in obstructed channels. The geometries considered, an example of which is given in Figure 2.1, are relevant to the problem of explosions in mine tunnels if the gas were changed to NG-air and the size could be scaled up appropriately. This background numerical development is summarized in more detail in Section 2 of this report.

In the three years of the current project with NIOSH, LCP&FD personnel have focused on developing and using numerical and experimental technologies that allow us to address critical questions related to NG explosions in coal mines. In particular, there is the overriding question:

*Given a large enough volume of a flammable mixture of NG and air, such as may exist in a coal mine, can a weak spark ignition develop into a detonation?*

The implications of an answer such as “yes,” or even “sometimes,” means that we could be seriously underestimating the pressures that can develop after an explosion in a mine tunnel. To address this question and its implications, LCP&FD has worked on two major tasks, one involving numerical simulation and the other in supporting the design and implementation of a new experimental test facility.

The work in numerical simulation has focused on the development and evolution of explosions in scenarios appropriate to those in mine tunnels. We consider methane, a primary component of NG, which itself can vary in composition and contain anywhere from 0.5–8% of higher hydrocarbons (HHC). A few percent of HHC can make NG easier to ignite and explode. At this stage of the model development and testing, however, we are considering NG and methane to be the same. In this work, we often refer to NG-air mixtures as methane-air mixtures. Then the specific tasks included in this work are:

1. Develop and test a model for stoichiometric methane-air combustion. Perform a series of simulations of flame propagation, acceleration, and possible DDT in channels with obstacles.
2. Develop and test similar models for fuel-rich and fuel-lean combustion.
3. Examine the effects of spatially varying fuel concentrations in a simulation.
4. Document the effects of stochasticity, i.e., examine how large-scale uncertainty in system behavior caused by minute perturbations in initial conditions or numerical procedures, affect flame acceleration and DDT.

Thus, as part of this effort, we developed appropriately simplified reduced chemical-diffusion models that are necessary for large-scale multidimensional unsteady numerical simulations. These models were then used to perform benchmark computations of the flame evolution to supersonic deflagrations, and, if appropriate,

detonations in methane-air mixtures. Computational results were compared with pre-existing experimental data. Results and interpretations of these simulations are described in detail in a number of published works [9–13] and in subsequent sections of this report.

The experimental effort required close coordination between LCP&FD personnel and NIOSH engineers in order to design and use the new explosion tube at Lake Lynn Laboratories (LLL). This is currently the largest operational test facility for NG explosions [14]. Its successful construction required design of new mixing, diagnostic, and ignition systems. Its use, to date, has led to important, new results concerning the detonability of large volumes of NG-air mixtures. More details of the operation, tests, and implications of these results will be discussed in Section 4 of this report.

We have shown that the complexity and scale of a NG explosion preclude us from having any analytic or simplified theoretical analysis of the complete explosion process, from initiation through to possible DDT. It is also difficult, dangerous, and extremely expensive to study large-scale explosions in a controlled, experimental environment. Because of the practical consequences of both unwanted and purposeful explosions, we must take advantage of every available tool we have for studying and explaining explosions. We must combine numerical simulations with carefully designed experiments and analyses, both to understand and then to use what we have learned about explosions to design safe and efficient systems. This report summarizes the work done by NRL and OMSHR to date to create a reliable, predictive capability.

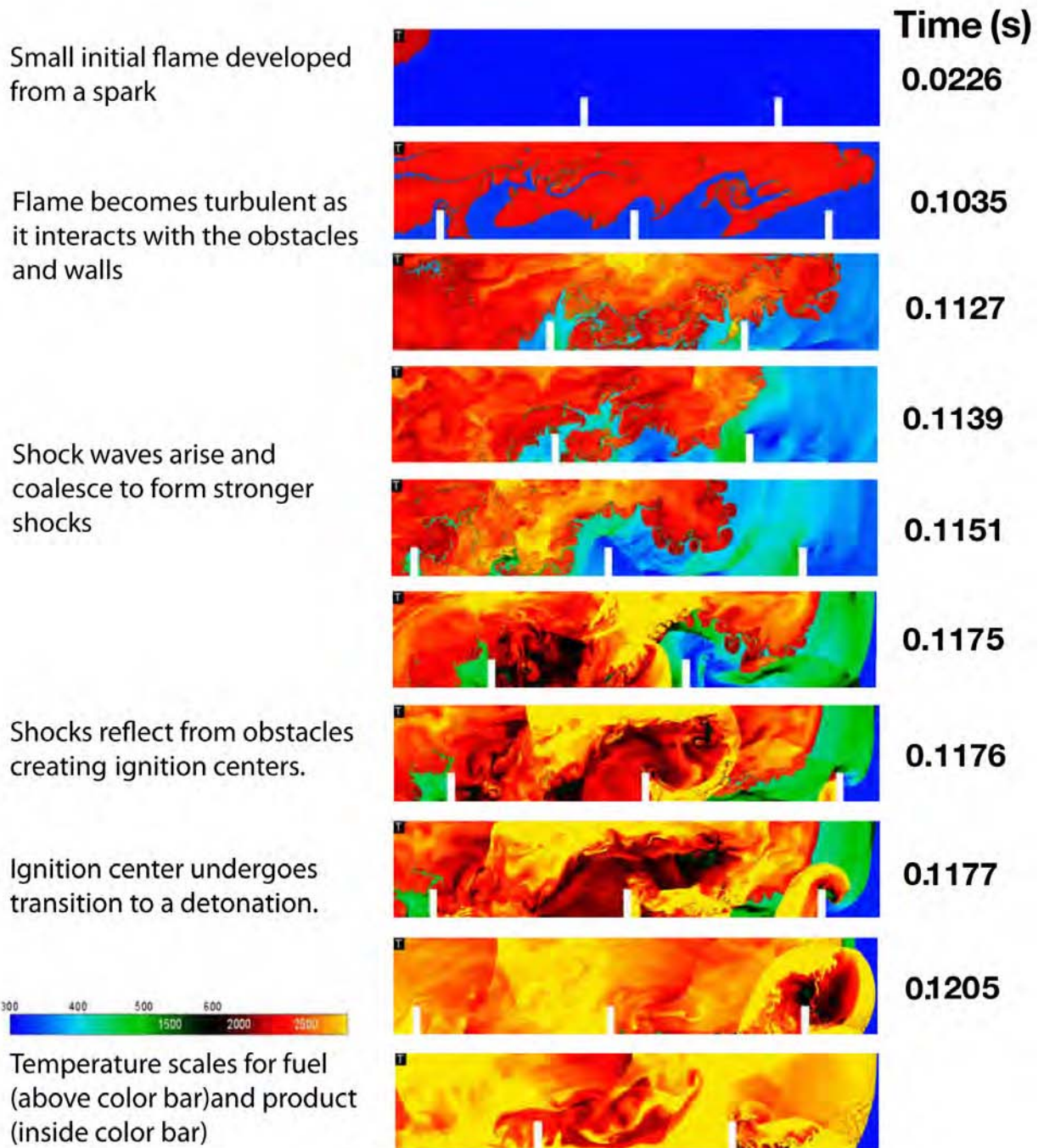


**Figure 1.1.** Computed flame evolution in an obstructed channel filled with a stoichiometric methane-air mixture [9]. Each frame is a window 102 long cm by 26 cm high. The window moves through the system to follow the reaction front and the flames and shocks directly behind it. The height of the channel is  $d = 52$  cm, so that the half-channel height used to define the computational domain of the simulation is  $d/2 = 26$  cm. The blockage ratio is defined as  $BR = 2h/d$ , where  $h$  is the height of an obstacle and  $d$  is the height of the channel. Here  $BR = 0.3$ .

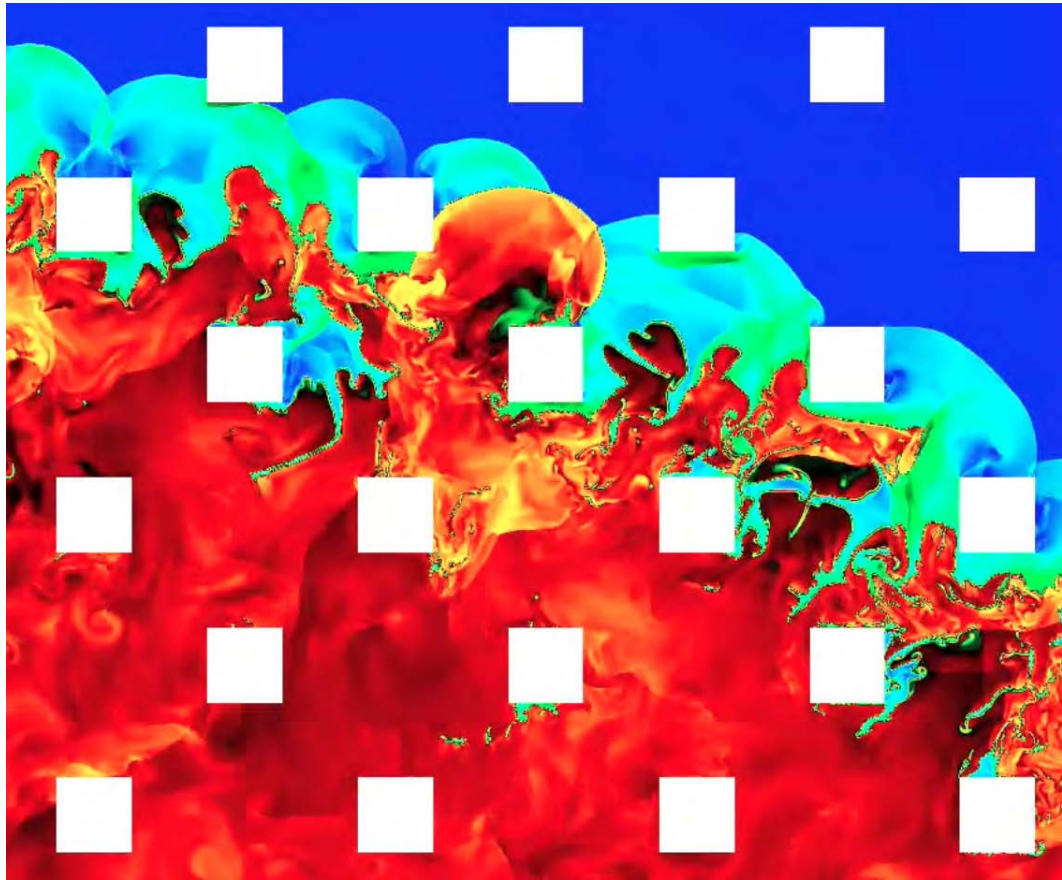


**Figure 1.2.** This is an illustration taken from a computation of the deflagration-to-detonation transition, or DDT, occurring in array of obstacles surrounded by a stoichiometric mixture of hydrogen and oxygen at atmospheric temperature and pressure [8]. Each obstacle is 1 cm in each direction. The background is in dark blue. The leading shocks (light blue) are followed by a turbulent flame. See Figure 2.6 for more details.

## 2. Background: Computing Explosions

Two of the fundamental questions of numerical simulation are: How do we solve the governing equations? How well are we solving them? We generally agree that descriptions of explosions in normal atmospheres require a solution of the unsteady Navier-Stokes equations (NSE) with some representation of the energy-release process. We refer to these coupled fluid-chemical equations as the reactive Navier-Stokes equations (RNSE), which we write here as

$$\frac{\partial \rho}{\partial t} + \nabla \cdot (\rho \mathbf{v}) = 0, \quad (2.1)$$

$$\frac{\partial (\rho \mathbf{v})}{\partial t} + \nabla \cdot (\rho \mathbf{v} \mathbf{v}) + \nabla P + \nabla \cdot \hat{\boldsymbol{\tau}} = 0, \quad (2.2)$$

$$\frac{\partial E}{\partial t} + \nabla \cdot ((E + P)\mathbf{U}) + \nabla \cdot (\mathbf{v} \cdot \hat{\boldsymbol{\tau}}) + \nabla \cdot (K \nabla T) + \rho q \dot{\Omega} = 0, \quad (2.3)$$

$$\frac{\partial (\rho Y)}{\partial t} + \nabla \cdot (\rho Y \mathbf{v}) - \nabla \cdot (\rho D \nabla Y) - \rho \dot{\Omega} = 0, \quad (2.4)$$

These equations describe the conservation of total mass, momentum, and energy, and the balance of chemical species. Here  $\rho$  is the mass density,  $\mathbf{v}$  is the fluid velocity,  $P$  is the pressure,  $E$  is the energy density,  $\dot{\Omega}$  is the reaction rate,  $q$  is the total chemical energy release,  $K$  is the thermal conduction coefficient,  $Y$  is mass fraction of fuel,  $D$  is the mass diffusion coefficient, and  $t$  is time. The viscous stress tensor  $\hat{\boldsymbol{\tau}}$  is defined as

$$\hat{\boldsymbol{\tau}} = \rho \nu \left( \frac{2}{3} (\nabla \cdot \mathbf{v}) \mathbf{I} - (\nabla \mathbf{v}) - (\nabla \mathbf{v})^\dagger \right) \quad (2.5)$$

where  $\nu$  is the kinematic shear viscosity,  $\mathbf{I}$  is a unit matrix, and superscript  $\dagger$  indicates matrix transposition.

To close this set of equations, we must add the equation of state and the definition of  $\dot{\Omega}$ . The chemical reaction rate can be described by a complex set of coupled partial differential equations representing the conversion of reactants into products and the energy release, or it can be approximated by a single-step model with only one equation.

What differs among the various explosion codes is complexity of the chemical model and the equation of state, the method of solution of RNSE, how this method is implemented in the code and computer, how different terms in the equations are coupled, and how complicated geometry and numerical resolution issues are handled. The requirements for solution of RNSE in various regimes of explosions are described below in more detail.

The material presented in this section is divided into three parts. First, we give the necessary background for understanding the evolution and development of numerical methods that are applicable for simulating explosions. This will also introduce some of the necessary computational terminology and concepts used subsequently in this report. Second, we describe three numerical models used previously to simulate coal mine explosions, and discuss their capabilities and limitations for computing the full range of explosion stages. Finally, we summarize the NRL background in developing and using models for numerical simulation of high-speed reactive flows.

## 2.1. Overview: Evolution of Numerical Methods

The importance of having the ability to use numerical methods to solve an explosion problem was realized in the mid 1900's when understanding the complexities of an actual explosion became an important issue in weapons design and analysis. These early efforts produced the first finite-difference methods for solving the NSE. All of these early methods had intrinsic difficulties generally with achieving sufficient accuracy, and with numerical stability specifically when they were used to compute the properties of shock waves and detonations [15, 16].

The intrinsic difficulties were based on the fact that the finite-differencing methods had an inherent numerical instability that introduced essentially uncontrolled numerical oscillations at the shock discontinuity. The first attempt to fix this by adding artificial damping terms (numerical diffusion) did not always work as expected and required *ad hoc* parameters to control the added numerical diffusion at the shock front [17, 18]. This method also caused more numerical problems when it was coupled to highly exothermic chemical reactions that might occur near shock fronts in detonation waves.

The major algorithmic breakthrough in our ability to solve the fluid-dynamic issues with computing explosions occurred in the early 1970's with the invention of flux-limiting methods [19]. These methods addressed the numerical origin of the uncontrolled numerical diffusion around propagating discontinuities by imposing solution constraints based on maintaining conservation, monotonicity, and causality. Over the next ten years, many communities adopted, expanded, and improved the new approach. Now all modern shock-capturing methods for solving the NSE with shocks either directly or indirectly use flux correction, especially near fluid-dynamic discontinuities. Application of these methods to astrophysical problems in addition to weapons research further aided their development [20].

With advances in computer capabilities (such as speed, memory, and architecture), the ability to perform meaningful numerical simulations advanced enormously. When the new methods for solving the NSE were combined with new methods for representing chemical reactions and energy release, applications opened up in almost every area of science, including atmospheric and solar physics, combustion, and astrophysics, and almost every branch of engineering. The accuracy of numerical solutions became mostly limited by speed and memory of available computers.

The next major step in computation was the recognition that when a fluid dynamics problem is solved with a monotone method (i.e., one that is designed so that it does not create any new, unphysical maxima or minima in the solution), there is often no need to resolve the viscous scale or add special models to describe the effects of turbulence. This concept is called MILES (monotone-integrated large-eddy simulation) or ILES (implicit large-eddy simulation) [21]. This is based on an interesting property of monotone methods: at the computational grid scale, monotone methods dissipate energy in a very physical way that mimics the natural viscous dissipation. To model a turbulent flow, it is sufficient to resolve some portion of the inertial range. The flow is then resolved from the largest scale down to the grid scale, at which the energy is dissipated by a numerically imposed viscosity. Thus the viscous dissipation scale is effectively replaced by a grid scale.

The use of MILES methods means that the extreme turbulence in an explosion can, in principle, be accurately computed without resorting to *ad hoc* models with empirical constants. This concept and its proof have taken many years of testing to validate, but now we believe we have a good understanding of how and why it works [22]. It is now widely accepted that if we resolve enough scales in a turbulent flow, we do

not have to resolve all length scales down to the viscous dissipation scale.

The final numerical advance that has changed our ability to compute explosions is the advent of adaptive gridding [23, 24]. Explosion problems are often characterized by a large disparity in physical scales and a concentration of important small-scale features, such as flames, shocks, and detonation waves, in relatively small areas of the computational domain. Since small-scale features require small computational cells, a uniformly spaced computational mesh throughout the entire computational domain usually means that there are large volumes of space with many small grid cells and nothing much happening. To increase the efficiency of computations, it makes sense to use fine grid around important flow features, and coarse grid everywhere else. Because of the dynamic nature of explosions, this adaptive gridding needs to be dynamically adjusted to resolve evolving flow features. This became possible with developments of special algorithms, generally called methods for adaptive mesh refinement (AMR).

As we show below, using explosion codes based on monotone methods with adaptive mesh refinement, coupled with the advances in computer power, has allowed enormous improvement in our ability to compute an explosion.

## 2.2. Previous Simulation of Coal-Mine Explosions

There are three main requirements for an RNSE code that is used to describe the full range of states that can occur in NG explosions.

1. The numerical model must solve the RNSE using a method appropriate for and accurate enough to capture the development and evolution of turbulence and shock phenomena.
2. There must be an “accurate enough” model for energy release, which, in our case, would represent natural-gas combustion.
3. The computational domain and what it contains must be specified and resolved numerically. This means that the code needs to be given boundary and initial conditions that make the problem unique and apply to a specific scenario.

Many adequate numerical methods exist for solving the RNSE, and many of these have been applied to NG explosions. If they are to predict DDT, however, they need to be monotone, have a chemical model that can reproduce properties of both laminar flames and detonations, and have enough resolution to compute the transition from laminar to turbulent flames to detonations, as it occurs. One of the main restrictions of many of the current commercial explosion codes is that they use “turbulence models.” The underpinning idea of a turbulence model is to solve the mean, large-scale fluid-dynamics equations on a computational grid in which the smallest grid size is substantially larger than the scale on which viscous dissipation occurs. Then the effects of sub-grid-scale turbulence and viscous dissipation are modeled by computing extra terms defined by the turbulence model (see, for example, [25]). The intended effect is that the turbulence model should modify the RNSE to account for unresolved small-scale effects, but in many cases this adds significant amounts of numerical diffusion that can mask DDT. Another issue related to the use of turbulence models, is that capturing DDT requires resolving the problem over a wide range of time and space scales. This could be as extreme as spatial scales ranging from micrometers or millimeters (e.g., viscous dissipation scales, flame thicknesses) to kilometers (channel lengths) and time scales ranging from nanoseconds to seconds (e.g., chemical reaction times).

An excellent discussion of many of the gas explosion models and codes, with an evaluation of their capabilities and limitations, is given in reviews by Lea and Ledin [26] and Popat et al. [27]. Commercial codes, such as FLACS [28, 29] and AutoReaGas [30], have been used for at least fifteen years by a number of communities. SAGE [31] is a code containing some higher-level algorithms and flexible gridding capabilities. All of these codes have been used to model coal mine explosions and help to explain observed damage [1, 4, 32]. They use different underlying numerical methods and implement somewhat different chemical submodels. Here we briefly describe relevant features of these codes so that they can be compared and contrasted to each other and to the the NRL codes and models we are currently using. This comparison will help to explain why we need a different code and different approaches to capture DDT.

Since both AutoReaGas and FLACS are based on monotone fluid-dynamics solvers, they should, in principle, be able to compute the properties of explosions and shocks. AutoReaGas uses a high-order monotone algorithm (based on a version of the flux-corrected transport (FCT) algorithm [16, 19] developed at NRL) and FLACS uses a lower-order algorithm. Practically, the higher-order algorithm in AutoReaGas means that this code requires fewer computational cells to resolve a feature in the flow, but it also means that it could take slightly longer to perform the calculation. The turbulence models used in both codes are the  $k - \epsilon$  models [25], which relate the dissipation rate of unresolved turbulence kinetic energy ( $k$ ) to the production of turbulence kinetic energy in the modified form of the RNSE. Based on the previous discussions, a question arises: Why does a monotone method need a turbulence model? The answer must be that the computations performed with the code are not resolved enough to take advantage of the natural dissipation properties of the algorithm they are using. This is not helped by the use of additional diffusion terms that come from the turbulence models.

In the AutoReaGas or FLACS calculations, the smallest grid size is of the order of 0.5 m and is much larger than a flame thickness, which is about 1 mm for a stoichiometric methane-air mixture [33]. Thus part of the turbulence model must represent features of chemical reactions and energy release that take place on the scale of the laminar flame thickness. The resulting description of the turbulent flame itself will be some averaged profile, but there are constants in the turbulence and chemical models that help ensure that the correct amount of energy is released overall, and this ensures the correct flame temperatures and deflagration velocities.

AutoReaGas and FLACS are RNSE codes because they contain combustion submodels that describe the concentration change rates of reactant and product species and the associated energy release rate. For large-scale explosion simulations, these submodels are empirical. For instance, AutoReaGas uses an empirical correlation between reaction rate and flame speed. FLACS uses the “ $\beta$  flame model” that correlates turbulent burning velocity with turbulence parameters. In both models, an increase in turbulent kinetic energy results in an increase in the reaction rate. These models, however, do not properly consider the physics of detonation or DDT.

AutoReaGas and FLACS are designed to approximately model deflagrations and can be applied to relatively low-pressure explosions. In most applications of these codes in the oil, gas, and chemical industries, the computed and measured explosion pressures do not exceed about 0.5 MPa. The large computational cell sizes they use mean that details of turbulence and its effect on flame acceleration and explosion pressure are not computed. The coarse grid also tends to “smear” or diffuse shocks and other rapidly rising pressure

waves that are important for DDT mechanisms. Thus, these models cannot predict extremely high pressures that could occur in a mining explosion as a result of possible DDT.

Despite these shortcomings at high pressures, such models still provide useful insights into many practical applications of interest at lower pressures. FLACS and AutoReaGas have been used to help analyze explosions in industrial facilities, such as oil production platforms, oil refineries, chemical process plants, and mines. In particular, these codes have been used to simulate explosions in off-shore oil and gas production facilities since the Piper-Alpha disaster in 1988 [34, 35]. Several groups in Europe have made attempts to use these models to study gas explosions in mines. NIOSH has used them with success to help analyze mine explosions in LLEM, which probably represents the most extensive use of these models in a mining industry application. The full extent of this initial gas explosion modeling application in mining is well documented in several reports [36, 37].

SAGE code [31] is used by DOD to study blast effects from weapons. It uses a relatively high-order monotone method for capturing shocks, and to this it adds a method for adaptive mesh refinement (AMR) so that it can capture developing features in the flow. It also contains models that allow it to evaluate the effects of explosions on solid-fluid interfaces, such as between concrete and air. It can simulate strong shock waves and complex combustion fronts because AMR can introduce resolution where it is needed. It does not use a turbulence model, but again, because it is based on a monotone algorithm with good grid resolution, it can take advantage of MILES. The chemistry model is based on an Arrhenius reaction model that describes the combustion rate in a computational cell in terms of the concentrations of reactants and products and chemical rate constants. The Grüneisen equation-of-state relates pressure to the density and the internal energy of the combustion products for methane-air burning. Because of its versatility, SAGE can model combustion through either a deflagration or detonation mechanism. It is not known if it can compute DDT from first principles, or whether the chemical model is adequate to do this. It is also not known if the type of adaptive gridding it uses would be adequate for computing DDT. Currently, the transition from a deflagration to a detonation is done in an *ad hoc* manner.

It is probably accurate to say that complete reactive CFD simulation of any realistic large-scale explosion is beyond any of today’s computer capabilities, and probably beyond our ability to specify the initial conditions and input constants. *The only viable approach is to select levels of algorithms, models, and gridding so that those chemical and physical processes that we think are important are resolved and the combustion phenomena they create are captured.*

### **2.3. Previous NRL Explosion Simulations: Deflagrations, Detonations, and DDT**

The computational tasks performed for NIOSH rest heavily on prior work at NRL in algorithm development, code construction, and use of these codes on high-performance computers to study fundamental mechanisms of explosions. The earliest NRL work includes some of the first computational studies of propagating flames and detonations, and culminates in the publication of the book *Numerical Simulation of Reactive Flow* [15]. Since ~1995, there has been a dedicated effort to understand DDT. The parts of that work which are relevant to this report comprise the rest of this Section.

One general conclusion, however, is that it *is* possible to compute the DDT process by solving the RNSE, given enough numerical resolution of critical regions in the system and a chemical model that spans the

combustion regimes from autoignition to laminar-flame propagation. We come back to this major conclusion at the end of this section.

### 2.3.1. *Early Development of Codes: Simulations of Flames and Detonations*

The earliest work at NRL in numerical simulations of reactive flows, and the particular application to explosions, began at the end of the 1960's with simulations of high-altitude nuclear bursts. This required constructing numerical, physical, and nonequilibrium chemical models for effects of blasts in air. The ionization, radiation, and products of the chemical reactions produced the signatures of the explosion. For our current concerns and discussions of DDT, the significant advances that came from this early work are the development of flux-limiting algorithms and their application for the NSE, fast solution methods for ordinary differential equations to represent the chemical reactions, and the new numerical algorithms that allowed simulation of high-speed reactive flows.

In the mid-1970's, NRL work turned to combustion, which emphasized chemically reactive flows where hydrogen or hydrocarbons were the fuels consumed. Much of this work is summarized in [15], which describes methods and applications. Subsequently, many of these approaches were developed further at NRL and elsewhere to the point where they had been incorporated into commercial CFD codes and used in industrial situations. The second edition of this book, which was published in 2001 [16], also gave information on how to use these commercial and other acquired codes. NRL work in explosions, deflagrations, and detonations focused on computing the single- and multi-dimensional structure of propagating flames and detonations, with some consideration of initiation and quenching. In addition, there was related work on chemical-fluid instabilities, such as those which led to chemical-acoustic coupling [38].

The following summary of work on DDT, starting around 1995 and continuing through to the present, is cast in terms of major conclusions with supporting results shown in figures with detailed captions. Only those aspects of the conclusions and observations that are related directly to DDT in methane-air and natural gas-air mixtures will be discussed here.

### 2.3.2. *Fundamentals of Deflagration-to-Detonation Transition*

The overriding objective of the simulations was to determine if we could compute DDT from "first principles." More specifically, we wanted to determine if we could resolve a large enough range of the temporal and spatial scales to see the transition. At the minimum, this would require resolving spatial scales from the laminar flame thickness to the size of the system, when and where they are important in the process. The approach we used combined numerical simulations with comparisons to laboratory experiments in an attempt to find mechanisms for unexplained observations. The primary tool was multidimensional, time-dependent numerical simulation of unsteady combustion using high-performance parallel computers. A more extensive description is given in [5], and presented in more detail in the references therein.

**Conclusion:** *We can compute DDT in systems with shocks and flames present.*

Figure 2.1 describes one of the first problems studied, shock-flame interactions and the evolution to a turbulent flame and DDT in an enclosed channel filled with an acetylene-air mixture. The configuration was based on experiments performed at the University of Wales at Aberystwyth. This result proved that it was

possible to simulate DDT by solving the RNSE. The result was confirmed by convergence studies for this flow and by comparisons to experiments [39]. The mechanism for DDT was the occurrence of a hot spot (or ignition center) that arose in shocked, compressed, and heated gas in the vicinity of a turbulent flame. Subsequent computations, with stronger intensity shocks and turbulence, produced hot spots closer to the flame brush. In one of the most intense cases, DDT occurred in funnels of unburned material inside the flame brush.

**Conclusion:** *Detonations arise when local conditions in unreacted material allow a spontaneous wave to form, and this wave evolves into a shock that is strong enough to become a detonation which can propagate outside the gradient.*

The gradient mechanism of detonation ignition, proposed by Zeldovich [40] and discussed and generalized by many researchers since, teaches us that a gradient in chemical reactivity can generate a supersonic “spontaneous wave” that may undergo transition to a detonation. If it does not, it results in a decoupled flame and a shock. Previous theoretical and some experimental studies of this ignition mechanism had been done in isolation from a turbulent flame: a gradient was proposed or created and the subsequent behavior studied.

Our simulations [41–43] have shown that such gradients arise naturally around hot spots in unreacted material as part of the background flow in which the turbulent flame exists. Close examination of the hot spot ignition have shown that it occurred in a gradient of reactivity which allowed the development of a spontaneous wave.

**Conclusion:** *Interactions of shocks and flames are important in creating the conditions in which hot spots can arise and subsequently produce detonations.*

Flames generate shocks, especially in confined spaces or in the presence of obstacles. In turn, shock interactions with flames create and drive the turbulence in flames far more dynamically than other combustion instabilities. Enhanced turbulence means a higher energy-release rate, and more fluctuations in background material that promote hot-spot formation and increase the likelihood of DDT. This is shown in Figure 2.1, and discussed in more detail in [41–43].

**Conclusion:** *Reflected shocks and boundary layers can interact with shocks and flames to reduce the time to DDT.*

High-intensity turbulent deflagrations in channels often generate shocks and high speed flows that interact with channel walls and flames. These interactions enhance turbulence, and can also produce complex dynamic structures that allow the flame to spread supersonically relative to the unburned material. This detonationless supersonic flame spread significantly increases the energy release in the system, and eventually accelerates DDT.

For example, a shock reflected into an incoming flow can interact with a boundary layer and produce a complex  $\lambda$ -shock structure containing a leading oblique shock followed by a recirculation region. If the flame is close enough to this structure, it becomes entrained in the recirculation region and attached to the oblique shock. The resulting reactive structure appears as a shock-flame complex propagating at approximately one half of the CJ velocity. This leads to an increase in the energy-release rate, the formation of Mach stems in the middle of the channel, and creation of multiple hot spots behind the Mach stem, thus facilitating DDT

[44]. An example of this phenomenon is shown in Figure 2.2 that compares simulations with and without the effects of boundary layers for a shock-flame interaction in an ethylene-air mixture. Similar phenomena can be produced by interactions of reflected shocks, flames, and wakes behind obstacles [45].

**Conclusion:** *For the large-scale features and transitions in the flow, 2D simulations give both qualitative and surprisingly good quantitative agreement with 3D simulations and experiments.*

Figure 2.3 shows the results of a calculation with boundary layers for a three-dimensional configuration analogous to the two-dimensional version shown in Figure 2.2. For this ethylene-air mixture, 2D and 3D simulations give similar times to DDT [46]. A large part of this agreement, which seemed fortuitous, was attributed to the unusual nature of the nonequilibrium, shock-generated turbulence in the flow [44–46].

### 2.3.3. Flame Acceleration and DDT in Channels with Obstacles

This work focused on flame propagation, acceleration, and eventual DDT in obstructed channels filled with a stoichiometric mixture of hydrogen and air. The geometrical parameters of the channel and the method of flame ignition were varied to extract general principles that could be used to evaluate the likelihood of DDT. Issues related to numerical accuracy were addressed. Validating experiments performed at Warsaw Institute of Technology and AberShock, Inc. (UK) tested selected aspects of the results [47, 48]. Although the hydrogen-air mixture used in this work is much more sensitive than NG-air, the general principles learned can be used to guide experiments and simulations in NG. For that reason, we now present a summary of the hydrogen simulations.

**Conclusion:** *A spark ignition in an obstructed channel can lead to DDT. Detonations can form when shocks collide with obstacles.*

At the initial stages of flame propagation, a thermal expansion of hot combustion products generates a flow ahead of the flame. This flow, that becomes non-uniform due to interactions with obstacles, distorts the flame, thus increasing its surface area. This increases the energy generation rate and results in flame and flow acceleration. Flame-vortex interactions and a number of fluid instabilities, such as Rayleigh-Taylor (RT) and Kelvin-Helmholtz (KH), continue to increase the flame surface area, and further accelerate the flow. The accelerating flow generates shocks that reflect from obstacles and interact with flame surface causing Richtmyer-Meshkov (RM) instabilities that become a dominant mechanism for the flame wrinkling. The flame continues to accelerate, shocks strengthen, and eventually shock reflections from obstacles create hot spots that produce detonations through the gradient mechanism. A representative example of this process is shown in Figure 2.4 [7].

A series of simulations performed for different energies of ignition sparks shows that though the ignition energy affects the initial flame development and changes the time to DDT, this often has little or no effect on the distance to DDT [7].

**Conclusion:** *As the height of the channel increases, the final combustion regime changes from choking deflagration to quasi-detonation, and then to detonation [7].*

For narrow channels, the choking deflagration is the final regime resulting from flame acceleration. In this regime, the turbulent flame and leading shock form a complex in which they remain a relatively constant

distance apart. Together, they travel at about  $(0.4\text{--}0.5 D_{CJ})$ . The leading shock diffracts as it passes over each obstacle, and then it reflects from the bottom wall after each diffraction.

For larger channels, the choking deflagration with the shock-flame complex undergoes a transition to a quasi-detonation. In this regime, there are repeated DDT events that produce detonations as shocks collide with obstacles. These detonations do not survive diffraction over an obstacle, but they are constantly reignited as the leading shock collides with the next obstacle.

For even larger channels, the DDT leads to a detonation that does survive diffraction and propagates through the system.

**Conclusion:** *More obstacles per unit length create more perturbations, which increase the flame surface area more quickly. Thus, the flame speed grows faster.*

**Conclusion:** *Detonations form when shocks collide with obstacles. These collisions are most effective in generating hot spots and detonations when they involve Mach stems.*

A Mach stem may form when the diffracted leading shock collides with the channel wall. If this Mach stem is strong enough, its collision with the next obstacle may produce a detonation. The strength of this Mach stem depends on the strength of the leading shock, the height of the obstacle that causes the shock diffraction, and the distance to the next obstacle. Decreasing the distance between obstacles eventually eliminates the Mach stem, and then the detonation initiation requires a stronger leading shock [6].

Thus, the effects of obstacle spacing on flame acceleration and the actual detonation initiation are counteracting to some extent. This is why increasing the number of obstacles per unit length may increase the distance to DDT, even though the flame speed would grow faster.

Different shock configurations that form just before the detonation initiation are illustrated by Figure 2.5. The figure shows the leading shock and turbulent flame brush developed in a series of hydrogen-air simulations in which the spacing between successive obstacles,  $S$ , inside the channel is systematically varied. We observe two distinct configurations:

*Configuration 1:* For  $S$  equal to or larger than the channel width  $d$  ( $S/d = 1, 1.5, 2$  in Figure 2.5), a Mach stem is formed by the diffracting shock reflecting from the bottom wall. The detonation is ignited when this Mach stem collides with an obstacle.

*Configuration 2:* For  $S$  smaller than the channel width ( $S/d = 0.25, 0.375, 0.5, 0.75$  in Figure 2.5), Mach stems do not form.

The detonation initiation for this configuration is more difficult since the leading shock without a Mach stem may not be strong enough. For  $S/d = 0.375, 0.5$  and  $0.75$  detonations do not develop. Isolated detonations sometimes appear in pockets of unburned material between obstacles behind the leading edge of the flame, but they cannot spread. For  $S/d = 0.25$ , however, multiple isolated detonations contribute to the final stages of flame and shock acceleration, and the leading shock becomes strong enough to ignite a detonation by a direct collision with the top part of an obstacle. The distance to DDT in this case is about 3 times longer than for the case in which  $S/d = 1$ .

### 2.3.4. DDT in Large Spaces Containing Obstacles

Here we consider a large area with many obstacles, either square or rectangular, with different kinds of symmetrical or asymmetrical placement. This is work in progress, so that any conclusions are preliminary and subject to revision or qualification as the analysis proceeds. There are, however, a few observations that are important to note now as they are relevant to explosions in coal mines.

**Conclusion:** *The evolution from a spark or a flame to a detonation in a two-dimensional array of obstacles follows an overall pattern similar to what was seen in channels with obstacles.*

This is shown by the example in Figure 2.6. After ignition, a small flame propagates for some time in a laminar regime, and then accelerates as its surface bends with the flow around obstacles. Turbulence develops as shear layers appear in the flow and become unstable, and this contributes to the burning rate increase. As the flow and flame accelerate, shocks are formed ahead of the flame. The shocks are reflected by obstacles and propagate back to the flame, thus causing shock-flame interactions and further increasing the energy-release rate. When shocks become strong enough, their collisions with obstacles create hot spots that produce detonations [8, 49].

**Conclusion:** *In structured arrays of obstacles, there are directional preferences for flame spread and the occurrence of DDT, and these directions are different for different stages of flame acceleration*

In structured arrays, some directions are more obstructed than others, and the flow loses more momentum in more obstructed directions. This delays the flame spread in more obstructed directions at initial stages of flame acceleration. On the other hand, the number of shock-flame interactions is higher in more obstructed directions, and this leads to a higher flame acceleration and faster strengthening of the leading shocks in these directions at later stages. As a result, detonations first appear in more obstructed directions.

Detonations spread in all directions and interact with obstacles causing shock reflections and diffractions. Some parts of detonation fronts are quenched by diffractions, but they are reignited by collision of decoupled shocks or overtaken by other detonations. Thus detonations continue to spread and quickly burn all the material between obstacles [8].

### 2.3.5. Computing DDT: General Observation

**Conclusion:** *Two-Dimensional and three-Dimensional simulations have often given the same values of run-up distances to DDT consistent with experimental results. It is often sufficient to perform two-dimensional simulations.*

This conclusion is based on repeated comparisons between simulations and experiments, and between 2D and 3D simulations [5, 49]. It appeared early in our studies, and has been repeatedly borne out by new comparisons. The physical meaning of this conclusion is a complicated concept. Our current belief is that the origin of this agreement lies in the the particular fundamental properties of the nonequilibrium, non-Kolmogorov turbulence in these flows that are somewhat similar in 2D and 3D. This is a topic which is important to understand and is currently under study in another research program. Meanwhile, we are constantly checking the assumptions involved and use this property to our advantage in the simulations described below for methane-air mixtures,

**Conclusion:** *It is possible to compute the DDT process by solving the RNSE, given enough numerical resolution of critical regions in the system and a chemical model that spans the combustion regimes from autoignition to laminar-flame propagation.*

Now that we have shown this, the questions are: What are the limitations? How can we beat them? How do we apply the information we have and could obtain?

**Experimental  
and  
Computational  
Geometry**

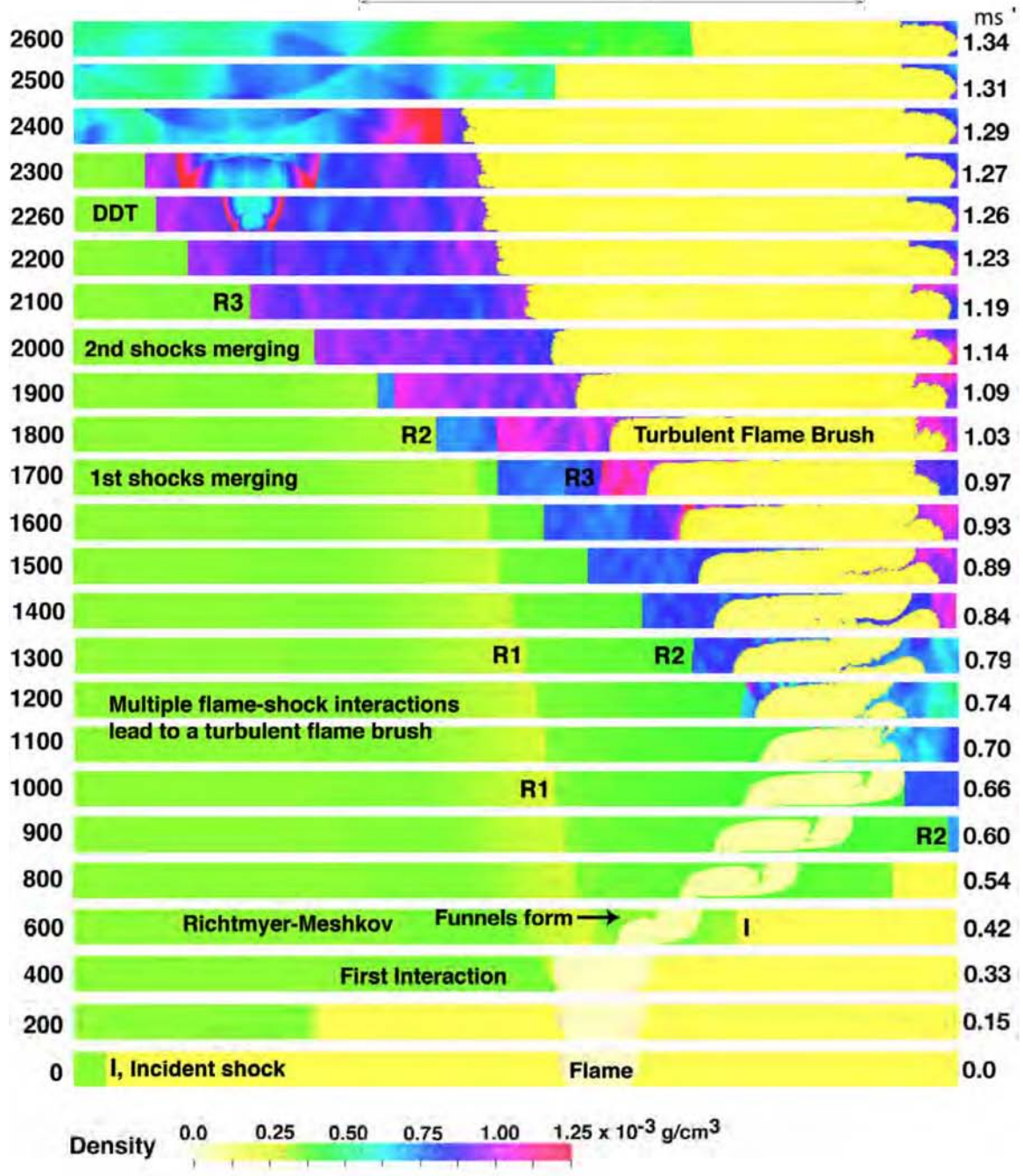
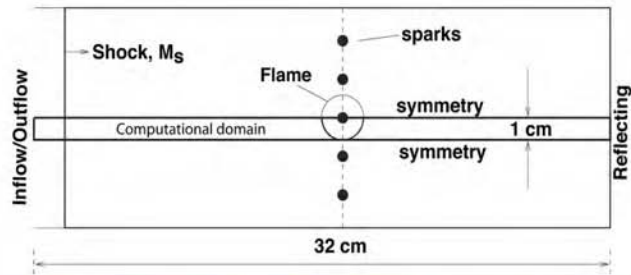


Figure 2.1. *Caption on next page.*

**Figure 2.1.** This figure is taken from one of the first computations showing DDT arising from a gradient of reactivity in the flow [41]. The schematic on the top shows the conditions simulated, which were modeled on experiments performed at the University of Wales Aberystwyth. Time sequence of density fields showing the overall evolution of a Mach 1.5 incident shock interacting with a low-pressure acetylene-air flame, corresponding to the initial and boundary conditions shown on the top. The computational domain for each frame is 32 cm by 1 cm. (The vertical scale is stretched by a factor of 1.28.) Time steps are shown on the left side and physical times are shown on the right side. Note that time differences between frames are not equally spaced, but are clustered near the DDT event starting at step 2200. Incident shock, I; Reflected shocks R1, R2, R3.

The initial frame, step 0, shows the shock on the far left and the unperturbed flame approximately in the middle of the domain. As time passes, this incident shock I approaches the flame, and the shock-flame interaction begins around step 400. When I interacts with the left side of the flame, the result is a rarefaction wave that moves back upstream, and a transmitted shock that moves through the flame. When this transmitted incident shock interacts with the right side of the flame, it produces a weak reflected shock R1 that also moves upstream, first through the material burned by the flame, and then through the initially shocked, unburned material. The rarefaction wave and R1 can be seen in frames 600 through 1700. The incident shock transmitted through the flame moves downstream toward the end wall, as seen in frames 600 and 800, and reflects from the wall by step 900. This produces a strong reflected shock R2.

The interactions of I and R1 with the flame trigger a Richtmyer-Meshkov (RM) instability, which creates a large funnel of unburned material that penetrates the burned region. At frame 1000, R2 begins to interact with the distorted flame. This generates a new sequence of reflected and transmitted shocks and rarefactions which further distort the flame. The shock R2 passes through the flame by step 1200, and continues to move upstream. It finally merges with R1 between steps 1700 and 1800. When R2 passes through the left side of the flame at step 1200, it generates another reflected shock that moves to the right. This shock passes through the flame, reaches the end of the tube, and reflects from the end wall between steps 1300 and 1400, producing the R3. The shock R3 passes through the flame again, further distorting the flame, and finally emerging from the left side of the flame at step 1600. This third emerging shock R3 propagates in material that was shocked three times previously (incident shock plus two reflected shocks). It eventually merges with the combined reflected shock (R1-R2) between steps 1900 and 2000.

Between steps 2200 and 2260, two sudden explosions occur almost simultaneously in the material behind the merged reflected shock, R1-R2-R3. These explosions coalesce to form a detonation that spreads in all directions. As it moves to the right, it enters the flame between steps 2400 and 2500, and decays into a shock.

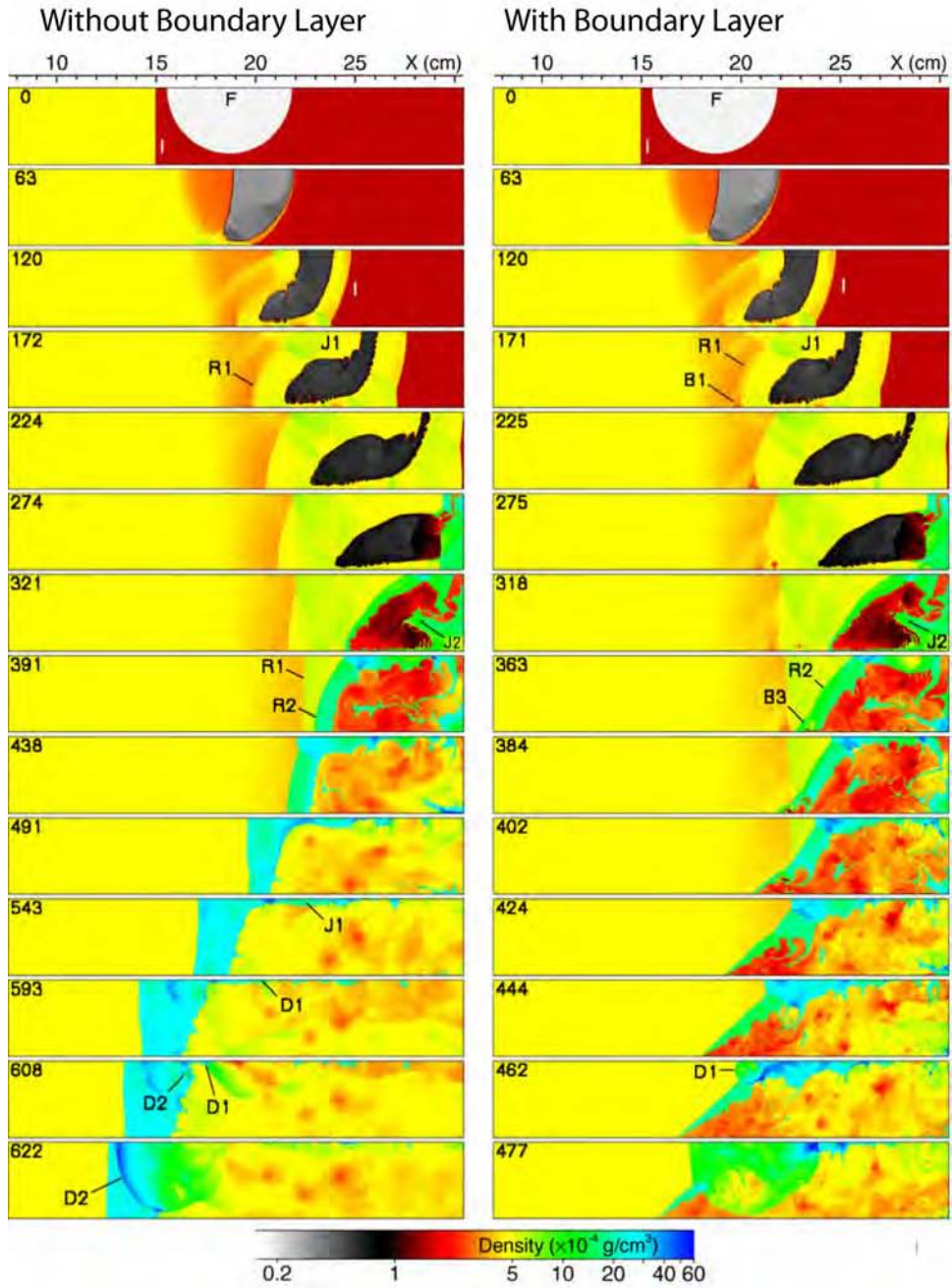
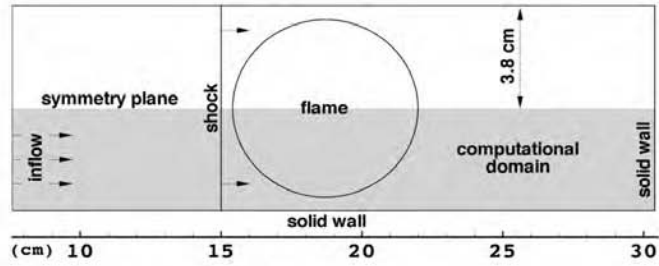


Figure 2.2. Caption on next page.

**Figure 2.2.** This figure is taken from one of the first computations of the effects of boundary layers on shock-flame interactions and DDT [44] showing DDT arising from a gradient of reactivity in the flow [41]. The schematic on the top shows the conditions simulated, which were modeled on experiments performed at the University of Wales Aberystwyth. The sequence of density fields showing shock-flame interactions and DDT in a stoichiometric ethylene-air mixture at  $P_0 = 1.44 \times 10^3$  Pa for initial and boundary conditions shown on top. Two cases, with and without boundary layer were computed. Incident shock Mach number  $M_s = 1.9$ . Time ( $\mu\text{s}$ ) is given on the left side of each frame. The letters indicate the incident shock I, the flame F, reflected shocks R1 and R2, funnels of unreacted material J1 and J2, detonations D1 and D2, and bifurcated structures B1, B2 (not shown) and B3.

The sequence on the left is taken from a simulation with free-slip boundaries that suppressed the formation of a boundary layer. The first frame at  $0 \mu\text{s}$  shows the initial conditions, a planar incident shock I moving from the left to the right, and the flame F. The sequence of frames, with time increasing from top to bottom, shows the incident shock I moving through and distorting the flame, reflecting from the back wall, and then the reflected shock R2 passing through and further distorting the flame. Hot spots form in unreacted material, and eventually two of the hot spots undergo transitions to detonations at  $593 \mu\text{s}$  and  $608 \mu\text{s}$ . The evolving structure of this flow has many similarities to the acetylene-air simulations shown in Figure 2.1.

The sequence on the right shows the development of the flow for the same mixture and value of  $M_s$ , but now for the case with a no-slip wall that allows a boundary layer to form. The boundary layer behind the incident shock is about 0.1 cm thick and is not visible in these frames. From the beginning of the simulation to about  $225 \mu\text{s}$ , the flow development is practically the same as it was for the case with free-slip walls. Boundary-layer effects do become apparent at  $171 \mu\text{s}$  when R1 begins to form a weak bifurcated structure B1, but B1 does not affect the flame until a later time. Another bifurcated structure B2 (not shown) begins to grow immediately after the incident shock reflects from the back wall, but it is quickly destroyed by a strong oblique shock coming out of the flame. Multiple reflections of oblique shocks and rarefaction waves inside the thin layer of unreacted material between the flame surface and the bottom wall prevent the formation of new bifurcated structures until about  $340 \mu\text{s}$ .

The flame remains essentially unaffected by boundary-layer phenomena until  $363 \mu\text{s}$ . By that time, R2 has passed through the flame, and a new strong bifurcated structure B3 begins to develop. When a bifurcated foot forms and grows, a recirculation region forms and grows behind it. Near the bottom wall, the flow in the recirculation region is moving towards the shock. The flame, which almost touches the bottom wall and moves with the flow behind the shock, penetrates the recirculation region. The flame approaches the shock first as a thin jet along the wall, and then quickly spreads inside the recirculation zone. The energy released by the flame in the recirculation region accelerates the growth of the bifurcated foot until the top of the foot reaches the symmetry plane (top boundary of the computational domain) and a forms a Mach reflection at the top boundary by  $424 \mu\text{s}$ .

The surface area of the flame interacting with the bifurcated shock increases, thus increasing the energy-release rate in the system. The energy release gradually increases the strength of the bifurcated shock and the Mach stem. Eventually, the temperature behind the Mach stem becomes high enough to ignite the mixture. Ignition produces several hot spots, spontaneous waves, and residual flames that grow quickly, interact with vortices, and eventually trigger a detonation D1.

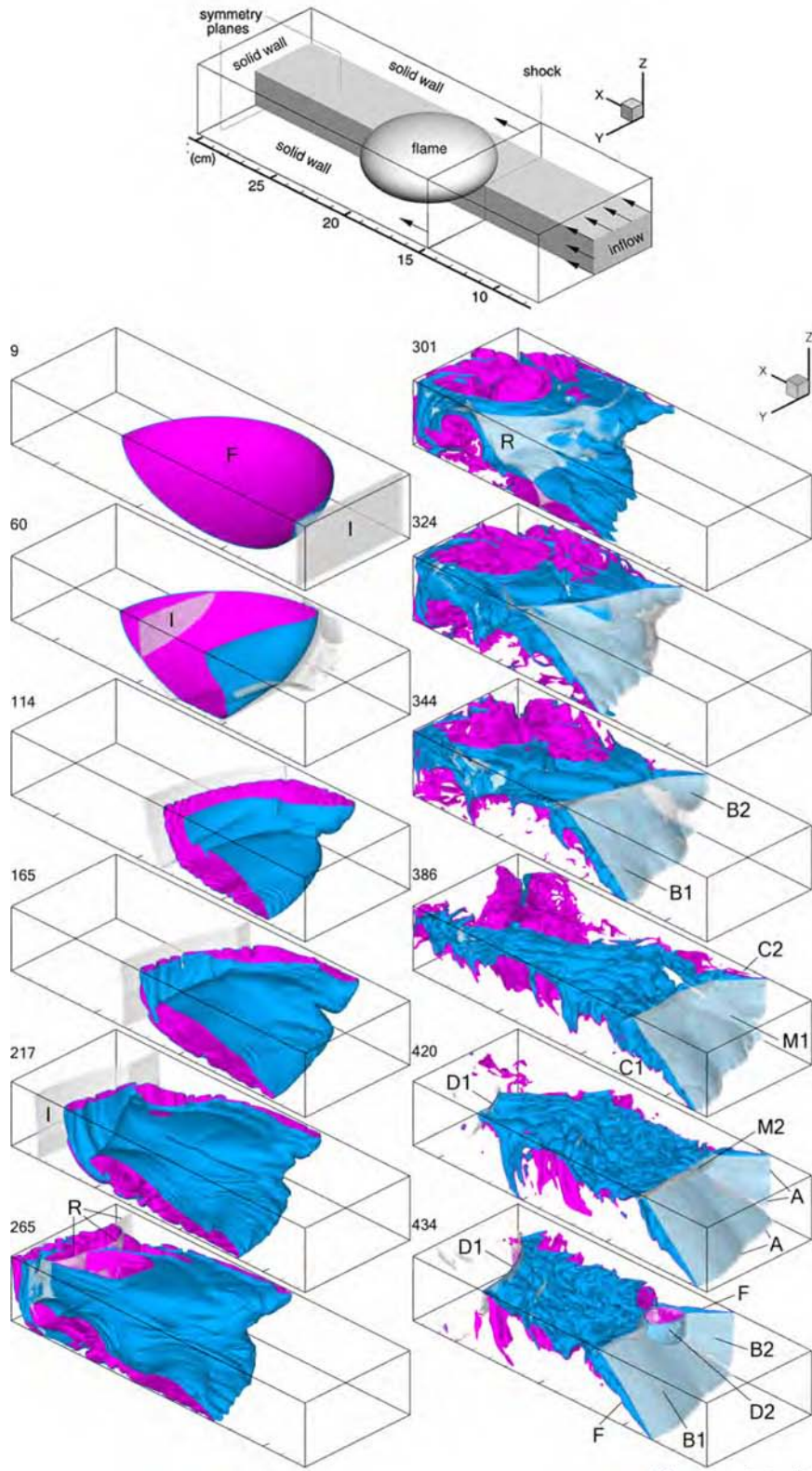


Figure 2.3. Caption on next page

**Figure 2.3.** Three-dimensional simulations [46] of the same problem shown in 2D in Figure 2.1. The figure shows shock-flame interactions and DDT in a stoichiometric ethylene-air mixture at  $P_0 = 1.44 \times 10^3$  Pa calculated for the initial and boundary conditions schematically shown on the top. Gray box on the top corresponds to the computational domain. No-slip walls are  $y = 0$  and  $z = 0$ , opposite walls are symmetry planes. Frames show a time sequence of computed 3D surfaces of flame (blue side faces unburned mixture, purple side faces burned gas) and shock (gray semi-transparent) in a 10.6 cm long part of the computational domain adjacent to the end wall ( $x = 30.4$  cm) for 217-386  $\mu\text{s}$ , and shifted 1.5-3 cm from the end wall for other times. Time in microseconds is given in each frame. The letters indicate the incident shock (**I**), the flame surface (**F**), the reflected shock (**R**), the bifurcated shocks (**B1**, **B2**), the recirculation areas (**C1**, **C2**), the shock-flame attachment line (**A**), the Mach stems (**M1**, **M2**), and the detonations (**D1**, **D2**).

The incident, planar shock moves along the  $x$ -axis and interacts with the flame. As in the two-dimensional calculations described above (Figure 2.2), the interaction is dominated by the Richtmyer-Meshkov instability, triggered by the flame curvature. The instability generates a large three-dimensional vortex that distorts the flame and creates a funnel of unreacted material in central parts of the shock tube near symmetry planes. On smaller scales, the RM instability creates small ripples on the flame surface. The interaction also distorts the initially planar shock that propagates through burned and unburned materials at different speeds. Oblique parts of the distorted shock reflect from side walls and interact again with the flame, creating more distortions.

As the flame continues to move with the flow, the incident shock reaches the end wall at 255  $\mu\text{s}$  and reflects. The stronger reflected shock **R** moves back through the already perturbed flame and creates more distortions at different scales. The flame quickly develops a very convoluted surface and becomes turbulent. The energy release accelerates due to the increased surface area of the flame and the increased temperature and density of unburned material behind the reflected shock.

When the reflected shock crosses the flame and enters the unburned material upstream, it begins to interact with boundary layers that developed near the no-slip walls. These interactions result in shock bifurcations **B1** and **B2** that appear as oblique shocks propagating along the walls,  $y = 0$  and  $z = 0$ . Shock bifurcations also create strong recirculation regions **C1** and **C2** near the walls. The recirculation flow entrains the flame that spreads through the recirculation region, approaches the bifurcated shock, and then attaches to it near the wall. The attachments first occurs near symmetry planes, where the initial flame surface was closest to no-slip walls. Then the attachment line approaches the corner  $y = z = 0$  between these walls. The attachment line is rather irregular because the flame and the boundary layer behind the bifurcated shock are turbulent. Above the attachment line, the flame surface **F** coincides with a slip surface that forms behind the bifurcated shock. The Kelvin-Helmholtz instability that develops along this surface generates more turbulence.

The reactive bifurcated shocks propagate with a speed of about a half  $D_{CJ}$  and interact with each other along the line that begins in the corner  $y = z = 0$ . The interaction between oblique shocks **B1** and **B2** produces an oblique Mach stem **M1** that generates additional vorticity and locally increases the temperature of shock-compressed material. The oblique shocks are relatively weak, and therefore the oblique Mach stem is not strong enough to ignite the material.

DDT producing detonation **D2** occurs when the bifurcated shock **B1** attached to the wall  $z = 0$  forms another Mach stem **M2** near the symmetry plane  $z = 1.9$ , and this central Mach stem interacts with the oblique Mach stem **M1** creating a hot spot. Another detonation **D1** appeared earlier in the funnel, near the end wall, but it did not affect the formation of **D2** behind two interacting Mach stems.

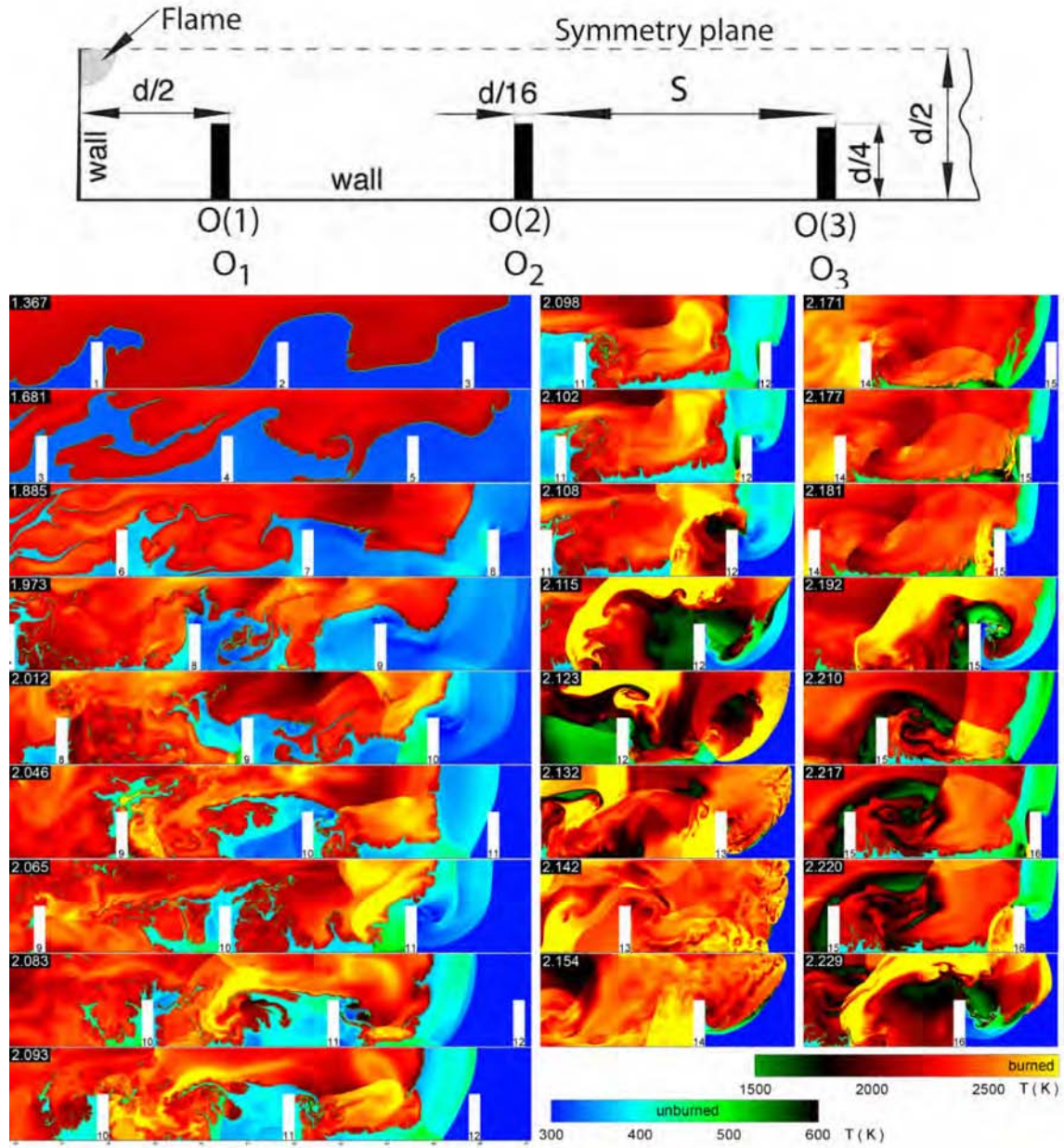


**Figure 2.4.** Accelerating flame (left column), DDT, and quasi-detonation (two right columns) in a half-channel with obstacles computed for the conditions shown by the schematic on top [7].  $d/2 = 2$  cm, the total channel length  $L = 64$  cm, and  $dx_{min} = 1/512$  cm. Times in milliseconds are shown in frame corners. The channel is filled with a stoichiometric hydrogen-air mixture at  $P_0 = 1$  atm.

A laminar flame, ignited at the left top corner of the computational domain, propagates with the velocity close to  $S_l = 298$  cm/s relative to unburned material. Hot reaction products expand and push unreacted material towards the open end of the channel. The flame front propagates with the moving flow and quickly becomes very convoluted as the flow interacts with obstacles. The increasing flame surface area results in faster energy release, thus accelerating the flow and increasing the flame speed in the laboratory frame of reference.

*Caption continued on next page.*

**Figure 2.4.** *Caption continued*

As the flame passes obstacles, it wrinkles due to the Rayleigh-Taylor (RT) instability caused by the flow acceleration. The unreacted flow ahead of the flame becomes sonic by 1.4 ms, just past  $O_5$ . Noticeable shocks begin to form ahead of the flame past  $O_7$  at 1.85 ms. They reflect from obstacles and side walls, and interact with the flame triggering Richtmyer-Meshkov (RM) instabilities. Kelvin-Helmholtz (KH) instabilities develop at the flame surface when a jet of hot burned material passes through a narrow part of the channel and a shear layer forms downstream of the obstacle. RT, RM, and KH instabilities, and flame-vortex interactions in obstacle wakes are the mechanisms responsible for increases in flame surface area, energy-release rate, and, eventually, shock strength. The elevated temperature behind shocks also contributes to the increased energy-release rate because  $S_l$  increases and shocks passing through the reaction zone release additional energy.

The average flame velocity gradually increases and reaches 800 m/s by 2.1 ms. This velocity equals about 0.8 of sound speed in the burned material, or  $0.4D_{CJ}$ , and is typical of what has been called the choking regime of flame propagation observed in experiments with obstructed channels. As the shock and the flame accelerate, the leading edge of the flame remains about 1 cm behind the leading shock, which diffracts at every obstacle and reflects from the bottom wall after each diffraction. The reflection type changes from regular to strong as the reflection point approaches the next obstacle. The resulting Mach stem becomes stronger after each diffraction, and the temperature of the hot region that forms when the Mach stem collides with an obstacle increases. At 2.100 ms, the reflection of the Mach stem from  $O_{12}$  creates a region with temperatures above 830 K. Two hot spots in this region ignite producing two small flame kernels. Then a detonation appears near one of the kernels and propagates through the unreacted material.

The newly formed detonation propagates through the gap between the flame and the obstacle into the shock-compressed material ahead of the flame. As the detonation passes around the obstacle, the lower part of the front decouples into a separated shock and a flame. The upper part of the front remains essentially undisturbed and develops detonation cells before it collides with the upper boundary. The collision creates a strong reflected shock that triggers a detonation in both the shock-compressed layer between the leading shock and the decoupled flame, and the uncompressed material. The strong detonation wave in the uncompressed material quickly develops detonation cells, collides with  $O_{13}$  at 2.125 ms, and diffracts. As the diffraction weakens the detonation wave, detonation cells grow and form an irregular two-level structure. The diffraction on  $O_{14}$  completely decouples the shock and flame by 2.164 ms, and effectively kills the detonation. A new detonation is ignited in the shock-compressed material by the collision of the Mach stem with  $O_{15}$  at 2.179 ms, but this detonation is unable to propagate through the very narrow gap between the obstacle and the flame. The leading shock and the flame remain decoupled until the Mach stem hits  $O_{16}$  and triggers a new detonation at 2.217 ms that spreads past the obstacle. This quasi-detonation regime that involves the detonation diffraction, failure, and reignition continues until the end of the channel.

---

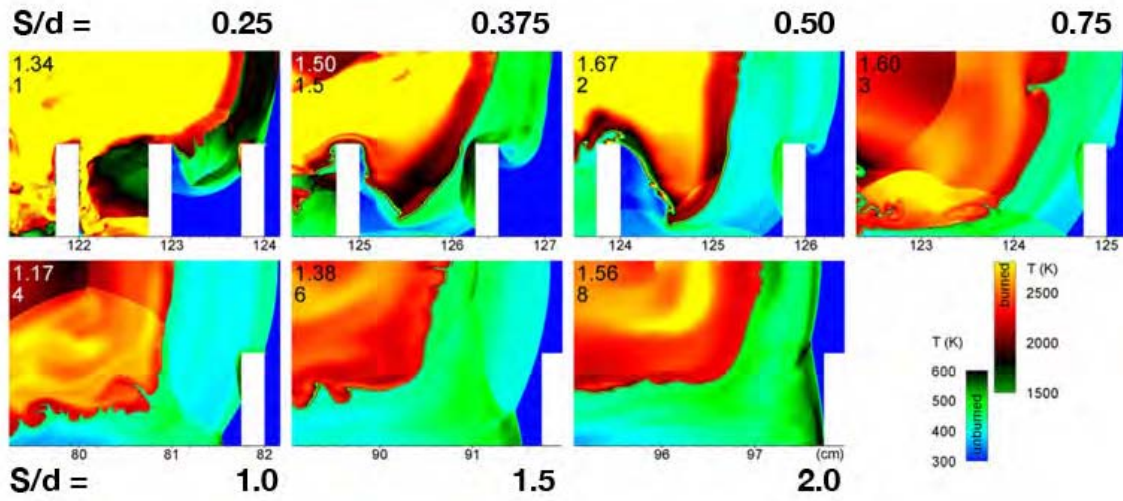


**Figure 2.5.** Flame and shock configurations in hydrogen-air mixture just before the detonation initiation or at the end of the channel. A Mach stem forms near the bottom wall for larger channels ( $S = 4, 6, 8$  cm), but not for smaller channels ( $S = 1, 1.5, 2, 3$  cm). Half-channel height  $d/2=2$  cm.  $S$  is defined by the schematic in Figure 2.4.

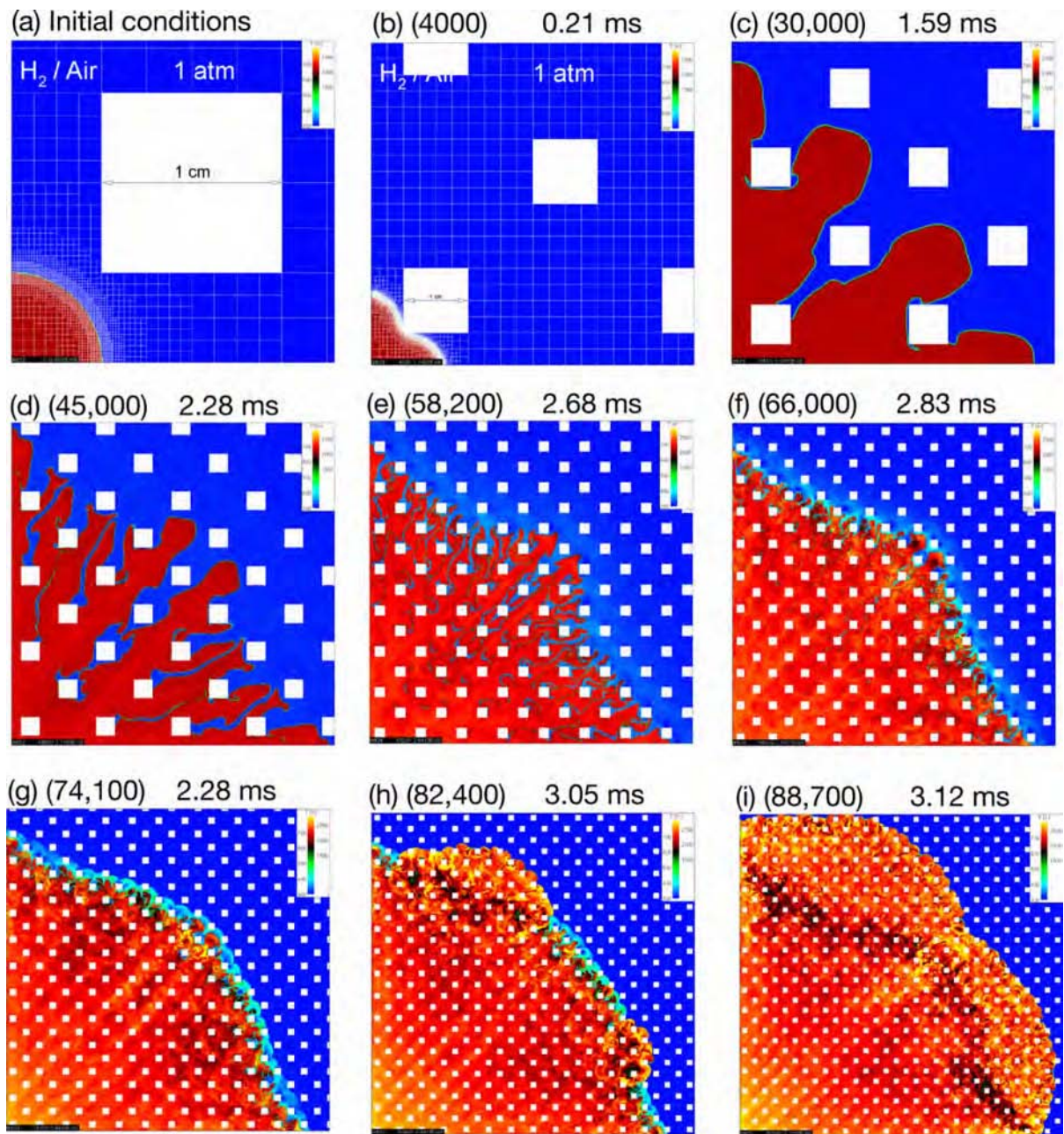


**Figure 2.6** Premixed hydrogen-air flame propagating through 2D array of obstacles after a weak spark ignition in the left bottom corner. The size of each obstacle is  $1 \times 1 \text{ cm}^2$ , the distance between neighboring rows of obstacles is 1 cm, and the computational cell size  $1/128 \text{ cm}$ . The timestep number and time from ignition are shown above each frame. Colors show temperature. Detonations appear in frame (h) and spread in all directions. The dark (low-temperature) band in frame (i) separates materials burned in deflagration and detonation regimes. An enlargement of a portion of frame (g) was shown earlier in Figure 1.2.

### 3. Flame Acceleration, DDT, and Detonations in Methane-Air Mixtures

The purpose of the theoretical and numerical effort is to develop a tool that will help us to address the pivotal question:

*Given a flammable mixture of methane and air of sufficient volume and lateral extent, can the mixtures develop into a detonation from a weak spark ignition source?*

To address this question, we defined four tasks that, in conjunction with well-defined experiments, will allow us to answer the question and give us the basis for understanding the results as well as extrapolating them to new situations. In summary, these tasks are:

1. Develop and test a model for stoichiometric methane-air combustion. Perform a series of simulations of flame propagation, acceleration, and possible DDT in channels with obstacles.
2. Develop and test similar models for fuel-rich and fuel-lean combustion.
3. Examine the effects of spatially varying fuel concentrations in a simulation.
4. Document the effects of stochasticity, i.e., of large-scale uncertainty in system behavior caused by minute perturbations in initial conditions or numerical procedures, on flame acceleration and DDT.

The progress in each of these areas is described below. In this exposition, we have moved the discussion of Task 4 to just after Task 1 because the tests were done on the stoichiometric mixture.

The final model developed must have the ability to compute the different stages of the evolution of a chemically reactive flow: ignition by a small spark, rapid flame acceleration, development of shocks, shock-flame interactions, and detonation initiation in complex geometries for natural gas mixtures with spatially and temporally varying stoichiometries. The solutions must come from the set of coupled, reactive Navier-Stokes equations (Eqs. 2.1–2.5). What we now describe are the first steps toward achieving this and a reliable predictive capability for DDT.

#### 3.1. DDT in Stoichiometric Methane-Air Mixtures (Task 1)

The items in Task 1 are the first, necessary steps in developing a multidimensional numerical model. The material presented here is described in more detail in references [9–13].

##### 3.1.1. Development of the Chemical Model: Parameter Calibration

Numerical models that can describe the behavior of shocks and detonations vary widely in their complexity, but for many practical situations, an extensive description of the details of the chemical pathways is expensive and unnecessary. Instead, it is more important to have an accurate model of the fluid dynamics coupled to a model for the chemical-energy release that puts the released energy in the “right” place in the flow at the “right” time. For detonations, direct shock ignition and subsequent propagation, as well as other more complex transient detonation structures, can be “accurately enough” computed if an acceptable representation of the chemical induction time (i.e., autoignition time) is known as a function of the state variables, temperature, and pressure [50]. Flame propagation and structure can be “accurately enough” computed with a model of energy release and diffusion coefficients that create a reasonable preheat zone [51].

The issue is always: “What is enough?” How accurate or detailed does the model have to be? This question has led to a series of simplified, single-step models for either flames or detonations [51–54] separately. What we need for prediction of DDT, however, is more demanding. We need a *single* model that will work for both combustion regimes. In previous work, we described similar single-step models for low-pressure acetylene, low-pressure ethylene, and atmospheric-pressure hydrogen-air mixtures [5–7, 41, 43, 44, 55]. Here we address the problem of developing a minimal model that captures the essential features of a flame, a detonation, and the deflagration-to-detonation transition (DDT) in methane-air mixtures.

Consider the physical phenomena we need to model. Flame acceleration in the laboratory frame occurs primarily due to advection by the induced gas flow, which can be orders of magnitude larger than the laminar and turbulent flame speeds [6, 7]. The gas flow is driven by thermal expansion of the combustion products and increases with the amount of heat released in a unit of time by the flame front, which is a function of the surface area of the flame. The flame surface area increases due to stretching by the flow and wrinkling caused by turbulent motions and fluid-dynamic instabilities. When the flow speed approaches the speed of sound, shocks form, and shock-flame interactions become an important mechanism for the flame wrinkling and turbulence generation. Hot spots, which can evolve to generate flames, shocks, and detonations, may arise in unreacted material from many types of interactions in a turbulent, shock-laden reactive flow. In these hot regions, a spatial temperature gradient exists, inside of which the temperature can be high enough to ignite the reactants. Ignition occurs consecutively in multiple layers of material heated to different temperatures, thus forming a reaction wave [40]. This wave can generate a strong shock and eventually a detonation. The survival of the newly formed detonation wave then depends on local thermal and chemical conditions and geometrical constraints [5].

Based on this progression of physical processes, the properties of the fuel-air mixture that are important during the flame-acceleration stage are the laminar flame speed  $S_l$ , the adiabatic flame temperature  $T_b$ , the viscosity  $\nu$ , the laminar flame thickness  $x_l$ , and the speed of sound  $c$ . In the work that follows, we assume that the gas mixtures behave as ideal gases, which means pressure  $P$  and internal energy  $\epsilon$  are related to the density and temperature by the state equations

$$P = \frac{\rho RT}{M}, \quad 3.1$$

$$\epsilon = \frac{P}{(\gamma - 1)}. \quad 3.2$$

Here the internal energy is  $\epsilon = E - \rho v^2/2$ , where  $E$  is the total energy and  $v$  is the velocity. The sound speed is given by  $c = \sqrt{\gamma RT}$ , and the specific heat capacity at constant pressure is related to the gas constant by  $c_p = \gamma R/(\gamma - 1)$ . The temperature rise in an adiabatic system due to chemical-energy release is  $T_b - T_o = q/c_p = q(\gamma - 1)/\gamma R$ . Thus, the adiabatic flame temperature  $T_b$  depends on the initial system temperature  $T_o$ , the heat release  $q$ , and the ratio of specific heats  $\gamma$ . The laminar flame speed also depends on  $q$  and  $\gamma$ , but it is also strongly influenced by the rate of chemical energy release, which is determined by the choice of reaction model. Here we assume that fuel,  $F$ , is converted to product,  $P$ , via a single reaction,  $F \rightarrow P$ , that has an Arrhenius dependence on temperature, characterized by a pre-exponential factor  $A$  and an activation energy  $E_a$ . The thermal diffusivity of the reactants,  $\kappa = K/\rho c_p$ , determines the length of the preheat zone of the laminar flame, and, thus, affects both  $S_l$  and  $x_l$ .

The late stages of DDT are controlled by induction delays behind strong shocks that correlate with some properties of detonation waves. Detonations are inherently unstable, leading to the formation of highly localized regions of high pressure and vorticity. Three shocks intersect to form the backbone of these regions, which are commonly referred to as triple points. Along the leading edge of the reaction front, one shock is a detonation wave and the second is an inert shock that has decoupled from the reaction front. A third transverse shock is inclined to the two leading shocks behind the leading edge. That shock can either be inert or reactive (a detonation). Several examples of triple points are shown below in Figure 3.5. The triple points move along the detonation front in the direction transverse to the direction of detonation propagation. The number and trajectory of triple points are characteristic of the properties of the gas mixture. When multiple triple points form along a detonation front, they leave behind a cellular pattern that has been observed in experiments. Since induction delays correlate with the size of these cellular structures, they can be used to calibrate a model that should approximately describe key phenomena responsible for the final stages of DDT. The detonation properties used for the calibration are the theoretical Chapman-Jouget (CJ) detonation velocity  $D_{CJ}$  and the detonation cell size  $\lambda$ . The velocity  $D_{CJ}$  depends only on the total amount of heat release and, hence, on  $q$  and  $\gamma$ . If the sound speed is correct,  $D_{CJ}$  gives an indication of the correct value of  $q$ , as  $T_b$  does for a deflagration. Ignition delay times also depend on the rate of chemical energy release. These delay times correlate well with the reaction zone structure, particularly with the characteristic size of the detonation cells,  $\lambda$ , which is controlled by  $q$ ,  $\gamma$ ,  $A$  and  $E_a$ .

The form of the model we are seeking for the reaction rate  $\dot{\Omega}$  is

$$\dot{\Omega} = A\rho Y \exp(-E_a/RT), \quad (3.3)$$

where  $Y$  is the fuel mass fraction. The transport coefficients, viscosity  $\nu$ , mass diffusivity  $D$ , and thermal diffusivity  $\kappa$  vary with temperature according to

$$\nu = \nu_o \frac{T^n}{\rho}, \quad D = D_o \frac{T^n}{\rho}, \quad \kappa = \kappa_o \frac{T^n}{\rho}. \quad (3.4)$$

The parameters  $\nu_o$ ,  $D_o$ , and  $\kappa_o$  are assumed to be constant, and  $n$  is a constant chosen to be 0.7. In this model, the ratio of specific heats  $\gamma$  does not vary with temperature. Target output for the quantities  $S_l$ ,  $T_b$ ,  $x_l$ ,  $D_{CJ}$ ,  $x_d$ , and  $\lambda$  for a stoichiometric (9.5%) methane-air mixture are given in Table 1.

**Table 1. Target Values for Output of Methane-Air Models**

Quantity	Lean (7%, $\phi = 0.72$ )	Stoichiometric (9.5%, $\phi = 1$ )	Rich (13%, $\phi = 1.43$ )
$S_l$	15–24 cm/s	34–45 cm/s	15–25 cm/s
$T_b$	1850–1940 K	2200–2330 K	1960–2000 K
$x_l$	0.17–0.2 cm	0.08–0.12 cm	0.18–0.25 cm
$D_{CJ}$	1680 m/s	1815 m/s	1800 m/s
$x_d$	0.8–1.6 cm	0.13–0.62 cm	0.69–1.1 cm
$\lambda$	$\approx 80$ cm	13–31 cm	$\approx 45$ cm

The model calibration is started by performing a series of one-dimensional calculations of flame and detonation structures for a range of input parameters. Then we choose a set of parameters that most closely reproduces *both* the laminar flame properties and the detonation properties. After this, two-dimensional simulations are used to compute detonation cell sizes using the model parameters arrived upon in the previous step. Finally, full simulations using the model parameters are used to compute flame acceleration and DDT, and these results are compared to experiments.

First, the values of  $\nu_0$  and  $\kappa_0$  were calculated directly from the known viscosity and thermal conductivity of air at 298 K and 1 atm. For simplicity, we assumed that the Lewis number ( $Le = \kappa_0/D_0$ ) of the mixture is equal to unity, i.e., that mass and heat diffuse at the same rate, so that  $D_0 = \kappa_0$ . This approximation is appropriate for mixtures of methane and air for which  $\kappa_o$  is only slightly larger than  $D_o$ . Assuming  $Le = 1$  greatly simplifies the one-dimensional analyses used to perform the model calibration. We then computed properties of a steady, one-dimensional laminar flame by solving an ordinary differential equation describing thermal conduction and energy release inside a steady-state reaction wave,

$$\frac{dF_t}{dx} = \rho \left( UC_p \frac{dT}{dx} - q\dot{\Omega} \right) \quad (3.5)$$

$$F_t = K \frac{dT}{dx} \quad (3.6)$$

where  $U = S_l \rho_0 / \rho$  is the flow velocity in the frame moving with the flame,  $F_t$  is the thermal flux, and  $\dot{\Omega}$  is the reaction rate given by Eq. (3.3). According to Eqn. (3.4), the thermal conductivity  $K$  is a function of temperature,  $K = \kappa \rho c_p = \kappa_0 T^{0.7} \rho c_p$ . Details of the solution method are given in [9, 56]. We search for a set of parameters,  $A$ ,  $q$ ,  $E_a$ , and  $\gamma$ , for which the computed value of  $S_l$  matches experimental data [57, 58], and that of  $T_b$  matches values calculated using a complex reaction mechanism for methane-air combustion [33]. The laminar flame thickness,  $x_l$ , is based on the temperature gradient, i.e.,  $x_l = (T_b - T_0) / \max |\partial T / \partial x|$ .

We use a Zeldovich-von Neumann-Doering (ZND) model to compute the half-reaction thickness of one-dimensional detonations using the same reaction model described above (Eq. 3.3) for a set of parameters  $A$ ,  $E_a$ ,  $\gamma$ , and  $q$ . The reaction zone of a one-dimensional detonation is described by

$$\frac{d\rho}{dt} = \frac{q\dot{\Omega}\rho(\gamma-1)}{(U^{*2} - c^2)} \quad (3.7)$$

$$\frac{de}{dt} = \frac{P}{\rho^2} \frac{d\rho}{dt} - q\dot{\Omega} \quad (3.8)$$

$$\frac{dx^*}{dt} = U^* \quad (3.9)$$

where  $e$  is the internal energy,  $t$  is time,  $x^*$  is the distance from the shock,  $U^* = D_{CJ} \rho_0 / \rho$  is the flow velocity in the shock frame,  $c = \sqrt{\gamma P / \rho}$  is the sound speed, and

$$D_{CJ} = c_0 \left( \sqrt{1 + \frac{q}{P_0} \frac{\rho_0(\gamma^2 - 1)}{2\gamma}} + \sqrt{\frac{q}{P_0} \frac{\rho_0(\gamma^2 - 1)}{2\gamma}} \right) \quad (3.10)$$

is the Chapman-Jouget detonation velocity. The solution procedure for this set of equations is described in detail in [9 56].

Solutions of Eqns. (5)–(8) give the reaction-zone profile, from which we find the half-reaction thickness of the one-dimensional detonation wave,  $x_d$ . This quantity correlates with the detonation cell size  $\lambda$  [59], which is often measured in detonation experiments. Even though detonation cells do not develop until after DDT occurs,  $\lambda$  is generally used instead of  $x_d$  in empirical correlations related to the detonation initiation and DDT [60–71]. For example, experimental evidence suggests that the ratio of the system size to  $\lambda$  must be greater than one for a sustained detonation to occur [60]. We use measured values of  $\lambda$  [72] (and, equivalently,  $x_d$ ) and values of  $D_{CJ}$  calculated using a thermodynamic equilibrium code (e.g., [73]) to find a set of consistent model parameters.

The choice of parameters  $\gamma$  and  $q$  determines  $T_b$  for laminar flames and  $D_{CJ}$  for one-dimensional detonations. Curves representing values of  $q$  that give  $T_b = 2210$  K and  $D_{CJ} = 1820$  m/s as a function of  $\gamma$  are shown in Figure 3.1a. We choose the values of  $q$  and  $\gamma$  at the intersection of these two curves to use in our model. The remaining parameters,  $E_a$  and  $A$ , determine  $S_l$  and  $x_d$  for fixed  $\kappa_0$ ,  $\gamma$  and  $q$ . The determination of  $\lambda$  for such a high-activation-energy mixture is not precise because the detonation cells are highly irregular. Hence, ranges for  $\lambda$  and  $x_d$  are given in Table 1. A representative value within the range shown in the table,  $x_d = 0.229$  cm, was used as the target value for the calibration process. Figure 3.1b shows the values of  $A$  for which  $S_l = 38.02$  cm/s and  $x_d = 0.229$  cm as a function of  $E_a$ . Again, we choose  $A$  and  $E_a$  at the point of intersection of these curves. Composite model values with their output quantities are shown in Table 2. We note, however, that a range of  $E_a$  and  $A$  exists that would give satisfactory values of  $\lambda$ .

**Table 2. Material, chemical, and reaction-wave parameters for stoichiometric (9.5%) methane-air**

Quantity	Value	Definition
<b>Input</b>		
$P_0$	1 atm	Initial pressure
$T_0$	298 K	Initial temperature
$\rho_0$	$1.1042 \times 10^{-3}$ g/cm <sup>3</sup>	Initial density
$\gamma$	1.197	Adiabatic index
$M_s$	27	Molecular weight
$A$	$1.64 \times 10^{13}$ cm <sup>3</sup> /g/s	Pre-exponential factor
$E_a$	$67.55 R T_0$	Activation energy
$q$	$39.0 R T_0 / M$	Chemical energy release
$\nu_0$	$3.6 \times 10^{-6}$ (g/s-cm-K <sup>0.7</sup> )	Transport constants
$\kappa_0 = D_0$	$6.25 \times 10^{-6}$ (g/s-cm-K <sup>0.7</sup> )	Transport constants
<b>Output</b>		
$S_l$	38.02 cm/s	Laminar flame speed
$T_b$	2210 K	Adiabatic flame temperature
$x_l$	0.0439 cm	Laminar flame thickness
$D_{CJ}$	1820 m/s	Chapman-Jouguet detonation velocity
$x_d$	0.229 cm	1D half-reaction detonation thickness

### 3.1.2. Description of Numerical Method and Validation of Basic Model

In order to properly compute DDT, a numerical model must be able to compute a wide variety of combustion waves, ranging from low-speed laminar flames to moderate-speed turbulent flames to high-speed detonations. In this section, we explore how the model developed in the previous section can be used to compute the limiting cases of this range of combustion waves: a laminar flame and a detonation. Here we present computations of two-dimensional unsteady laminar flames and detonations and compare them to the idealized, steady-state 1D flame and detonation structures computed in Section 3.1.1.

The code used to perform these validation tests and all subsequent simulations described in Sections 3 and 4 solves the RNSE using an explicit, second-order, Godunov-type numerical scheme incorporating a Riemann solver. The domain is discretized using a structured adaptive mesh based on the fully threaded tree data structure [74]. The mesh refinement is dynamically controlled by gradients of density, temperature, and composition.

#### 3.1.2a. Laminar Flame Structure

Equations 2.1–2.5 in conjunction with the calibrated reaction model (Eqn. 3.3 and Table 2) were solved using the standard explicit, second-order, numerical scheme described above. We consider a thin (in the  $y$ -direction), two-dimensional channel that is initially filled with premixed methane and air. An initial approximation for a planar laminar flame is placed across the domain so that the reaction wave propagates into the fresh reactants in the positive  $x$ -direction. After a short adjustment period, the correct laminar flame profile forms, and the flame propagates at a constant velocity,  $S_l$ . Here we compare the computed flame structure and propagation speed to those obtained with the 1D steady-state approximation described earlier. We consider two different grid resolutions at the flame front,  $dx_{min} = 0.018125$  cm ( $\approx 3$  computational cells per laminar flame thickness) and  $dx_{min} = 0.00113$  cm ( $\approx 39$  cells/ $x_l$ ). Away from shocks and flame fronts, the maximum computational cell size was taken to be  $dx_{max} = 0.29$  cm.

Figure 3.2 shows the 1D flame structure calculated for these two different grid resolutions along with the 1D steady-state solution (lines). The high-resolution calculation reproduces the theoretical flame structure and gives nearly the same flame speed,  $S_l = 38.02$  cm. There are some differences in the reaction-rate profiles calculated at lower resolution ( $dx_{min} = 0.018125$  cm). The computed laminar flame speed is approximately 12% smaller than the theoretical laminar flame speed. More resolution tests are discussed below in Task 4. Here we only note that when we compute DDT in larger channels,  $dx_{min}$  is limited by the available computational resources, and in most cases, the simulations must be somewhat under-resolved. The coarser resolution simulation shown in Figure 3.2 was chosen to reflect the minimum amount of grid resolution we used in the subsequent DDT simulations.

#### 3.1.2b. Detonation Structure

Multidimensional instability of gas-phase detonations results in a complex, dynamic structure at a detonation front. This structure involves multiple transverse waves and triple-shock configurations that interact with each other, causing the energy release to be highly nonuniform [75]. The size and regularity of a detonation cell characterize the kinetics of energy release: the cell size correlates with the energy-release rate and the regularity is controlled by the effective activation energy  $E_a/RT_{ZND}$ , where  $T_{ZND}$  is the post-shock temperature in the ZND-detonation structure. An example of a very regular structure formed in a

low-pressure mixture highly diluted by an inert gas is shown in [75].

Some reactive systems, such as methane-air, show even more complex detonation cell structures. For example, fine cellular structures may appear embedded inside main detonation cells. In some cases, such fine cellular structures may be caused by two distinct stages of energy release that occur at different timescales [76, 77]. In many cases, however, multilevel cellular structures can be explained by secondary instabilities of overdriven parts of the detonation front that can even appear in systems with a one-step energy release and high  $E_a/RT_{ZND}$ . Analysis of experimental data [78] and numerical simulations [79–81] show that secondary detonation cells appear for  $E_a/RT_{ZND} > 6.5$ .

We have now performed a series of extremely high-resolution unsteady numerical simulations of detonations propagating in a stoichiometric methane-air mixture. This is a very high-activation energy system,  $E_a/RT_{ZND} = 17.2$ , and, accordingly, the simulations show the formation of multiple levels of cellular structures caused by the propagation of very irregular triple-shock configurations [10]. The simulations show two main types of triple-shock configurations: one in which there was a triple-shock configuration with an attached transverse detonation, and another triple-shock configuration with an inert transverse wave. These combine to produce three types of collisions, which seem characteristic of a system of highly irregular structures with very high-activation energy. Here we describe these simulations in more detail. Later in this report (Section 4) we relate the results of these simulations to recent experimental cell measurements at NIOSH Lake Lynn Laboratory (LLL).

The system was modeled by solving the same set of equations with the same AMR approach to adaptive gridding as was used to perform the 2D flame calculations in Section 3.1.2.a and all of the DDT simulations described below. It has been shown that such models capture most of the key features responsible for the formation of detonation cells, including the effects of chemical kinetics on cell regularity and formation of secondary cell structures [79–81]. We consider a two-dimensional rectangular channel of height 32 cm and length 1024 cm. Using 2D simulations allows us to achieve a very high numerical resolution in the current calculations that would be prohibitively expensive in 3D. Based on previous experiments [72] and calculations [59], the channel height is large enough to capture at least one detonation cell. A significant number of computational grid cells was needed to resolve the instabilities in the detonation front properly. The smallest grid size used in these computations was 1/1024 cm, which is equivalent to about 234 cells per half reaction thickness. Details of the ignition method is given in [10]. Figure 3.3 shows the speed of the leading edge of the computed detonation front as a function of time. The average propagation speed of 1813 m/s is consistent with the CJ detonation velocity (1820 m/s), as defined by thermodynamic parameters.

Locally, the shape and the velocity of the detonation front are dictated by the dynamics of primary triple-shock configurations that form as a result of the inherent instability of a planar detonation. At times, the leading edge of the front is an overdriven detonation with velocity greater than  $D_{CJ}$ , and at other times a decoupled shock-flame complex with velocity less than  $D_{CJ}$ . A sequence of density fields taken from the calculations at several instants over a characteristic detonation-cell crossing time are shown in Figure 3.4.

The various types of triple-shock configurations appearing in the computation are analyzed in detail in [10] and are shown in Figure 3.5. Most of the primary triple-shock configurations we see in the simulations involve transverse detonations that propagate through the large induction zone (labeled 3 in the figure) behind weak parts of the leading shock (1). A close-up view of the temperature field in the vicinity of a

typical triple-shock configuration is shown in Figure 3.5a. The transverse detonation wave (2) is nearly perpendicular to the leading shock (1), and burns most of the unreacted material (3) behind it. Even the material in the small triangular region between the oblique shock (4) and the slip line (5) detonates, in contrast to the case with lower  $E_a/RT_{ZND}$  computed in [80], where it did not burn and left behind an unreacted tail.

Occasionally, we saw a different type of triple-shock configuration: a transverse detonation failed and became an inert transverse shock (9). One of these configurations is shown in Figure 3.5b. Here, the material detonates only in the overdriven part of the leading front (6). A variation of this situation is shown in Figure 3.5c where only a small part of the transverse detonation survives. A thin layer of material is burned in this region in addition to the burning in the overdriven part of the leading front. These types of configurations leave behind large pockets of compressed, unburned material (8) that may become completely surrounded by burned gas when two triple points collide, which can limit the total amount of energy released near the reaction front and limit the propagation velocity of the detonation.

Since both types of triple-shock configurations shown in Figure 3.5 exist in the same system, three types of collisions between triple-shock configurations are possible. The examples from the current simulation are shown in Figure 3.6. Isolated unreacted pockets form when at least one of the colliding transverse waves is inert. If another transverse wave is a detonation (Figure 3.6b), then it continues to propagate into the pocket after the collision and burns the compressed material. If both transverse waves are inert (Figure 3.6a), then the pocket drifts downstream and burns as a deflagration. Collisions between two triple-shock configurations with reactive transverse shocks (Figure 3.6c) result in significantly weaker reflected triple shocks since there is very little unburned material behind the leading edges of detonation.

Due to the high activation energy in the model used in these calculations, both transverse detonations and the overdriven parts of the leading front are unstable. They produce the smaller triple-shock configurations that can be seen in Figure 3.6. For overdriven parts of the leading front, these secondary instabilities increase in size with the distance from the primary triple point (Figure 3.6a). The spacing between the secondary triple points varies from fractions of a millimeter to several millimeters. The instability of transverse detonations occurs at even smaller scales of the order of 0.1 mm or less that are not well resolved in the simulations.

Finally, we emphasize that the unstable detonation front modeled here is very irregular. Even though characteristic length scales associated with primary triple points can be approximately estimated, the distinction between primary and secondary triple-shock configurations often becomes blurred. The detonation instabilities can be observed for all range of scales, from about a half of the channel width down to the grid resolution. This leads to the formation of a very complicated detonation cell structure. While it is difficult to make quantitative assessments of cell sizes and regularity, the numerical results obtained using the reaction model described in Section 3.1.1 qualitatively agree with experimental results. Direct comparisons with experiments performed at LLL will be discussed in a later section.

### 3.1.3. Channels with Obstacles

We next use Eqns. (2.1–2.5) to calculate multidimensional, turbulent, accelerating flames and subsequent DDT. Obstructed channels promote faster flame acceleration than smooth channels and, hence, provide a useful geometry in which to study DDT. In addition, this configuration has been used for several experimental studies, and so there is data that can be used for comparisons. A schematic of the channel used in the calculations is shown in Figure 3.7.

We consider three different configurations chosen to be similar to experimental systems [72, 82] and summarized in Table 3. For each test case, the channel is uniformly filled with a stoichiometric methane-air mixture.

- *Configuration 7.6.* Here  $L = 216.2$  cm,  $d = 7.6$  cm, which models the  $7.6 \times 7.6$  cm square channel used in [82]. In the experiments, both ends of the channel were closed, and the initial pressure in the unburned gas mixture was 47 kPa ( $\sim 1/2$  atm).
- *Configuration 17.4.* Here  $L = 1187.8$  cm,  $d = 17.4$  cm, which is similar to the circular cross-section tube (diameter 17.4 cm) used in [72]. Here, the right end of the channel is open to the atmosphere, and the initial gas pressure is atmospheric, as in the experiments.
- *Configuration 52.* Here  $L = 2130$  cm,  $d = 52$  cm, which is similar to the 52 cm diameter tube used in [72], where the channel is also open to the atmosphere at  $x = L$ .

**Table 3. Configurations for Simulations**

Configuration	7.6	17.4	52
$L$ (cm)	216.2	1187.8	2130
$d$	7.6	17.4	52
$\xi$	1/3, 2/3	0.3, 0.6	0.3, 0.6
$x = l$ boundary	closed	open	open
$P_o$ (atm)	0.464	1	1
Cross-section, experimental channel	square	circular	circular
Experiment reference	[82]	[72]	[72]

To ignite the mixture in the simulation, we placed a quarter-circular region of hot, burned material at the left wall on the centerline and added a small amount of extra energy to the burned region. The additional energy per unit mass is on the same order of the chemical energy release, which could model ignition by a low-energy ( $\sim 100$ mJ) spark. The resulting shock wave is very weak and not nearly strong enough to ignite a detonation directly. It does, however, cause multiple shock reflections and shock-flame interactions that distort and wrinkle the flame front.

We have shown that it is possible to compute the behavior of a propagating laminar flame with a resolution of 5 computational cells across the thickness of the reaction front. For a propagating detonation, however, we required over 200 computations cells across the detonation front thickness to properly compute the dynamics of the unstable detonation. Here we are most concerned with the acceleration of flame and the transition to detonation and less interested in computing the large-scale instabilities of the detonation

front. Hence, in the simulations described below, we use the grid resolution required for the laminar flame thickness and do not try to fully resolve the detonation structure.

### 3.1.3a. Configuration 7.6

In the experiments [82], obstacles of heights 1.27, 1.9, and 2.53 cm corresponded to blockage ratios of  $\xi = 1/3$ ,  $1/2$ , and  $2/3$ , respectively, on both the top and bottom walls. Both ends of the chamber were closed. The pressure of the stoichiometric methane-air mixture inside the chamber was initially 47 kPa. The mixture was ignited by an electric spark at the centerline of the channel.

We simulated a two-dimensional rectangular channel (Figure 3.7) with obstacle spacings and heights as in the experiments. After ignition, we tracked the position and velocity of the leading edge of the flame front as well as the total length of flame surface created as the flame evolves. Flame velocities were computed at discrete locations along the length of the channel and represent an average velocity over the interval between two successive measurement locations. The flame surface was calculated by summing the total length of the isosurface on which  $Y = 0.5$  at a particular instance in time. Figure 3.8 compares measured and computed flame velocities and flame surface areas for  $\xi = 1/3$  and  $\xi = 2/3$ . At early times in the flame development, the simulations and experiments showed similar flame velocities for both blockage ratios. Differences arose further downstream ( $x \sim 100$ – $150$  cm) as the flame evolved.

The flame acceleration process occurs in three phases, each of which can be characterized by the dominant mechanism driving the growth in flame surface area. In the first phase, the flame is folded and stretched by a laminar flow field that is induced by the thermal expansion of the combustion products. The development of flame surface is similar for  $\xi = 1/3$  and  $2/3$  for this phase,  $x \leq 70$  cm (Figure 3.8c). Temperature maps of the leading edge of the flame as it passes over the first obstacle are shown in Figures 3.9a,b. There is relatively little wrinkling of the flame front during this phase.

In the second phase, the predominant mechanism for increasing the total length of flame surface is wrinkling by fluid dynamic instabilities (e.g., Kelvin-Helmholtz and Rayleigh-Taylor) and turbulent fluctuations. Localized regions of vorticity stretch and fragment the flame front, thereby increasing the total amount of flame surface area. The energy released at the flame surface causes the thermal expansion of the product gases, which causes a net flow through the channel. Shear layers develop downstream of obstacles as the fluid is accelerated through the restricted cross-sectional area above them. Fluid dynamic instabilities and turbulence in the shear layers contribute to generation of more flame surface area. The flame surface and velocity become substantially larger for  $\xi = 2/3$  than  $\xi = 1/3$  for  $x > 70$  cm. In this case, the shear layers develop more quickly, since the flow is accelerated to a higher velocity in the smaller gap between obstacles.

Temperature maps of the flame fronts near  $x = 100$  cm, Figures 3.9c and d, show that there is much more small-scale flame structure and therefore much more flame surface in the  $\xi = 2/3$  case. The increase in total flame surface (see Figure 3.8c) continues as long as substantial amounts of fuel remain in between obstacles behind the foremost part of the flame front. Then, when most of this fuel is depleted, the flame surface decreases rapidly. The maximum flame surface developed for  $\xi = 2/3$  is larger than that for  $\xi = 1/3$  because the increased velocity of the flame front allows the flame to propagate farther in the channel before extended reaction zones can burn out. The extra amount of flame surface present in these regions results in faster depletion of the fuel, and hence the steep drop in flame surface for  $x \geq 130$  cm.

This rapid decline in flame surface is slowed as the flame enters the third phase. When the speed of the

induced flow approaches the speed of sound in the unburned mixture ahead of the flame, energy released at the leading edge of the flame front generates weak pressure waves that propagate ahead of the flame. These pressure waves later become shocks, which can reflect from obstacles and walls. The reflected shocks also collide and interact with portions of the reaction front. The flame surface is wrinkled by these shock-flame interactions that promote Richtmyer-Meshkov instabilities. The turbulence generated by these instabilities is not, necessarily, homogeneous, isotropic, Kolmogorov turbulence. The nature of this turbulence and its interaction with the flame are interesting areas of future investigation. Here, the additional energy release caused by flame-surface wrinkling helps to sustain the flame speed and slow the decline in the net flame surface. This process occurs for  $x > 160$  cm for  $\xi = 2/3$ , but does not begin to occur in the  $\xi = 1/3$  case until the flame reaches the end of the domain. A longer channel would be necessary to observe significant shock-flame interactions for the  $\xi = 1/3$  case. Figures 3.9e,f compare the temperature maps for  $\xi = 1/3$  and  $2/3$  when the leading edge of the flame is near  $x = 200$  cm. A well-defined shock wave has formed in the  $\xi = 2/3$  case, but the waves ahead of the flame front have not yet coalesced into a shock for  $\xi = 1/3$ .

### 3.1.3b. Configurations 17.4 and 52

In the larger-diameter tubes used in the experiments [72], the obstacles were annular orifice plates spaced one diameter apart. The blockage ratio defined in these experiments is  $\xi^* = 1 - (D^*/D')^2$ , where  $D'$  and  $D^*$  are the tube diameter and orifice diameter, respectively. One end of the tube was left open to the atmosphere, and the initial gas pressure was atmospheric throughout the tube. The uniform stoichiometric methane-air mixture was ignited near the tube axis at the closed end. Photodiodes were placed at various positions along the walls of the tubes, and reaction-front velocities were calculated based on time-of-arrival measurements.

After the initial acceleration period, two regimes of propagation velocity were found. One of these, the “choking” regime described above, is characterized by a velocity close to  $1/2D_{CJ}$ . The second regime, the quasi-detonation regime, is characterized by a flame-front velocity just less than  $D_{CJ}$ . For a blockage ratio of  $\xi^* = 0.3$ , the experimentally measured flame speed fluctuates between the speeds typical of these two propagation regimes. This indicates that the 17.4 cm diameter tube is close to the critical size for detonation propagation, as supported by the observation that  $D'/\lambda < 1$  for the stoichiometric methane-air system. For the larger blockage ratio,  $\xi^* = 0.6$ , the experimental flame velocity approaches a steady value of approximately 700 m/s, a velocity characteristic of the choking propagation regime. Similar results were obtained for the 52.0 cm tube.

We performed simulations similar to these experiments using the configuration shown in Figure 3.7 with  $d = D'$  and  $\xi = \xi^*$  for configurations 17.4 cm and 52 cm. Because of the differences in geometry, the obstacle heights in the simulations,  $h$ , are slightly larger than the heights of the orifice plates in the experiments,  $h^* = (D - D^*)/2$ , for the same blockage ratios. Figure 3.10 shows the calculated flame velocities and surface areas as a function of the position of the leading edge of the reaction wave for  $\xi = 0.3$  and 0.6. Figure 3.11 shows maps of temperature (left column), pressure (center column), and velocity (right column) for a sequence of instances over the course of the simulation. In both the calculations and experiments, the flame accelerates to a fixed velocity characteristic of the choking regime, which then either undergoes DDT or continues to propagate at this average speed. The initial flame acceleration is similar to that described in the previous section: flames are stretched by the thermal-expansion-induced flow, wrinkled and torn by

turbulence and fluid dynamic instabilities, and further fragmented by shock-flame interactions. For example, the black line in each frame in Figure 3.12 shows the progress of a shock colliding with and passing through a flame. As the shock passes through, significantly more flame surface is created behind it. For the cases shown in Figure 3.10 and 3.11, the channel is long enough for the flames to progress through all stages of the acceleration process.

The evolution of flame surfaces for  $0 < x \leq 450$  cm shown in Figure 3.10c follows the same trend as in the early stages of configuration 7.6. For  $x \geq 450$  cm and  $\xi = 0.3$ , the flame surface sharply decreases. At this point, however, the reaction-front velocity jumps to  $D_{CJ}$ , indicating that a detonation was initiated and survived. The sequence of events that lead to DDT is shown in Figures 3.11i–m. Strong shock waves formed ahead of the flame front reflect off of the channel wall and the faces of obstacles, which results in even stronger waves and more shock-flame interactions. Eventually, Mach stems form and these raise the local temperature close to the ignition point. These regions of elevated temperature, or hot spots, may or may not ignite, depending on the ignition delay time of the mixture and the length of time the temperature remains elevated. The hot spot created by a Mach stem just beginning to reflect from the base of the obstacle in Figure 3.11j (rightmost obstacle in figure) leads to a successful detonation ignition. The detonation then propagates into unburned fuel, catches up to the leading shock wave, and proceeds to consume nearly all unburnt fuel in that region. This is qualitatively similar to the process reported for detonation ignition in hydrogen-air mixtures in channels with obstacles [6, 7]. The size of the system, however, is considerably larger for the methane-air mixture.

Velocity curves shown (Figure 3.10a) for  $d = 17.4$  cm and  $\xi = 0.3$  indicate that the detonation propagates at a speed much less than  $D_{CJ}$ . This reduction in velocity is a result of recurring detonation diffractions that continually decouple the flame from the leading shock. The detonation is then reignited at a subsequent obstacle in the manner discussed above. Although a detonation propagates at a speed greater than or equal to  $D_{CJ}$ , a fast deflagration (decoupled flame and shock) propagates significantly slower. Thus, the time-averaged velocity for this quasi-detonation, characterized by intermittent periods of detonation and fast deflagration propagation, is below  $D_{CJ}$ . An example of detonation failure and subsequent reignition is shown in Figures 3.11o–t. This repeated ignition and decoupling process leads to the observed smaller propagation velocities for this case.

Simulations of the  $d = 52$  cm channel were then performed for  $\xi = 0.3$  and  $\xi = 0.6$ . A sequence of temperature (left column), pressure (center column), and velocity (right column) maps near the leading edge of the flame front for  $\xi = 0.3$  are shown in Figure 3.13. The same progression of events observed for the  $d = 17.4$  cm channel can be seen. The first occurrence of DDT is shown in panels k–n. Detonation diffraction over an obstacle, shock-flame decoupling, and subsequent DDT is shown in panels o–t. The flame velocities obtained for both the  $\xi = 0.3$  and the 0.6 cases are shown in Figure 3.14. For  $\xi = 0.3$ , the computed and measured flame velocities are very similar during the initial flame acceleration period ( $x \leq 700$  cm). Near 700 cm, DDT occurs in the simulated system and the computed velocity jumps to  $\sim 1800$  m/s. This propagation speed is much closer to  $D_{CJ}$  than that observed in configuration 17.4,  $\xi = 0.3$  since fewer instances of shock-flame decoupling take place in the larger channel. In the experiments, DDT first occurs farther downstream, near  $x \sim 1000$  cm, and the quasi-detonation velocity is somewhat smaller than the calculated value. For  $\xi = 0.6$ , the computed flame acceleration is close to the experimental data. In the

simulations, several instances of DDT were observed, while no DDT occurred in the experiments. The total flame surface for the  $\xi = 0.6$  simulation is everywhere greater than that of the  $\xi = 0.3$  simulation. Larger pockets of unburned fuel between obstacles take longer to burn and delay the onset of the rapid decline in flame surface area that occurred in configurations 7.6 and 17.4 for the larger blockage ratios. By the time the pockets of fuel begin to burn out, the leading edge of the propagating flame has already accelerated to the point where frequent shock-flame interactions significantly increase the amount of flame surface, leading to less rapid net losses of flame surface area.

### 3.1.4. Sensitivity of the Model to Small Parameter Variations

It is important to evaluate the sensitivity of the computed flame acceleration and of DDT to variations in the parameters of the chemistry model. We first consider the sensitivity of the flame acceleration by evaluating how much velocity profiles change when there are systematic variations in the length and time scales of the laminar flame. This is done by changing model parameters  $A$ ,  $q$ ,  $E_a$ , and  $\gamma$  to create moderate (10-15%) variations in the laminar flame velocity, adiabatic flame temperature, and specific-heat ratio. We next consider the impact on DDT of changing these parameters. As discussed earlier, model parameters also affect various length and time scales of detonation waves, in particular,  $D_{CJ}$ ,  $\lambda$ , and ignition delay times.

**Table 4. Configurations for Parameter Sensitivity Study**

$\mathcal{P}$	1	2	3	4	5
$A$ (cm <sup>3</sup> g-s)	$1.64 \times 10^{13}$	$1.2 \times 10^{13}$	$1.64 \times 10^{13}$	$4.411 \times 10^{13}$	$1.64 \times 10^{13}$
$E_a/RT_0$	67.55	67.55	69.45	67.55	67.55
$qM/RT_0$	39.0	39.0	39.0	34.71	34.82
$\gamma$	1.197	1.197	1.197	1.197	1.226
$S_l$ (cm/s)	38.02	32.0	32.0	38.02	38.02
$T_b$ (K)	2210	2210	2210	2000	2210
$D_{CJ}$ (m/s)	1820	1820	1820	1724	1854
$x_d$ (cm)	0.229	0.331	0.356	0.332	0.0616

The first question to address is how changes in model parameters affect the velocity of the flame in an obstructed channel. To test this, we performed a series of simulations using configuration 17.4 with  $\xi = 0.3$  and 0.6 and varying parameters in the model. A description of the parameter sets (denoted  $\mathcal{P}$ ) and the corresponding laminar flame and 1D detonation properties is given in Table 4.

First consider different sets of parameters that yield the same  $T_b = 2210$  K but different values of the 1D laminar flame speed. (In Table 4, these are  $\mathcal{P}1$ – $\mathcal{P}3$ .) Figure 3.15a shows that the results were nearly identical for all three cases with  $\xi = 0.6$ , and only slight differences between  $\mathcal{P}3$  and  $\mathcal{P}1$  were found later in the flame development for  $\xi = 0.3$ . These simulations suggest that, in the range of  $S_l$  considered, the laminar flame speed has negligible influence on the evolution of the flame propagation speed in the channel.

The effect of the adiabatic flame temperature on the flame acceleration was tested by changing the amount of heat released per unit mass of fuel, while maintaining a constant  $S_l$ . To test this, we compare  $\mathcal{P}1$

and  $\mathcal{P}4$ . Figure 3.15b shows the flame acceleration computed using these two parameter sets, which suggest this 200 K temperature difference has no noticeable effect on flame acceleration. The effect of varying  $\gamma$  (and, hence, the sound speed) on the flame acceleration is shown in Figure 3.15c, which compares  $\mathcal{P}1$  and  $\mathcal{P}5$ . Again, only slight differences between the two cases are noticeable for both  $\xi = 0.3$  and 0.6.

The second important issue is how the choice of model parameters affects the onset of the DDT. As we discuss later in this report, it is difficult to treat this issue in a truly quantitative manner because DDT is a stochastic process that depends on the formation of relatively small hot spots, and these result from combinations of shock reflections or turbulent fluctuations. In some situations, even seemingly imperceptible changes in any physical or numerical parameters or background conditions can lead to significant random variations of distances or times to detonation initiation [6]. Even with these caveats, we should still be able to get a qualitative idea of the likelihood of DDT for a given parameter set.

A detailed discussion of the results shown in Figure 3.16, which is the downstream section of the channels for the cases shown in Figure 3.15, is given in [9]. Here we summarize that discussion by observing that the results for  $\xi = 0.3$  are consistent with changes in chemical induction times and  $E_a$ , which in turn affect the time of detonation onset. This sensitivity is not observed for  $\xi = 0.6$  which does not show the transition. The choice of  $\gamma$  (more precisely,  $\gamma - 1$ ) plays a large role in detonation initiation and propagation. Using  $\mathcal{P}5$ , we investigate how increasing  $\gamma - 1$  by 15% (so that  $\gamma = 1.226$ ) affects the transition to detonation. For  $\xi = 0.3$ , the detonation propagates as a quasi-detonation in a manner similar to that observed using set  $\mathcal{P}1$ . For  $\xi = 0.6$  and large  $\gamma$ , there are several instances of detonation initiation and failure. The transitions are infrequent, and the average propagation velocity is smaller than  $D_{CJ}$  and the quasi-detonation propagation velocities observed for the  $\xi = 0.3$  cases.

The results shown in Figure 3.15 and Figure 3.16 indicate that varying the model parameters to result in relatively small (10 – 15%) changes in individual laminar flame properties has little impact on the observed flame acceleration. In general, the effects on DDT are also small. It is not clear whether the differences in the first occurrence of DDT among the several parameter sets shown in Figure 3.16a are due to physical differences in the modeled systems or to chance fluctuations in the thermodynamic conditions within the hot spots that initiate detonations. The changes in model parameters for  $\mathcal{P}2$  and  $\mathcal{P}3$  both have the effect of increasing induction delay times behind shocks (an effect that could delay DDT), but the resulting first occurrences of DDT appeared later and sooner than the baseline case, respectively. Small changes in the thickness of the detonation wave (and detonation cell size) result in correspondingly small changes in the average propagation velocity and first occurrences of DDT unless the system is near a critical value for detonation propagation. In such a system, even a small increase in detonation cell size could impede DDT. In systems sufficiently larger or smaller than the critical size for DDT for a given fuel mixture, the interaction of the induced flow and shocks with the wrinkled flame surface seems to have a much larger influence on the large-scale behavior of the reaction front than the details of the model chemistry in these types of obstructed channels.

There are other physical properties of the gas mixture that have not been discussed here that could potentially impact the first occurrence of DDT. For instance, the ratio of the acoustic time in the Zeldovich reactivity gradient to the reaction time [83] has been shown to be relevant to the development of a detonation [84]. It is not possible to vary the reaction time and the induction time independently using a one-step

reaction model. This could be done with a multiple-step reaction model, but at a higher computational cost. Evaluating whether solutions obtained using a multiple-step reaction model would produce more accurate results and, if so, whether the improvement justifies the additional computational costs is left for future investigations. Likewise, we have not discussed how changes in the laminar flame thickness affect flame acceleration. The thickness of the flame influences its ability to become wrinkled and distorted by shocks and fluid-dynamic instabilities, which in turn greatly affects the total energy release rate. We will return to this important issue in Sections 3.3 and 3.4.

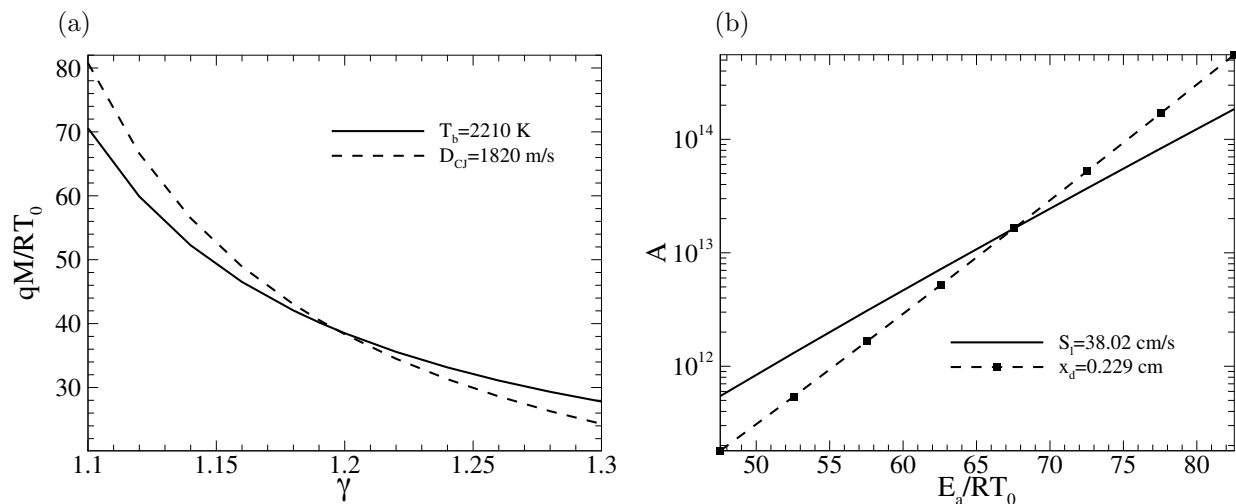


**Figure 3.1.** Parametric curves for which (a)  $T_b = 2210$  K,  $D_{CJ} = 1820$  m/s and (b)  $S_l = 38.02$  cm/s,  $x_d = 0.229$  cm. The points of intersection in the two figures give the values of  $qM/RT_0$ ,  $\gamma$ ,  $E_a/RT_0$ , and  $A$  used in conjunction with the single-component reaction model (Eq. 3.3).

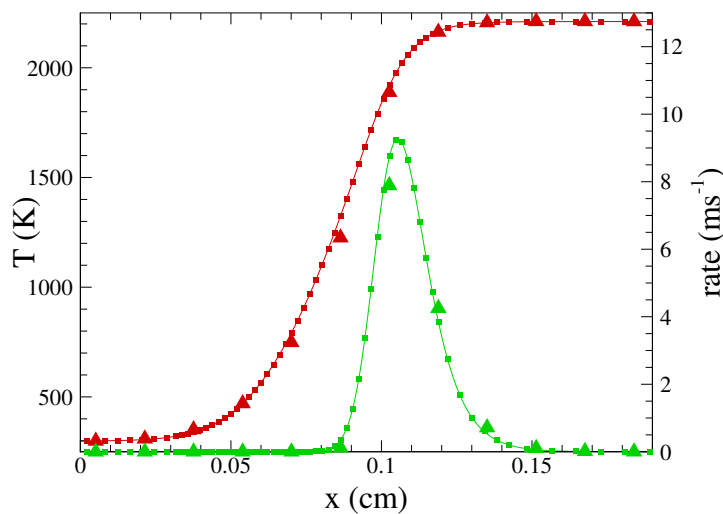


**Figure 3.2.** Temperature (red) and reaction-rate (green) profiles for a laminar flame calculated using Eqs. (3.5–3.6) (lines), two-dimensional Navier-Stokes equations (Eqns. 2.1–2.5) with  $dx_{min} = 0.018125$  cm (triangles), and the two-dimensional Navier-Stokes equations (Eqns. 2.1–2.5) with  $dx_{min} = 0.00113$  cm (squares).

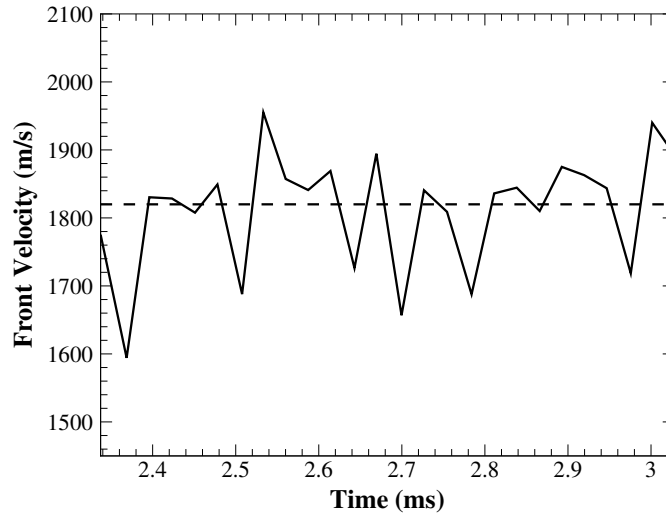


**Figure 3.3.** Front-propagation velocity as a function of time after the denotation has reached a quasi-steady propagation speed of 1813 m/s (solid line) and  $D_{CJ}$  for a stoichiometric (9.5%) methane-air mixture (dashed line).

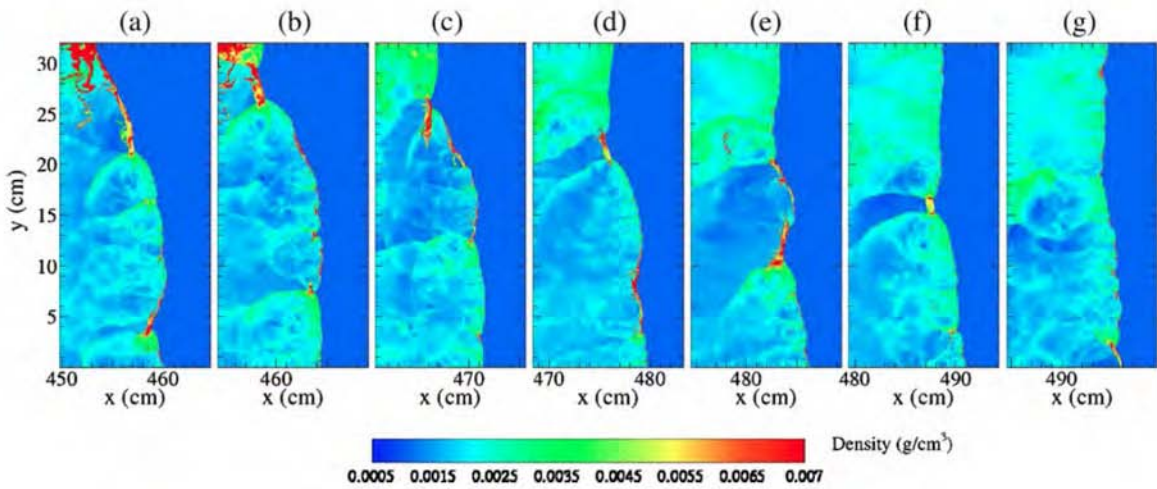


**Figure 3.4.** Selected density maps of the full channel width in the vicinity of the detonation front at times (a)  $t = 2.480$  ms, (b)  $t = 2.505$  ms, (c)  $t = 2.542$  ms, (d)  $t = 2.586$  ms, (e)  $t = 2.620$  ms, (f)  $t = 2.648$  ms, and (g)  $t = 2.677$  ms after initiation.

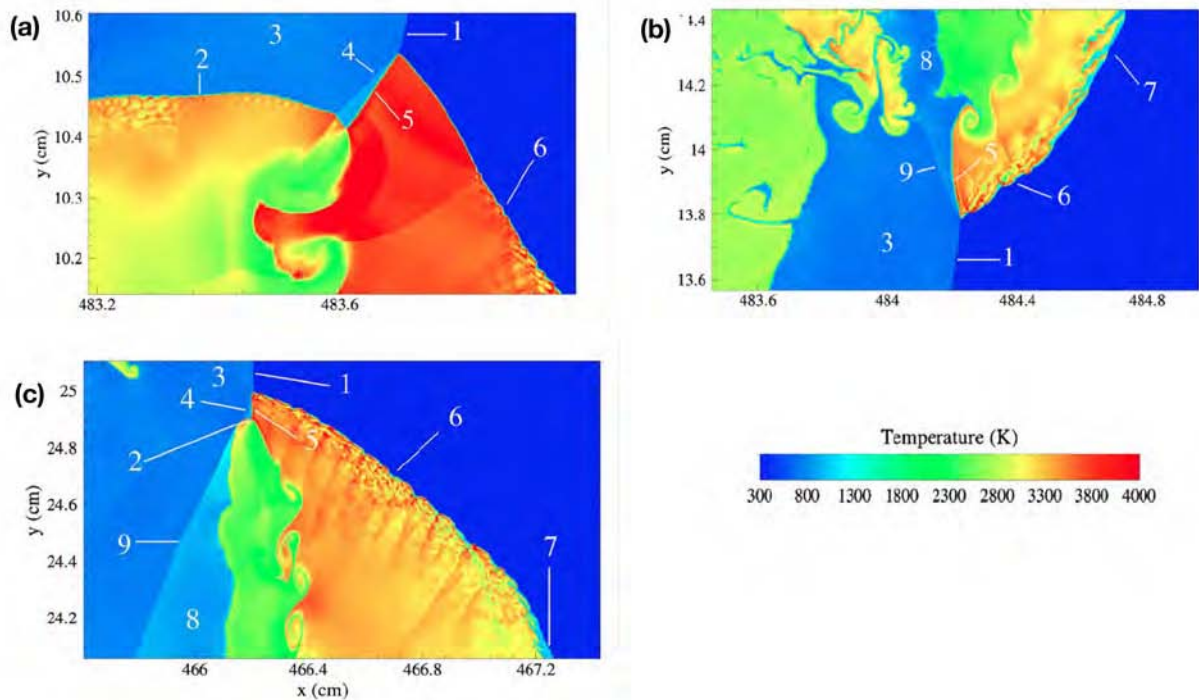


**Figure 3.5.** Temperature maps near (a) a triple-shock configuration to which a transverse detonation is attached, (b) a triple-shock configuration where detonation occurs at the leading edge but not in the transverse wave, and (c) a triple-shock structure showing characteristics of both (a) and (b), and for which the transverse wave is a detonation between the oblique shock and slip line and an inert shock farther away from the leading edge. Structures shown in the figure include (1) leading inert shocks, (2) transverse detonations, (3) induction zones (unreacted material), (4) oblique shocks, (5) slip lines, (6) overdriven detonations, (7) decoupled shocks and reaction zones, (8) pockets of unreacted material, and (9) inert transverse shocks.

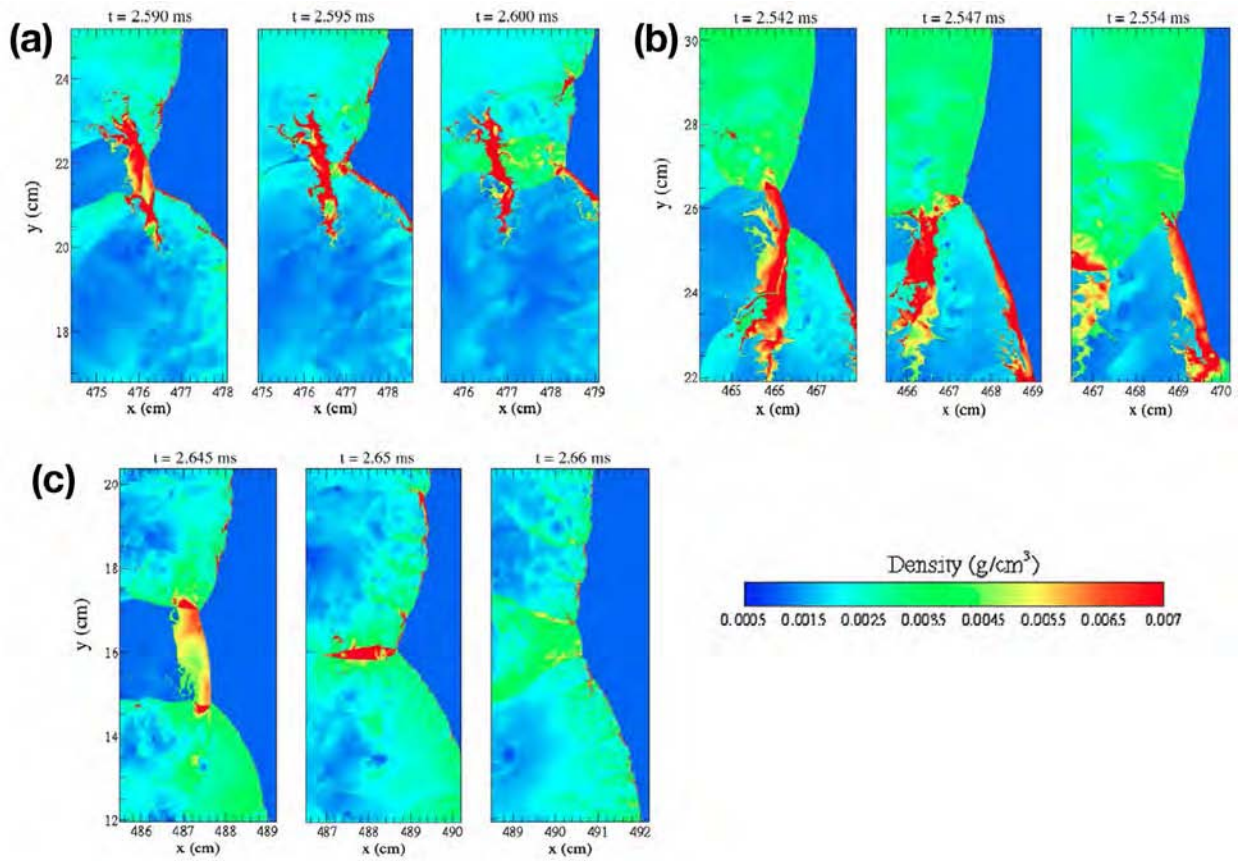


**Figure 3.6.** Density maps near several representative triple point collisions: (a) two triple points with inert transverse waves, (b) one triple point with transverse detonation and one with an inert transverse wave, and (c) two triple points with transverse detonations. Time increases from left to right in each figure.

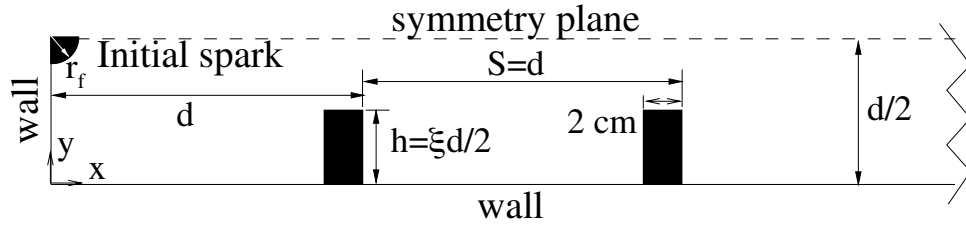


**Figure 3.7.** Schematic of general two-dimensional channel with obstacles used in DDT calculations. We assume the channel is symmetric and simulate only the lower half, so symmetry conditions ( $\partial u/\partial y = \partial Y/\partial y = \partial T/\partial y = \partial P/\partial y = v = 0$ ) are applied at the channel center line,  $y = d/2$ . The obstacles are taken to be 2 cm thick, and their heights are set based on the desired blockage ratio,  $\xi = 2h/d$ . Spacings between obstacles are set equal to  $d$ , and the obstacles fill the entire length of the channel. Walls and obstacle surfaces are adiabatic no-slip reflecting boundaries. Calculations are initialized by placing a quarter-circular region of burned material in the upper left corner of the domain. This initial flame radius is 0.25 cm in all calculations.

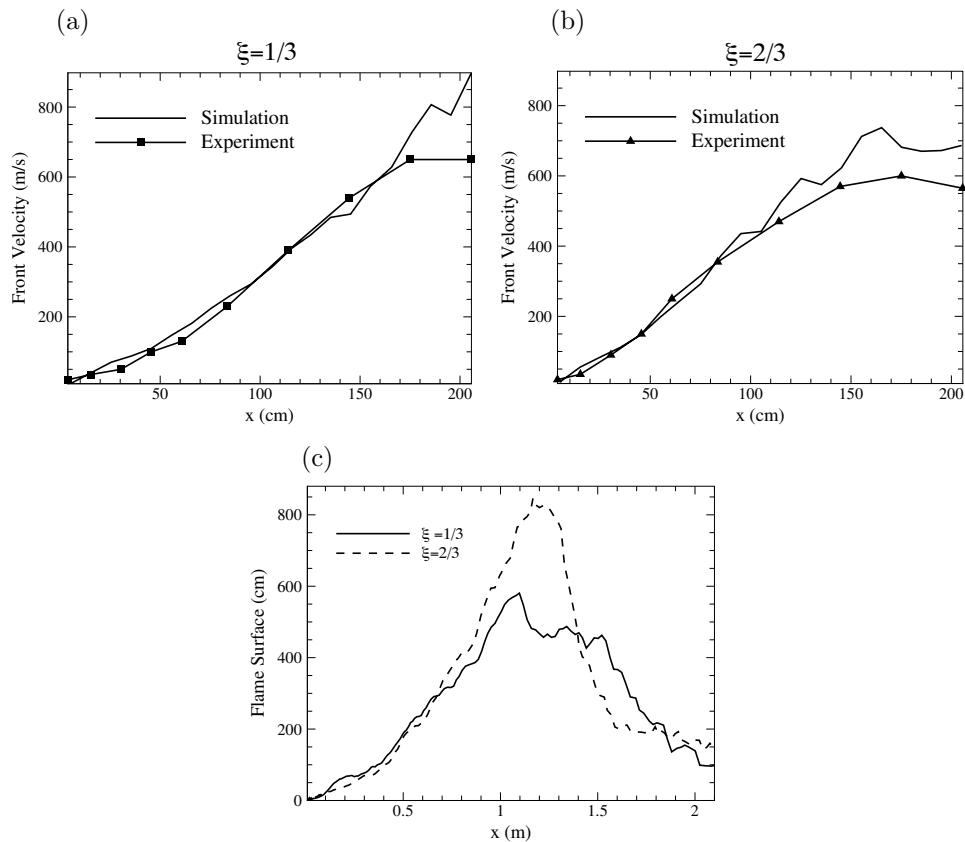


**Figure 3.8.** Configuration 7.6: (a and b) Computed and measured [82] flame-propagation velocities and (c) computed flame-surface as a function of the position of the leading edge of the reaction front.

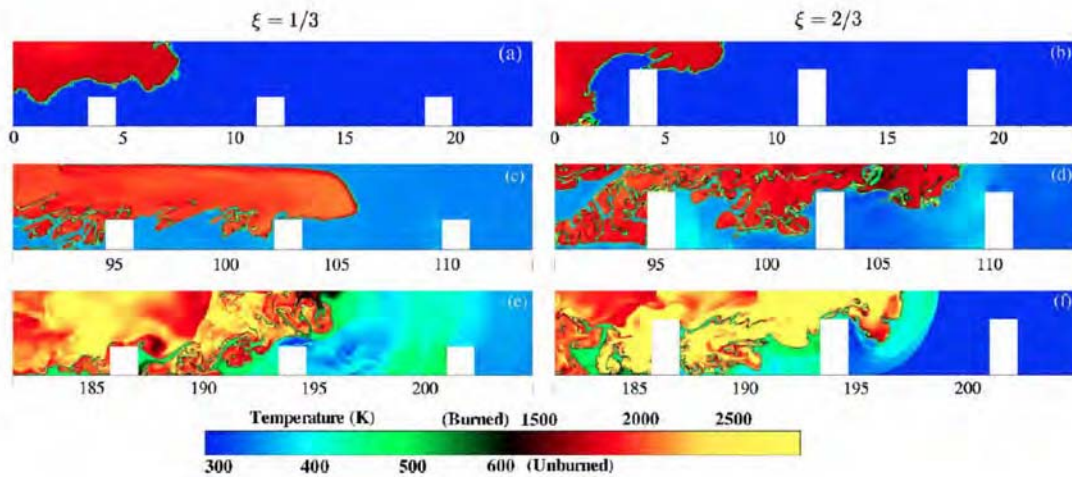


**Figure 3.9.** Temperature maps near the leading edge of the flame for configuration 7.6 with  $\xi = 1/3$  (left) and  $\xi = 2/3$  (right) at several locations throughout the channel: (a and b) near first obstacle, (c and d) near  $x = 100$  cm, and (e and f) near  $x = 200$  cm. The top temperature scale is for burned material, and the bottom scale is for unburned material. Time increases from top to bottom in each column.

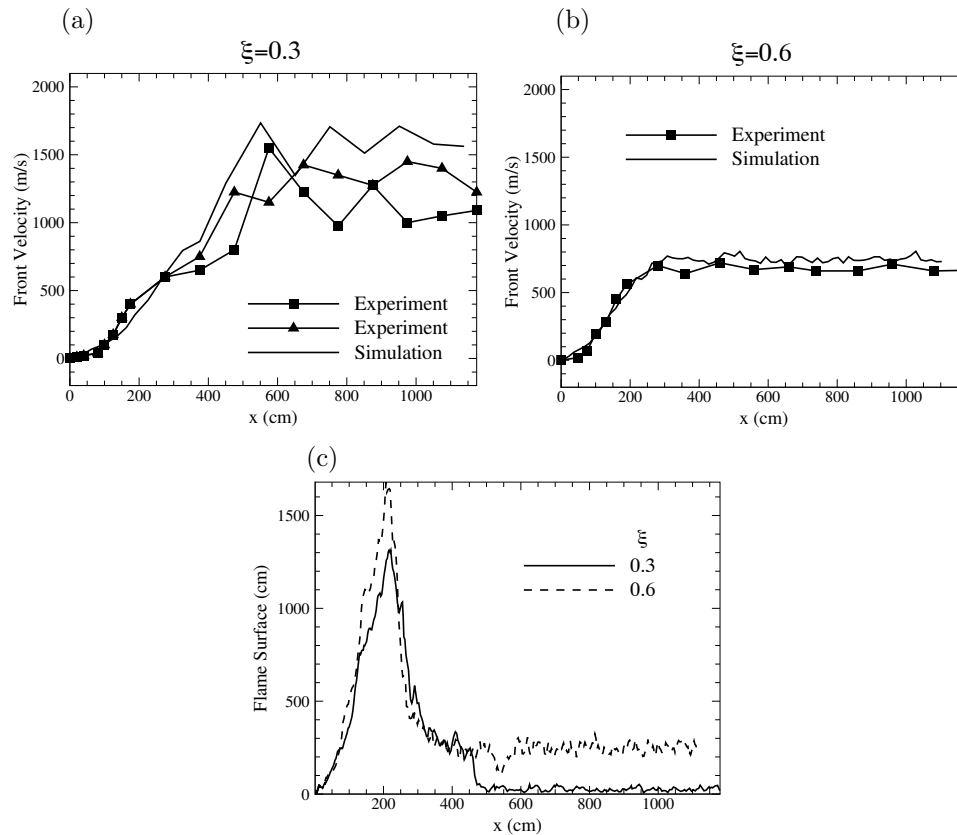


**Figure 3.10.** Configuration 17.4: (a and b) Computed and measured [72] reaction front-propagation velocities and (c) calculated flame-surface lengths as a function of the position of the leading edge of the reaction front.

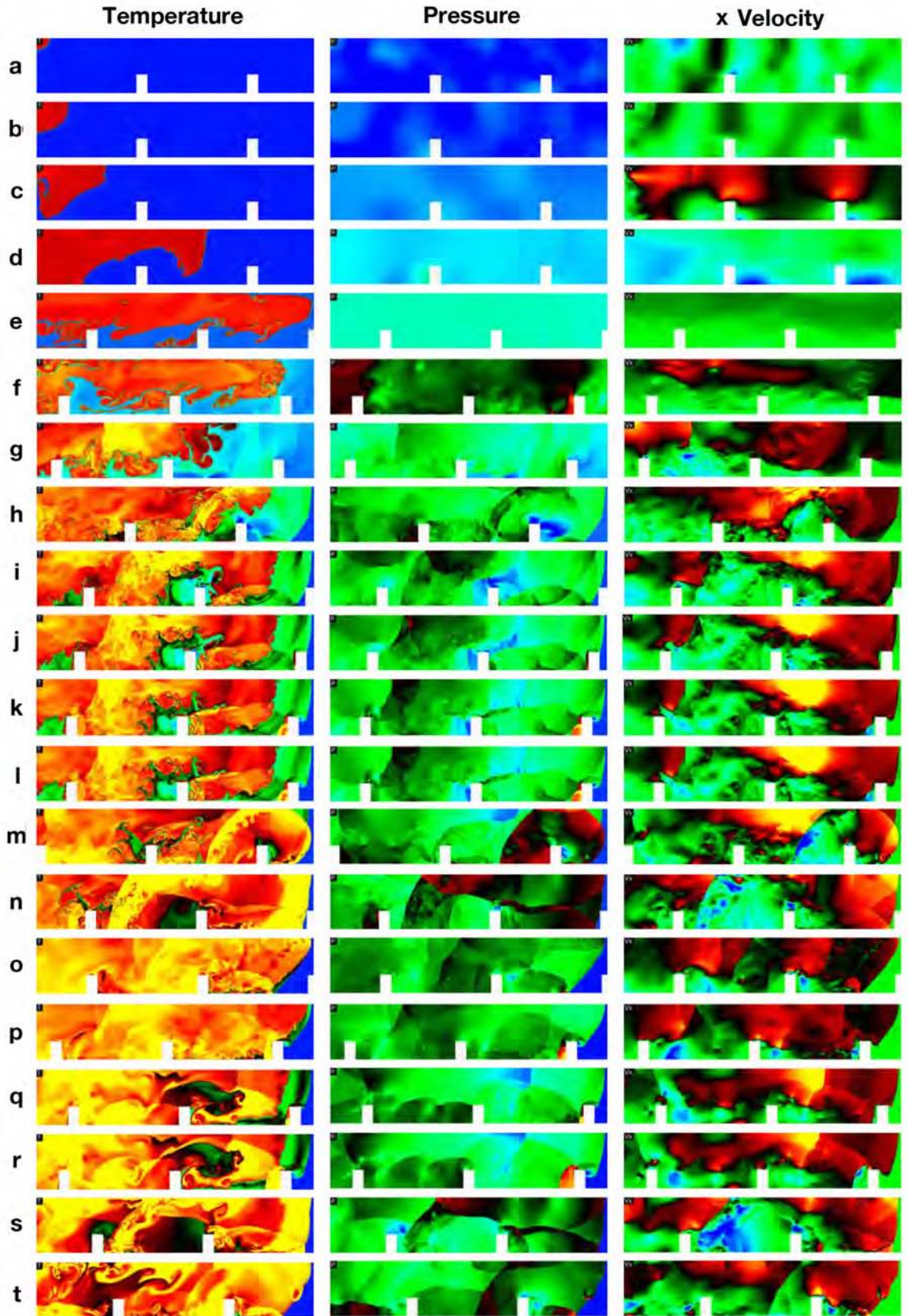
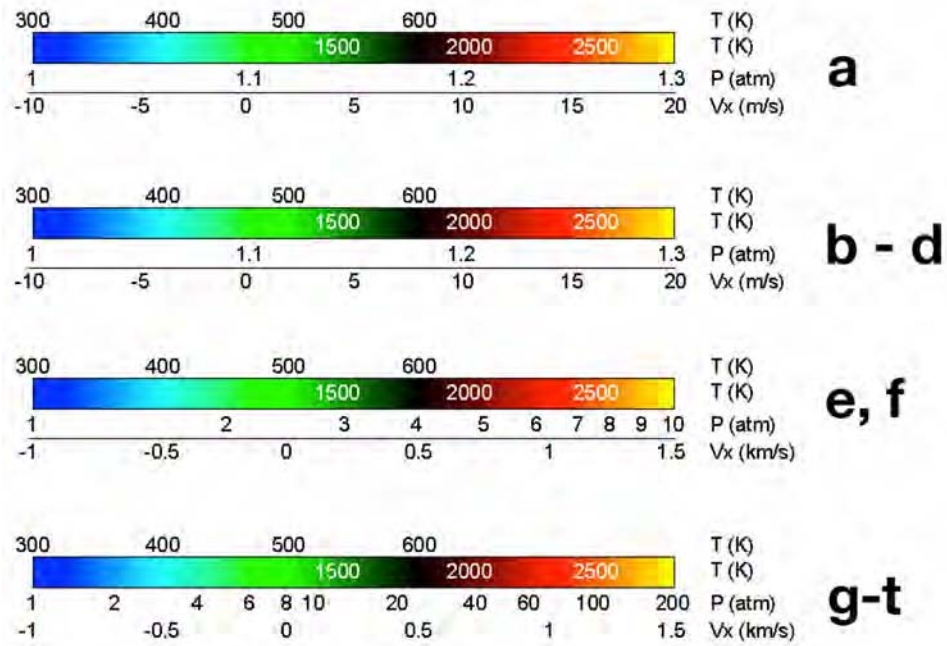
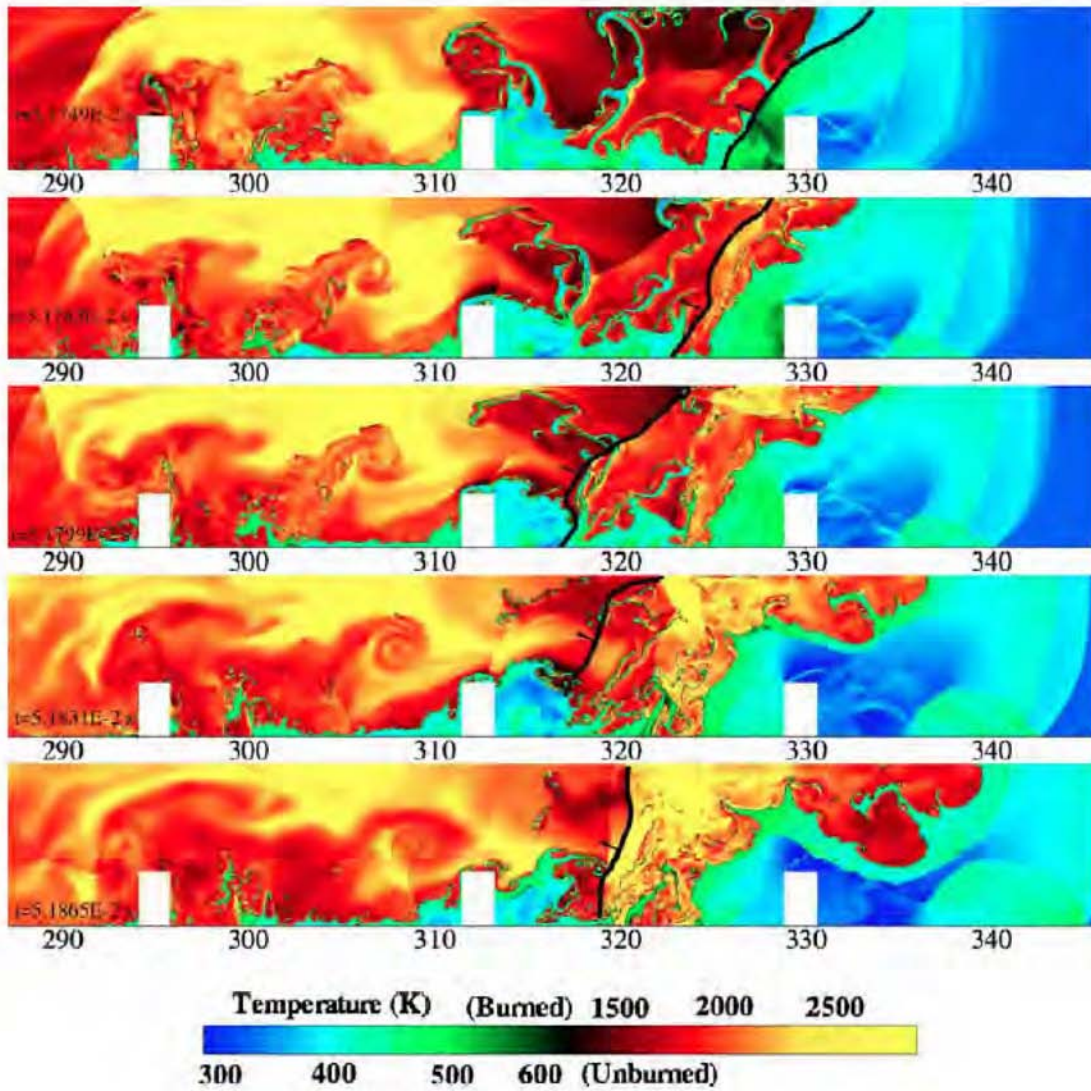


Figure 3.11. Legends and caption on next page.



**Figure 3.11.** Configuration 17.4: Temperature, pressure, and  $x$ -velocity sequences (see previous page) in the simulation of flame acceleration and DDT in an obstructed channel with  $\xi = 0.3$ . Pressure and velocity scales change with time as the static pressure and bulk velocity in the channel grow while the flame is accelerating. There are two temperature scales, as indicated in the legends above. The upper scale (cooler) refers to the unburned gas, the lower scale (hotter) refers to the burned gas. The letters on the left side refer to the frames on the previous page.



**Figure 3.12.** Temperature maps near the leading edge of flame in configuration 17.4 with  $\xi = 0.3$  as a shock interacts with the flame front. The heavy black line indicates the location of a shock, and the arrow indicates the direction of propagation. The top temperature scale is for burned material, and the bottom scale is for unburned material. Time increases from top to bottom.

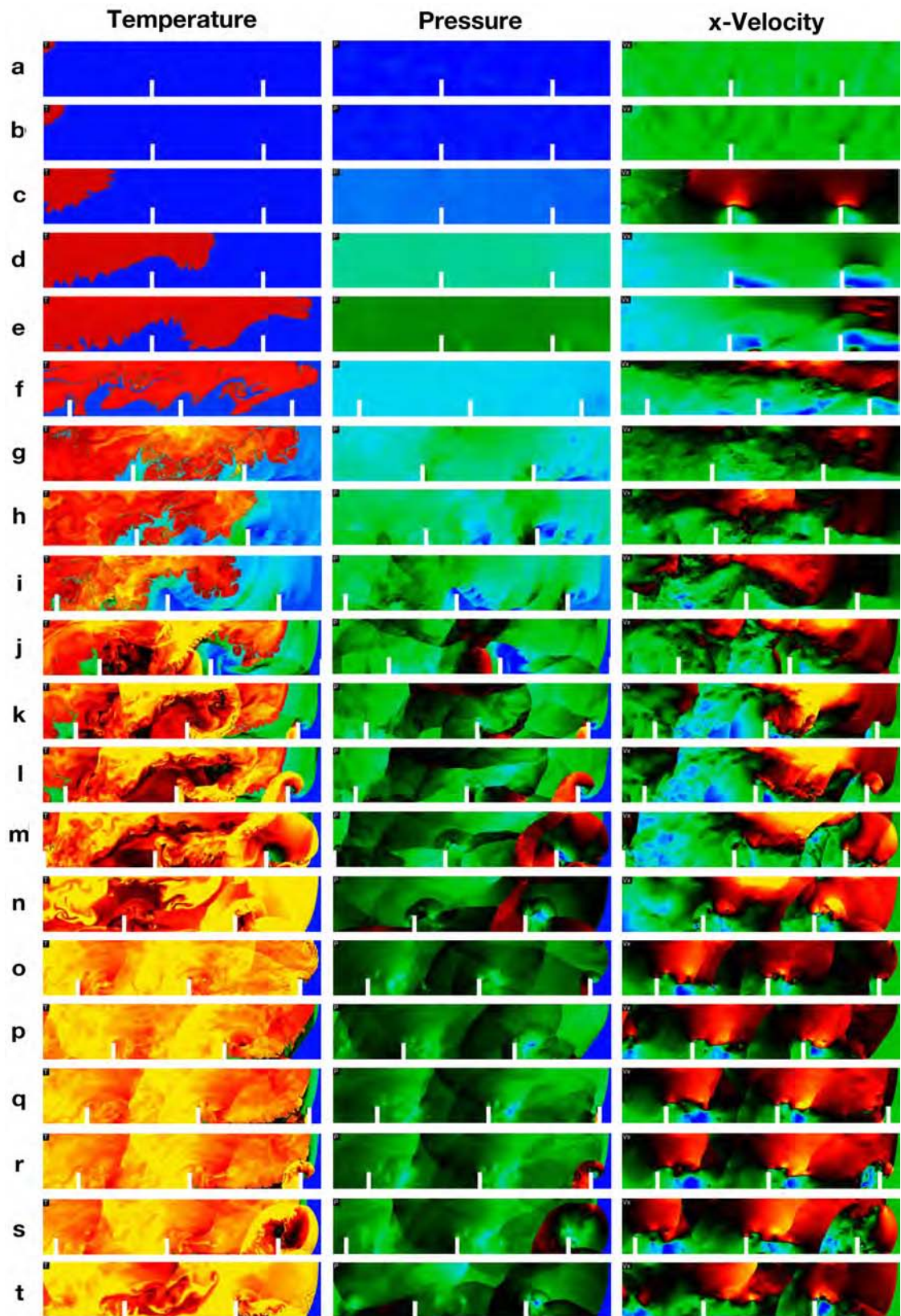
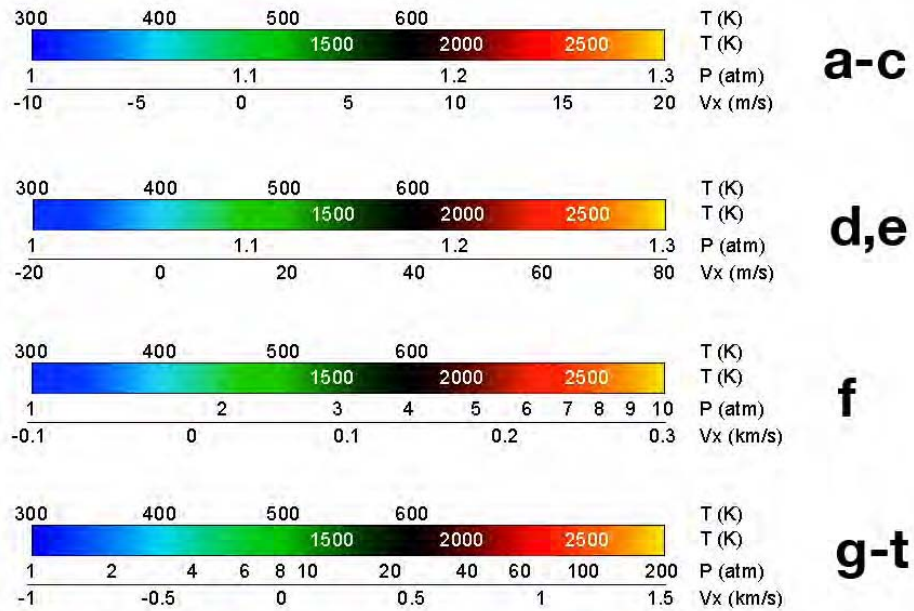
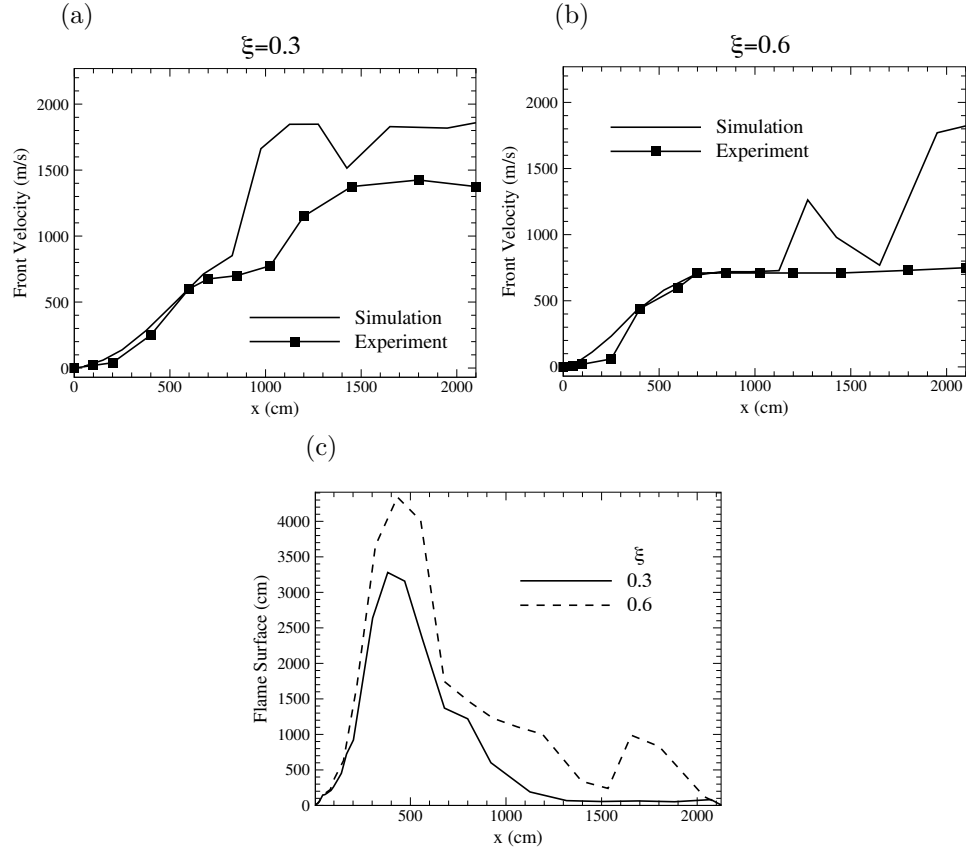


Figure 3.13. Legends and caption on next page.



**Figure 3.13.** Configuration 52: Temperature, pressure, and  $x$ -velocity sequences (see previous page) in the simulation of flame acceleration and DDT in an obstructed channel with  $\xi = 0.3$ . Pressure and velocity scales change with time as the static pressure and bulk velocity in the channel grow while the flame is accelerating. There are two temperature scales, as indicated in the legends above. The upper scale (cooler) refers to the unburned gas, the lower scale (hotter) refers to the burned gas. The letters on the left side refer to the frames on the previous page.



**Figure 3.14.** Configuration 52: (a and b) Computed and measured [72] reaction front-propagation velocities and (c) calculated flame-surface lengths as a function of the position of the leading edge of the reaction front.

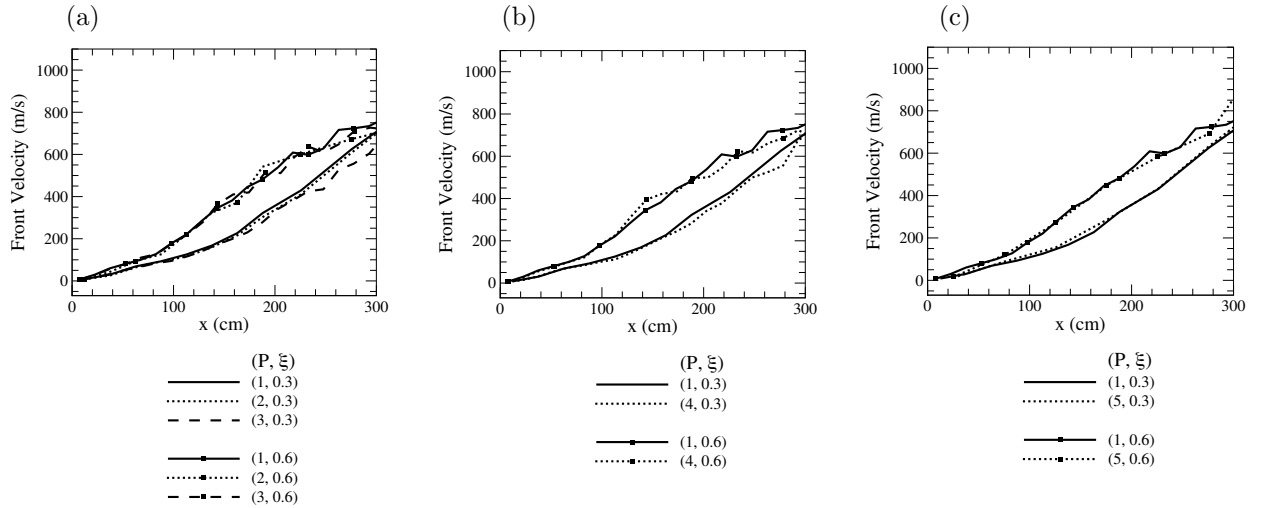


**Figure 3.15.** Reaction front-propagation velocities as a function of the position of the leading edge of the reaction front for  $x < 300$  cm in configuration 17.4 calculated using parameter sets,  $\mathcal{P}$ , (a) 1, 2, 3, (b) 1, 4, and (c) 1, 5. See Table 4 for descriptions of the parameter sets. Lines with symbols represent  $\xi = 0.6$ , and those without represent  $\xi = 0.3$ .

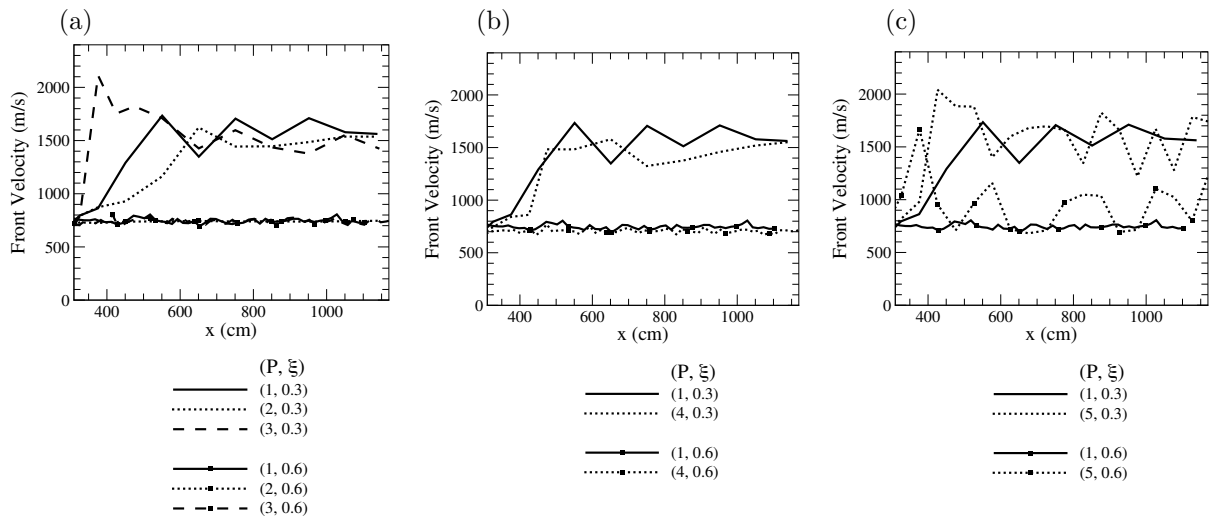


**Figure 3.16.** Reaction front-propagation velocities as a function of the position of the leading edge of the reaction front for  $x > 300$  cm in configuration 17.4 calculated using parameter sets,  $\mathcal{P}$ , (a) 1, 2, 3, (b) 1, 4, and (c) 1, 5. See Table 4 for descriptions of the parameter sets. Lines with symbols represent  $\xi = 0.6$ , and those without represent  $\xi = 0.3$ .

### 3.2. Stochasticity and Resolution (Task 4)

Stochasticity is the ability of a process to deviate randomly from its mean path. Experimental observations show that DDT is a stochastic process in the sense that there is some uncertainty in time and location for the detonation initiation. This uncertainty is an important aspect of the DDT that involves multiple stochastic phenomena, including flow instabilities, turbulence, many interactions between shocks, flames, and vortices, and the resulting hot-spot formation. Since the detonation usually arises from one of many hot spots that stochastically appear in the system, detonation initiation also becomes stochastic. Small fluctuations in density, temperature, and composition play an important role in the development of stochasticity in experimental systems, which are also affected by uncertainties in initial conditions. The real cause of stochasticity, however, is embedded in the complexity of underlying physical phenomena and is present in RNSE-based numerical models that describe these phenomena.

High-Reynolds number flows, those for which we can only reasonably resolve a portion of the range of turbulent scales, are stochastic in the sense that they are very sensitive to minute changes in computational parameters. Small variations in reaction rates, initial conditions, background conditions, features of the computational grid, and even in the numerical roundoff that occurs at a particular time in the simulation, can change the exact time and location when various features of the flow arise and interact or are quenched. The issue of stochasticity in computations of DDT is closely related to numerical resolution tests, since changing the computational cell size affects a non-converged solution, and triggers a stochastic response at the same time. When stochastic deviations are comparable to the systematic effect of numerical resolution, the effects of resolution cannot be properly evaluated without estimating the dispersion of the results related to stochastic properties of the system.

How such small-scale perturbations affect the large-scale behavior of a system is a question largely unaddressed in turbulent reacting flows because of their physical complexity and the high costs of the simulations. It is important, however, to understand whether a particular DDT mechanism is, in fact, robust to small variations in a turbulent, stochastic flow.

#### 3.2.1. Background

Our previous experience with DDT simulations has shown that some systems are more susceptible to the stochastic behavior than others, depending on geometries and initial conditions involved.

In the earliest DDT computations for low-pressure acetylene and ethylene [41,43, 44], we did not observe any significant stochastic behavior, though no systematic studies of stochasticity were performed for these systems. These computations showed excellent convergence with changes in the computational grid. This suggests that systematic effects of numerical resolution were not altered by any significant random deviations. Stochastic effects were observed in computations of DDT in obstructed channels [6] that included both numerical convergence studies and dedicated stochasticity tests. The latter were based on background temperature variations in the range  $dT = \pm 0.01\text{K}$  that were too small to cause any systematic effects. All other model parameters, including the numerical resolution, were kept constant. Multiple computations performed for these slightly different background temperatures showed practically no effect on the initial flame acceleration, but revealed moderate stochastic dispersion for the run-up distance to DDT. This dispersion was of the order of 20% for the larger obstacle spacing  $S > d$  (Configuration 1 in Section 2.3.3), and of

the order of 40% for the smaller obstacle spacing  $S < d$  (Configuration 2 in Section 2.3.3). These tests were repeated for several numerical resolutions and showed that stochastic deviations were comparable to systematic effects of numerical resolution.

### 3.2.2. Methane Tests

Now we describe the stochasticity, model sensitivity, and numerical resolution tests performed for flame acceleration and DDT in the stoichiometric methane-air mixture. We first describe these tests individually, and then discuss the implications for producing a predictive computational ability for DDT.

#### 3.2.2a. Laminar Flame Resolution

The numerical issue of how much grid resolution is necessary at the reaction front becomes extremely important when attempting to simulate flame acceleration and DDT for very large-scale explosions. A major constraint on the size of the system that can be simulated is set by the number of small cells required to obtain a sufficiently accurate description of the reacting flow. Thus, it is useful to know the largest cell size that can be used to meet this requirement. Our previous tests have shown that the amount of resolution required to produce the correct laminar flame speed depends strongly on the complexity of kinetics and diffusion used in the model. We have seen above that the methane-air flame with a single Arrhenius step, which is a rather simplified chemical-diffusion model, needs to be resolved with only three cells to propagate with the approximately correct velocity. In previous studies [85], which used full chemical reaction models, we found that we needed 20–50 cells to resolve the flame thickness, depending on the number of species in the model. Because of the significant sensitivity of the flame speed and subsequent acceleration for multispecies models, resolution tests of such models were even more crucial if the results were expected to be quantitatively or even qualitatively correct.

The next level question, one that goes beyond isolated laminar-flame resolution, is what is the resolution required to describe the flame correctly in the flame-acceleration region of an entire flow calculation. This depends not only on the resolution at the front, but the influence of other properties of the flows, including instabilities and turbulence that also depend on resolution. Here we break this issue into two parts. First, we have addressed the question: What is the resolution needed at the front to achieve the correct flame acceleration?

We tested the effect of the reaction front resolution on flame acceleration in configuration 7.6 defined in Table 3 with  $\xi = 1/3$  using the model parameters shown in Table 2. In all cases, the flame was initiated from a spark of size  $r_f = 0.25$  cm. Three values of  $dx_{min}$  were tested, 0.018124 cm (corresponding to  $\sim 3$  computational cells per laminar flame thickness), 0.009062 cm ( $\sim 5$  cells/flame thickness), and 0.004531 cm ( $\sim 10$  cells/flame thickness). Figure 3.17a shows the computed propagation velocity of the leading edge of the flame, and Figure 3.17b shows the development of the flame surface, both as a function of the position of the leading edge of the flame. As the minimum grid size is decreased, and the flame front becomes more resolved, the peak amount of flame surface increases. The computed flame velocity during the later stages of the flame acceleration process also increases when the number of grid cells in the reaction zone is increased from 3 to 5. A subsequent increase from 5 cells to 10 cells has little impact on the bulk acceleration of the flame.

### 3.2.2b. Background Flow Resolution

Our numerical model includes an adaptive mesh refinement, which means that the computational cell size in the vicinity of flames and shocks is significantly smaller than in the background flow, away from steep gradients. Since the maximum and minimum computational cell sizes can be changed independently, we can consider the effect of the resolution of the background flow on flame acceleration. There are two case studies for this: one for configuration 7.6 and another for configuration 17.4 (Table 3). First, consider configuration 7.6, which is shown in Figure 3.18. Here, the size of the finest computational cells in the vicinity of shocks and flame fronts were held fixed at  $dx_{min} = 0.018124$  cm while the largest grid sizes in the background flow were systematically decreased from  $dx_{max} = a = 0.211$  cm to  $a/8 = 0.0264$  cm. The flame acceleration increases noticeably as the grid sizes are decreased from  $a$  to  $a/2$  to  $a/4$ . Only small differences between the curves for  $a/4$  and  $a/8$  are visible, suggesting some level of grid convergence has been attained.

Next, consider configuration 17.4, which is the physically more difficult case because it leads to DDT, and the simulations summarized by the curves in Figure 3.19. As in the previous figure, the three curves represent cases for which we apply the same initial physical conditions and finest grid size, but vary the size of the coarsest computational grids. The two more resolved cases give very similar flame acceleration until just before DDT. In the least resolved case, the flame acceleration is notably slower. We can therefore consider the two more resolved cases as having acceptable background resolution. One explanation for this variation in flame acceleration from coarse to fine grids is that for finer background resolution, more of the turbulent length scales are resolved. This increase in resolution of the turbulence, in turn, means that finer-scale background effects contribute to flame-surface wrinkling, there is faster energy release, and hence faster flame acceleration.

### 3.2.2c. Stochasticity, Resolution, and DDT

The issue of multiple, interacting stochastic processes in DDT is one of the most difficult and important issues for safety and risk analysis. How much variation in the distance to DDT can we expect, given the stochastic nature of turbulence and hot-spot formation?

To investigate this point, consider again configuration 17.4. The two curves representing the most resolved simulations from Figure 3.19 are reproduced in Figure 3.20. The results of four other nearly identical simulations are also shown. The three green curves represent simulations performed with  $dx_{max} = 0.145$  cm, and for the three blue curves,  $dx_{max} = 0.0725$  cm. The differences between the curves of each particular color were minute variations in the initial system temperatures (0.01 K). These simulations, which are nearly identical physically, show a range of locations and timings in which DDT occurred. In fact, all of the simulations shown in Figure 3.20 have undergone DDT at about the same flame and shock velocity,  $\sim 1000$  m/s. In all cases, the flame acceleration is similar, but the transition occurs anywhere in about a 50 cm region, which, equates to three or four obstacle spacings. This corresponds to uncertainty of about 15% in the run-up distance to DDT, which is consistent with 20% uncertainty obtained in similar tests for hydrogen-air mixtures discussed above.

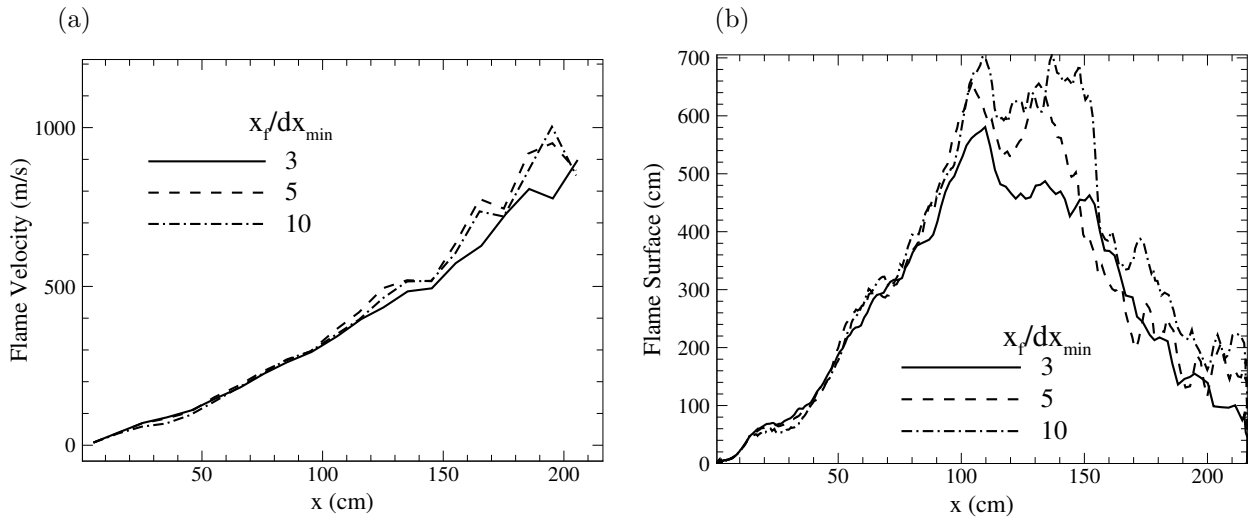


**Figure 3.17.** (a) Flame velocity and (b) flame-surface length as a function of position of leading edge of a flame for configuration 7.6,  $\xi = 1/3$  using three successively higher grid resolutions at the flame front, representing 3, 5, and 10 grid cells per laminar flame thickness.

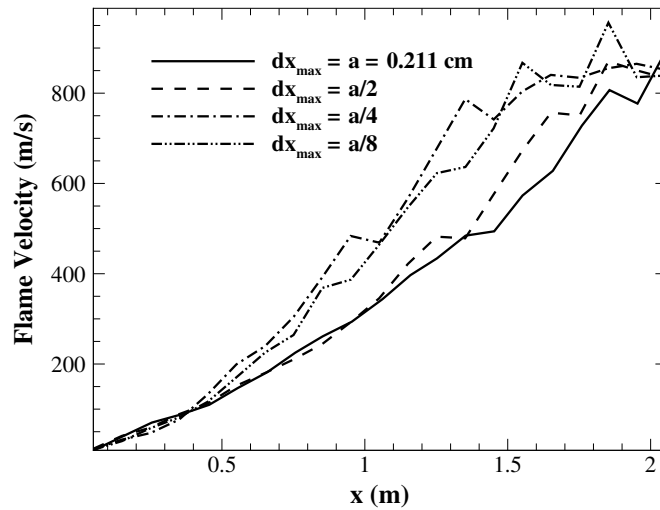


**Figure 3.18.** Flame velocity as a function of position of leading edge of a flame for configuration 7.6,  $\xi = 1/3$  using three successively higher grid resolutions *in the background flow*, so that the largest computational cells in the calculations were successively decreased by factors of 2, ranging from  $dx_{max} = 0.211$  cm to 0.026376 cm.

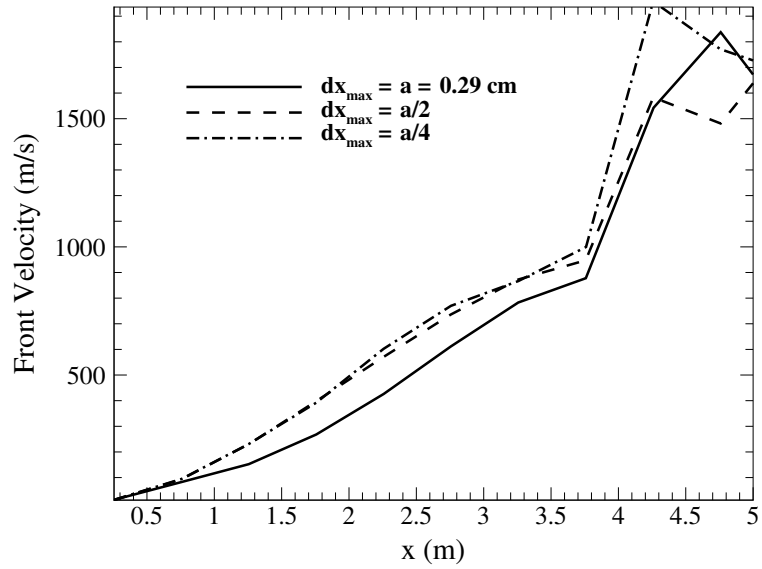


**Figure 3.19.** Flame velocity as a function of position of leading edge of a flame for configuration 17.4,  $\xi = 0.3$  using three successively higher grid resolutions *in the background flow*, so that the largest computational cells in the calculations were successively decreased by factors of 2, ranging from  $dx_{max} = 0.29$  cm to 0.07256 cm.

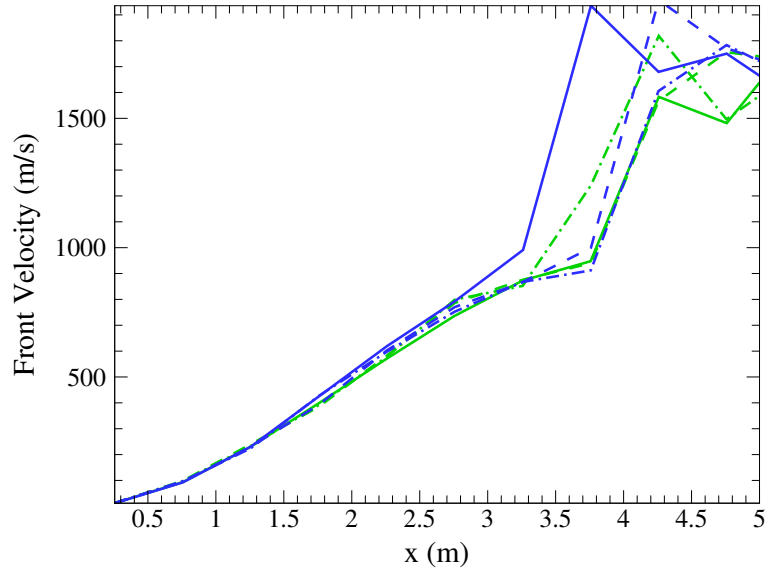


**Figure 3.20.** Flame velocity as a function of position of leading edge of a flame for configuration 17.4,  $\xi = 0.3$  for six nearly identical systems. Green lines represent calculations done with  $dx_{max} = 0.145$  cm. Blue lines represent calculations done with  $dx_{max} = 0.07256$  cm. For each color, different lines represent different initial system temperatures: 297.99 K (solid lines), 298.00 K (dashed lines), 298.01 K (dash-dotted lines). Onset of DDT is found to vary stochastically for these numerical and background perturbations.

### 3.3. DDT in Fuel-Lean and Fuel-Rich Mixtures (Task 2)

Above we outlined a systematic approach to developing a chemical-diffusive submodel for stoichiometric methane-air mixtures. Based on the success of this model when it was used in full numerical simulations for predicting flame acceleration and DDT, we proceeded using a similar approach to develop models for both lean and rich methane-air mixtures. The ultimate objective then is to produce some model that could be interpolated when used for gradients of stoichiometry, which is what we normally would see in a naturally developing mixture of gases. Below we describe a reasonably good model for lean mixtures of methane and air and show that this approach does not generalize directly to rich mixtures. Several alternate, more general approaches for the form of a chemical-diffusive model are discussed. The key condition for computing DDT is that the same model must work reasonably well for both flames and detonations. Figure 3.21 shows how several important properties of methane-air mixtures vary with stoichiometry [33, 57, 58, 73].

#### 3.3.1. Fuel-Lean Model

In order to find a model that works well in full-scale simulations, we look for overlap in the sets of model parameters that will give reasonable values for both flames and detonation. Calibration is performed using the same methodology described in Section 3.1.1. The target values for a fuel-lean, 7% methane-air system are given along with those for a stoichiometric mixture in Table 1. Figure 3.22 shows results for key output parameters as a function of the input variables. As before, we select values from intersections of these curves. For this lean case we find both  $\gamma$  and  $q$  are slightly smaller than those obtained for the stoichiometric case as one might expect since the total amount of fuel and, hence, energy that can be released is also smaller. There is considerable uncertainty in the detonation cell size for this mixture, so two curves are shown representing loose bounds on the acceptable size of the computed  $x_d$ . This figure gives a range of values  $A$ ,  $E_a$  that lie along the  $S_l = 23.7$  cm/s curve bounded by the two dashed curves. We choose a value,  $E_a = 57.55RT_0$ , that lies in the middle of this range. The corresponding value of  $A$  and all other calibrated input parameters are given in Table 5.

We next consider the behavior of a flame calculated using the set of parameters in Table 5 for configuration 17.4. Here we only investigate the case for which  $\xi = 0.3$ . The resulting flame velocity is shown as a function of position in the channel in Figure 3.23. Flame acceleration is nominally slower than that observed for the stoichiometric case discussed in Section 3.1.3, consistent with the fact that  $S_l$  is smaller and  $x_l$  is slightly larger for the lean flame than they are for stoichiometric flames. It is worth noting here that the computed  $x_l = 0.067$  cm is still about a factor of three smaller than measured values [33], which could have an impact on the evolution of flame surface and, hence, acceleration. Experimental flame velocity measurements [72] for 6.5% and 8% mixtures are also shown in Figure 3.23. These curves bound the velocity profile of the simulated 7% mixture, suggesting that the model parameters given in Table 5 at least qualitatively predict the right flame acceleration. Figure 3.23 also shows the results of two parametric sensitivity analyses for which  $T_b$  and  $S_l$  were systematically varied. The results are the same as those discussed in Section 3.1.4, namely that small changes in these flame properties have little effect on the overall flame acceleration. Also, no DDT was observed for this mixture. In the experiments, an 8% mixture was found to undergo DDT while a 6.5% mixture did not.

**Table 5. Material, chemical, and reaction-wave parameters for lean (7%) methane-air**

Quantity	Value	Definition
<b>Input</b>		
$P_0$	1 atm	Initial pressure
$T_0$	298 K	Initial temperature
$\rho_0$	$1.1042 \times 10^{-3}$ g/cm <sup>3</sup>	Initial density
$\gamma$	1.18	Adiabatic index
$M_s$	27	Molecular weight
$A$	$3.2 \times 10^{12}$ cm <sup>3</sup> /g/s	Pre-exponential factor
$E_a$	$57.55 RT_0$	Activation energy
$q$	$36.8 RT_0/M$	Chemical energy release
$\nu_0$	$3.6 \times 10^{-6}$ (g/s-cm-K <sup>0.7</sup> )	Transport constants
$\kappa_0 = D_0$	$6.25 \times 10^{-6}$ (g/s-cm-K <sup>0.7</sup> )	Transport constants
<b>Output</b>		
$S_l$	23.7 cm/s	Laminar flame speed
$T_b$	1971 K	Adiabatic flame temperature
$x_l$	0.067 cm	Laminar flame thickness
$D_{CJ}$	1692 m/s	Chapman-Jouguet detonation velocity
$x_d$	1.01 mm	1D half-reaction detonation thickness

### 3.3.2. Fuel-Rich Model

Finding an adequate model of the form we are using for fuel-rich mixtures is much more difficult. The fundamental problem, shown in Figure 3.21, is that for methane-rich mixtures the rate of change of detonation properties (e.g.  $\lambda$  and  $D_{CJ}$ ) as a function of methane concentration is qualitatively different from that of methane-lean mixtures. The detonation velocity and cell size remain larger and smaller, respectively, for higher methane concentrations than do the laminar flame velocity and adiabatic flame temperature. Because of this, curves of constant  $S_l$  and  $x_d$  for this particular mixture do not intersect within a range of realistic values of the activation energy as shown in Figure 3.24. The figure shows curves for two different  $S_l$  that reflect the large variation in measured flame speeds found in the literature and two curves for detonation thickness to reflect the uncertainty in actual detonation cell size and the correlation factor of the cell size to  $x_d$ . Still, there is no intersection. Here, we use two different approaches to address this difficulty.

In the first approach, we strike a compromise that attempts to match flame parameters more closely than detonation properties. The justification for this is that flame acceleration and onset of DDT depend more strongly on the properties of the flame than on the properties of a detonation wave. These are given in the first column of Table 6. The resulting adiabatic flame temperature and laminar flame speed lie just outside the ranges given in Table 1, while the detonation velocity and the detonation cells are noticeably smaller than the ranges given in Table 1. The laminar flame thickness obtained using these parameters ( $x_l = 0.0631$  cm), while larger than that obtained for a stoichiometric mixture, is significantly smaller than that measured in experiments [33].

In the second approach, we attempt to bring the bounds of the flame speed curves within the bounds of the detonation thickness curves by choosing a smaller value of  $A$  for each particular  $E_a$  and then varying the thermal conductivity, a parameter we had assumed to be fixed and equal to that of air in our stoichiometric and lean models, to speed up and artificially thicken the laminar flame. This procedure has no effect on the detonation wave since thermal conduction does not play a significant role in that combustion mode. Figure 3.25 shows four different curves in the  $\kappa_o$ - $E_a$  parameter space. These curves represent the values of  $\kappa_o$  needed to achieve either  $S_l = 15.7$  cm/s or 23.7 cm/s for the values of  $A$  shown in Figure 3.24 that define the bounds  $x_d = 0.69$  cm and 1.1 cm. Hence, the top and bottom curves in the figure define the bounds on the values of  $\kappa_o$  that can be used to obtain  $S_l$  and  $x_d$  within the ranges shown in Table 1. We are thus, again, in the situation where the choice of parameters is non-unique. The additional dimension in the parameter space, now occupied by  $\kappa$ , allows us to vary the laminar flame thickness independently of the flame speed in an attempt to create a flame that is more physically realistic. For fixed  $A$ ,  $E_a$ , decreasing  $\kappa_o$  results in a reduction of flame thickness, meaning the bottom curve in Figure 3.25 represents the minimum flame thickness achievable for this parameter set. Figure 3.26 shows how  $x_l$  varies along this curve as a function of  $E_a$ . The flame thickness decreases with increasing activation energy, but not quickly enough to fall close to the experimental value of approximately  $x_l = 0.25$  cm. The laminar flames computed using this approach are approximately 2-3 times too thick within the range of reasonable activation energies for this mixture. The choice of  $E_a$ , is then somewhat arbitrary, so we set  $E_a = 67.55RT_0$ , the same value used for the stoichiometric mixture, and choose  $\kappa_o = 4.71 \times 10^{-5}$  g/s-cm-K<sup>0.7</sup> and  $A = 1.053 \times 10^{12}$  cm<sup>3</sup>/g/s, which gives the computed  $S_l = 15.7$  cm/s and  $x_d = 0.69$  cm. These parameters and the corresponding computed flame and detonation properties are given in the second column of Table 6.

We then use both models for 13% methane-air combustion to compute flame acceleration in configuration 17.4 with  $\xi = 0.3$ . The resulting flame velocities are compared with velocities measured in experiments with 12% and 13% methane concentrations [72] in Figure 3.27. We find a significant difference in the flame acceleration between the two cases. This observation is in spite of the fact that both models produce similar  $S_l$  and  $T_b$ . The principle difference between the two cases is the thickness of the computed flames. The model 2 flame is 10 times thicker than the model 1 flame. The result is a much more slowly accelerating turbulent flame brush. The velocities computed for the model 2 flame do, however, agree reasonably well with the experimental measurements. Neither model predicts DDT, nor was it observed in experiments either for this rich case.

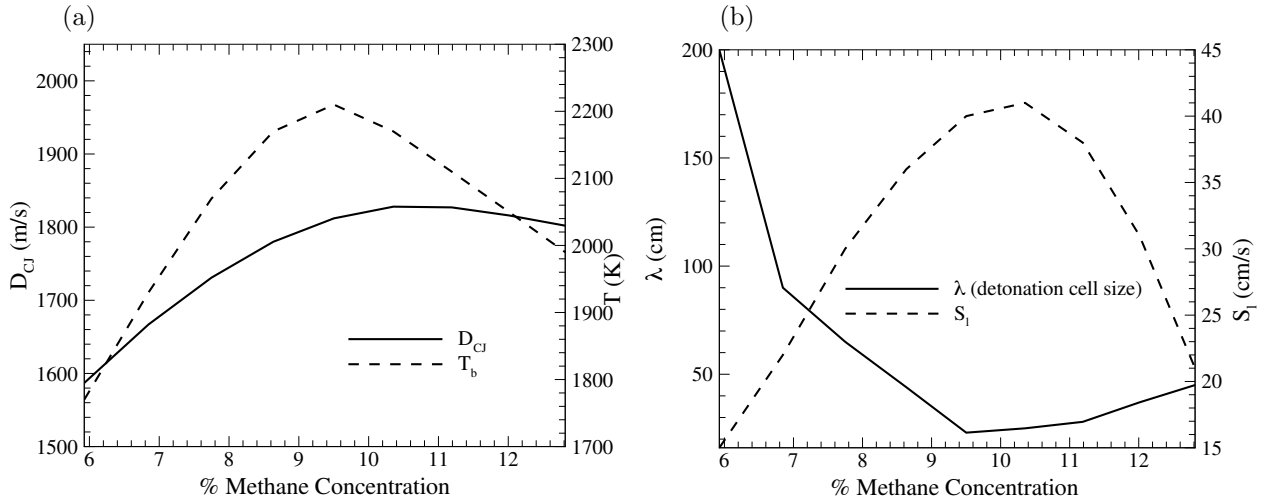
### 3.3.3. Discussion and Other Approaches Under Consideration

Figure 3.27 shows that there is some sensitivity in flame acceleration to the thickness of the modeled flame. This is in contrast to the lack of any pronounced sensitivity to other flame parameters, such as  $S_l$  and  $T_b$ . Further testing is needed to isolate this effect by considering a series of flames with the same  $S_l$  and  $T_b$  but different  $x_l$ , controlled by varying  $\kappa$ . Physically, there may be some justification for rich mixtures having larger  $\kappa$ . The thermal diffusivity of methane is slightly larger than that of air, so the additional methane present in rich mixtures and product gases leads to larger effective diffusivities. The calibrated  $\kappa$  for model 2 is still much larger than one would expect, however.

**Table 6. Material, chemical, and reaction-wave parameters for rich (13%) methane-air**

Quantity	Value	Value	Definition
<b>Input</b>			
$P_0$	1 atm	1 atm	Initial pressure
$T_0$	298 K	298 K	Initial temperature
$\rho_0$	$1.1042 \times 10^{-3} \text{ g/cm}^3$	$1.1042 \times 10^{-3} \text{ g/cm}^3$	Initial density
$\gamma$	1.19	1.27	Adiabatic index
$M_s$	27	27	Molecular weight
$A$	$2.6 \times 10^{12} \text{ cm}^3/\text{g/s}$	$1.053 \times 10^{12} \text{ cm}^3/\text{g/s}$	Pre-exponential factor
$E_a$	$57.55 RT_0$	$67.55 RT_0$	Activation energy
$q$	$36.3 RT_0/M$	$26.71 RT_0/M$	Chemical energy release
$\nu_0$	$3.6 \times 10^{-6} \text{ (g/s-cm-K}^{0.7}\text{)}$	$3.6 \times 10^{-6} \text{ (g/s-cm-K}^{0.7}\text{)}$	Transport constants
$\kappa_0 = D_0$	$6.25 \times 10^{-6} \text{ (g/s-cm-K}^{0.7}\text{)}$	$4.71 \times 10^{-5} \text{ (g/s-cm-K}^{0.7}\text{)}$	Transport constants
<b>Output</b>			
$S_l$	24.1 cm/s	15.7 cm/s	Laminar flame speed
$T_b$	2025 K	1990 K	Adiabatic flame temperature
$x_l$	0.0631 cm	0.698 cm	Laminar flame thickness
$D_{CJ}$	1728 m/s	1800 m/s	C-J detonation velocity
$x_d$	0.54 cm	0.69 cm	1D half-reaction detonation thickness

The single component reaction model, in which fuel is converted completely into product in a single reaction step, is not correct for rich mixtures in which there is fuel left over after oxidation is complete, i.e., when the oxidizer is depleted. For this situation, the oxidizer is the limiting component and should be explicitly computed. Such a two-component reaction model and its effect on flame acceleration and DDT will be discussed in more detail in the following section.



**Figure 3.21.** (a)  $D_{CJ}$  and  $T_b$  computed using chemical equilibrium software [73, 33] and (b)  $\lambda$  and  $S_l$  measured experimentally [14,72] as a function of methane concentration for laminar flames and detonations.

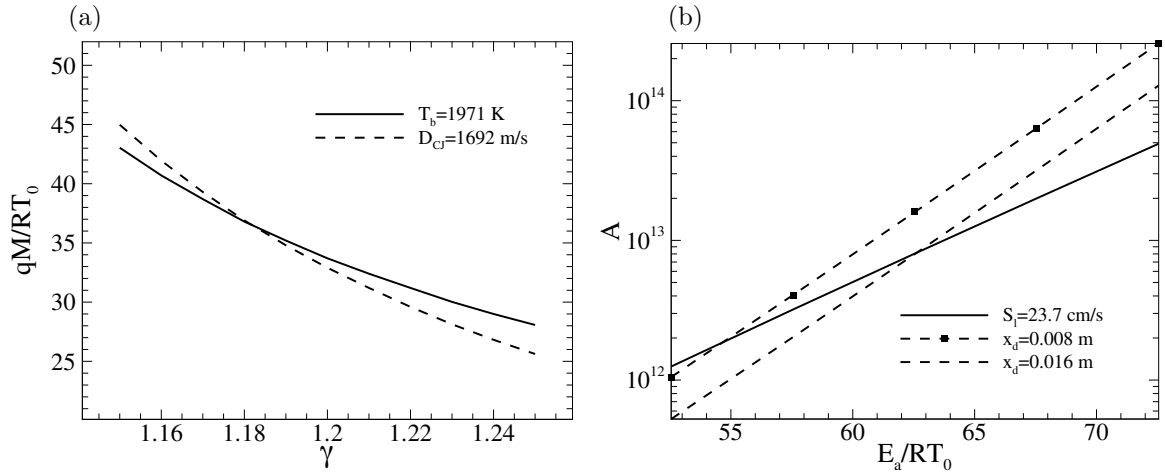


**Figure 3.22.** Parametric curves for which (a)  $T_b = 1971$  K,  $D_{CJ} = 1692$  m/s and (b)  $S_l = 23.7$  cm/s,  $x_d = 0.8$ , and 1.6 cm for a lean (7%) methane-air mixture computed using the single-component reaction model (Eq. (33)). The point of intersection in (a) gives the values of  $qM/RT_0$  and  $\gamma$  used to compute the curves in (b). Two curves for  $x_d$  are given to indicate uncertainty in correlation between detonation cell size and  $x_d$ .

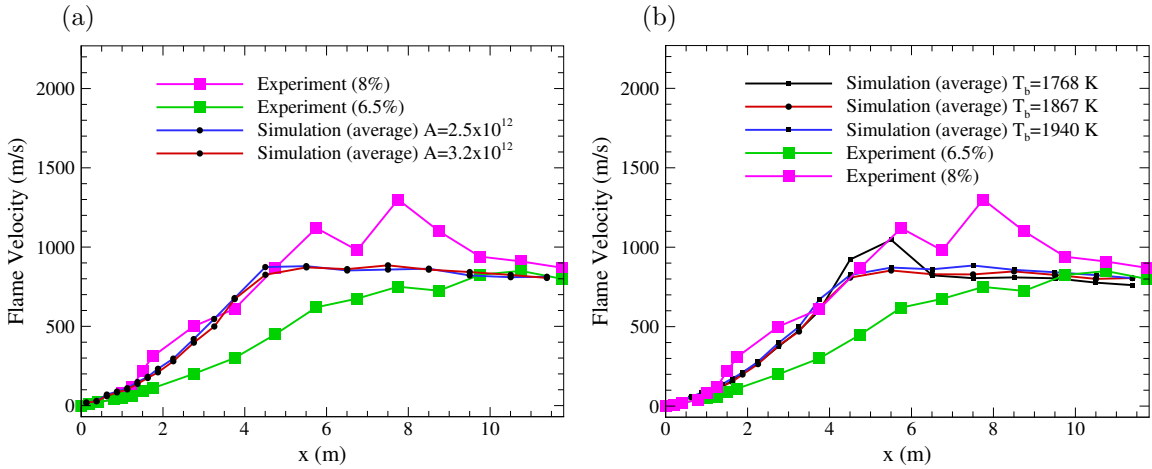


**Figure 3.23.** Velocity of the leading edge of the calculated 7% methane-air flame ( $\Phi\phi = 0.72$ ) as a function of its location in the channel in Configuration 17.4,  $\xi = 0.3$  for (a) various values of  $S_l$  and fixed  $T_b$  and (b) various values of  $T_b$  and fixed  $S_l$  along with experimental measurements for 6.5% and 8% methane-air flames in a similar configuration [72].

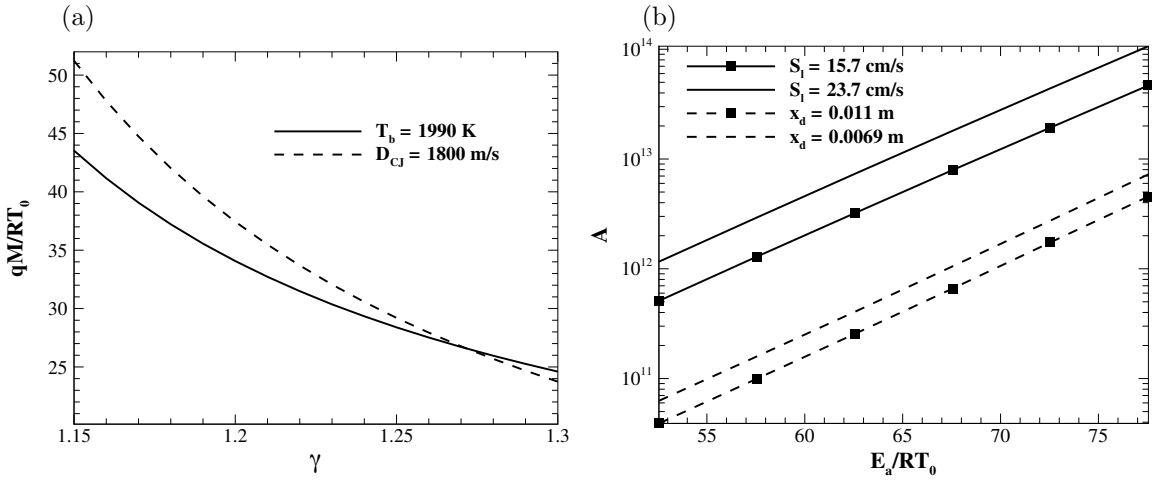


**Figure 3.24.** Parametric curves for which (a)  $T_b = 1990$  K,  $D_{CJ} = 1800$  m/s and (b)  $S_l = 23.7$  and 15.7 cm/s,  $x_d = 0.69$  and 1.1 cm for a rich (13%) methane-air mixture computed using the single-component reaction model (Eq. (33)). The point of intersection in (a) gives the values of  $qM/RT_0$  and  $\gamma$  used to compute the curves in (b). Two curves for  $x_d$  are given to indicate uncertainty in correlation between detonation cell size and  $x_d$ .

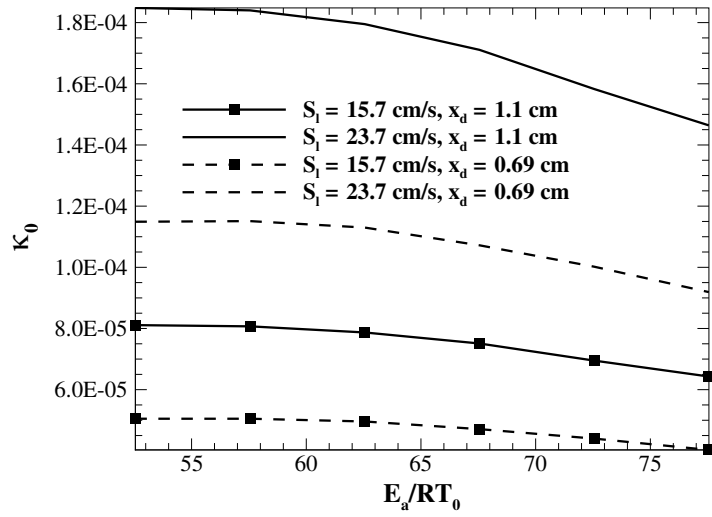


**Figure 3.25.** Variation of  $\kappa_o$  needed to attain  $S_l = 15.7$  or  $23.7$  cm/s using the values of  $A$  for which  $x_d = 0.69$  or  $1.1$  cm shown in Figure 3.23b as a function of  $E_a/RT_0$ .

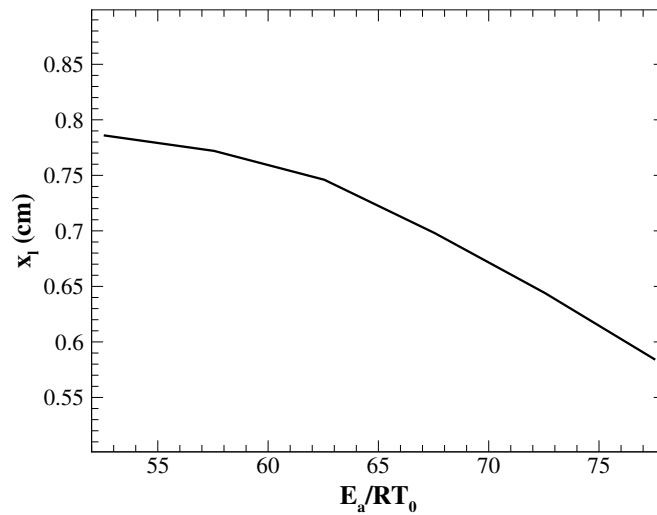


**Figure 3.26.** Laminar flame thickness computed using values of  $\kappa_o$  on the lowest curve in Figure 3.24 ( $S_l = 15.7$  cm/s,  $x_d = 0.69$  cm) as a function of  $E_a/RT_0$ .

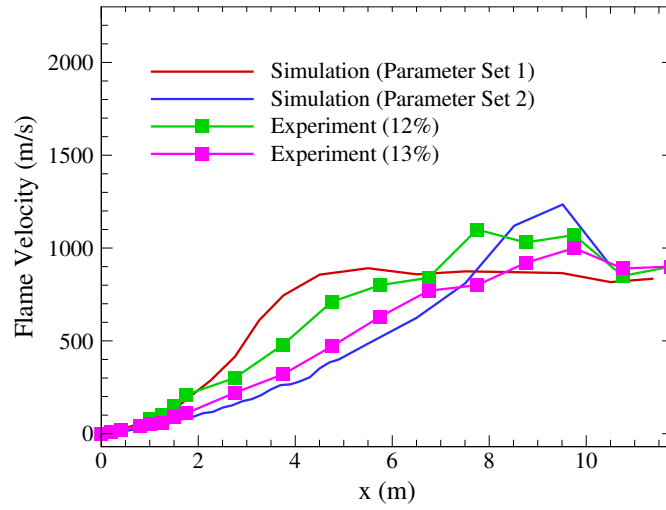


**Figure 3.27.** Velocity of the leading edge of the calculated 13% ( $\phi = 1.43$ ) methane-air flame as a function of its location in the channel in Configuration 17.4,  $\xi = 0.3$  computed using the two parameter sets given in Table 6 along with experimental measurements for 12% and 13% methane-air mixtures in a similar configuration [72].

### 3.4. Propagation in a Gradient of Fuel Composition (Task 3)

While DDT and detonation propagation in uniform fuel-air mixtures has been studied extensively, much less is known about the behavior of deflagration waves, DDT, and detonations in systems where the fuel and air are only partially premixed, that is, where the local fuel concentration is not uniform. Such heterogeneous methane-air systems may form in the unventilated, sealed areas of underground coal mines. If methane gas seeps in from the tunnel roof, then a gradient will exist from roof to floor while the methane diffuses into the air. The magnitude of this gradient will depend on the methane influx rate from the tunnel roof. If air leaks through seals into a methane-rich sealed area, then buoyancy will cause the inflowing air to collect near the tunnel floor and the existing methane-rich atmosphere to collect near the tunnel roof until diffusion leads to their complete mixing. In this case, the magnitude of the composition gradient will depend on the air inflow rate into the sealed area. Understanding how a flame accelerates, whether it can undergo transition to a detonation, and how that detonation propagates are important general problems anywhere natural gas accumulates.

In premixed systems, the propagation speed and the cellular structures formed by instability of a detonation front depend strongly on the equivalence ratio of the fuel-air mixture. The general trend is for the detonation to slow and cell sizes to grow as the mixture moves away from stoichiometric. In methane-air systems, the detonation cell width was found to vary between 21 and 51 cm over a methane concentration range of only 3.5% [72]. These observations suggest that in partially-premixed systems where the concentration of fuel is nonuniform, both the propagation speed and the detonation cell size can vary as a function of space. The implications of this spatial dependence have been studied in systems where the gradient of the fuel concentration is parallel to the direction of propagation [86–88]. The magnitude of the concentration gradient was found to be a determining factor in whether or not a detonation could propagate through the nonuniform mixture.

Less work has been done on systems for which the gradient in fuel concentration is normal to the direction of propagation of the detonation. Experiments have shown that the sizes of detonation cells vary spatially in relation to the variation in fuel concentration [89] and that the shape of the detonation wave is curved in these systems [89, 90]. Calhoon and Sinha [91] calculated the structure of a detonation in the mixing layer of laminar, initially non-premixed, co-flowing streams of fuel and air. They found a complex wave structure that resembled a typical triple flame found in low-speed mixing layers [92, 93]. A detonation formed near the line of stoichiometry in the mixing layer that extended into the fuel-rich and fuel-lean mixtures above and below this point. In these regions, the detonation was curved due to variations in the local propagation speed. Far from the line of stoichiometry where the mixture was either too rich or too lean to support a detonation, the leading shock detached from the reaction zone leaving behind high-speed deflagrations. Downstream, a diffusion flame consumed the excess fuel and oxidizer that were not burned in the fuel-rich and fuel-lean detonations and deflagrations.

Here we generalize this to a partially premixed system (similar to that used by Calhoon and Sinha [91]) in which the local methane-air equivalence ratio varies as a function of space and time. Ultimately, we wish to consider flame acceleration and DDT in configurations similar to those considered in Sections 3.1–3.3. This work, however, is still ongoing, and in the following sections we give only an overview of the calibration of the numerical and physical models being used. We then test these models by performing calculations of

a detonation propagating in a heterogeneous methane-air mixture. These preliminary results are discussed in context of the previous experimental and numerical studies described above. Eventually, we plan to use the same models to compute flame acceleration and transition to detonations in obstructed channels.

### 3.4.1 The Two-Component Model

Since now the relative concentrations of fuel and oxidizer can vary throughout the system, we must consider a two-component, single-step reaction model,  $\nu_F F + \nu_O O \rightarrow (\nu_P) P$ , in which  $\nu_F$  moles of fuel ( $F$ ) combine with  $\nu_O$  moles of oxidizer ( $O$ ) to form  $\nu_P$  moles of product ( $P$ ). The molecular weights of the fuel and oxidizer species are given by  $W_F$  and  $W_O$ , respectively. In order to compute partially premixed flames and detonations, it is necessary to consider the dynamics of both the fuel and oxidizer species, the mass fractions of which ( $Y$  and  $X$ , respectively) are governed by

$$\frac{\partial(\rho Y)}{\partial t} + \nabla \cdot (\rho Y \mathbf{v}) - \nabla \cdot (\rho D_f \nabla Y) - \rho \dot{\Omega} = 0, \quad (3.11)$$

$$\frac{\partial(\rho X)}{\partial t} + \nabla \cdot (\rho X \mathbf{v}) - \nabla \cdot (\rho D_o \nabla X) - \rho S \dot{\Omega} = 0. \quad (3.12)$$

These equations are solved concurrently with Eqs. (2.1–2.5). Here, we assume a two-component reaction model for which we write the fuel consumption rate,

$$\dot{\Omega} = -\rho A(\phi) Y X \exp(-E_a(\phi)/RT), \quad (3.13)$$

that explicitly depends on the local concentrations of both fuel and oxidizer. The pre-exponential factor  $A$  and the activation energy  $E_a$  are assumed to vary with the local equivalence ratio  $\phi$ . In order to ensure the model gives the correct flame temperature and flame speed as a function of equivalence ratio, we also allow  $q$  and  $\kappa_o$  to vary as functions of  $\phi$ . For a two-component mixture, we define a local mixture fraction  $Z$  that does not vary across the reaction zone [94, 95],

$$Z = \frac{SY - X - SY_{lean} + 1}{1 + S - X_{rich} - SY_{lean}}, \quad (3.14)$$

where  $S = s\tilde{Y}_\infty/\tilde{X}_\infty$  is the global equivalence ratio,  $s = \nu_o W_o/\nu_f W_f$  is the stoichiometric coefficient of the reaction,  $Y_{lean}$  is the mass fraction of fuel in the leanest region of the flow (where  $\tilde{X} = \tilde{X}_\infty$ ), and  $X_{rich}$  is the oxidizer mass fraction in the richest region of the flow (where  $\tilde{Y} = \tilde{Y}_\infty$ ). Since  $Z$  is a conserved quantity across the flame front, it can be related to the fuel and oxidizer mass fractions in the unburned mixture just upstream of the reaction zone according to

$$Y_{unb} = Z(1 - Y_{lean}) + Y_{lean}, \quad X_{unb} = (1 - Z)(1 - X_{rich}) + X_{rich}. \quad (3.15)$$

The local equivalence ratio can then be computed based on these unburned mass fractions,

$$\phi = \frac{SY_{unb}}{X_{unb}}. \quad (3.16)$$

We define  $\tilde{X}_\infty$  and  $\tilde{Y}_\infty$  as the maximum possible oxidizer and fuel mass fractions in the domain, respectively. In the equations above, the fuel and oxidizer mass fractions,  $Y$  and  $X$ , have been normalized by these values so that they vary between 0 and 1.

3.4.1a. Calibration for Stoichiometric Mixture

**Table 7. Input model parameters and computed properties of reaction waves for five different methane-air mixtures using a two-component reaction model.**

Quantity	5.9% ( $\phi = 0.6$ )	7% ( $\phi = 0.72$ )	9.5% ( $\phi = 1$ )	11.2% ( $\phi = 1.2$ )	13% ( $\phi = 1.43$ )
<b>Input</b>					
$P_0$ (atm)	1	1	1	1	1
$T_0$ (K)	298	298	298	298	298
$\rho_0$ (g/cm <sup>3</sup> )	$1.1042 \times 10^{-3}$	$1.1042 \times 10^{-3}$	$1.1042 \times 10^{-3}$	$1.1042 \times 10^{-3}$	$1.1042 \times 10^{-3}$
$\gamma$	1.172	1.18	1.197	1.244	1.27
$M_s$ (g/mol)	27	27	27	27	27
$A$ (cm <sup>3</sup> /g-s)	$1.0697 \times 10^{11}$	$7.0 \times 10^{11}$	$1.78 \times 10^{13}$	$7.583 \times 10^{14}$	$9.343 \times 10^{12}$
$E_a/RT_0$	42.0	52.55	67.55	95	77.55
$qM/RT_0$	33.66	36.81	39.0	37.2	38.29
$\nu_0$ (g/s-cm-K <sup>0.7</sup> )	$3.6 \times 10^{-6}$	$3.6 \times 10^{-6}$	$3.6 \times 10^{-6}$	$3.6 \times 10^{-6}$	$3.6 \times 10^{-6}$
$\kappa_0 = D_{f0} = D_{o0}$ (g/s-cm-K <sup>0.7</sup> )	$1.53 \times 10^{-5}$	$2.1 \times 10^{-5}$	$3.25 \times 10^{-5}$	$5.92 \times 10^{-5}$	$5.25 \times 10^{-5}$
<b>Output</b>					
$S_l$ (cm/s)	15.4	21.6	40.3	38.0	15.9
$T_b$ (K)	1770	1971	2210	2110	1990
$x_l$ (cm)	0.24	0.24	0.21	0.37	0.76
$D_{CJ}$ (m/s)	1587	1691	1820	1827	1800
$x_d$ (cm)	2.02	1.32	0.23	0.29	0.39

Calibration of the model parameters is performed in a manner similar to that described in Sections 3.1.1 and 3.3.2. Target laminar flame properties (flame speed, adiabatic flame temperature, laminar flame thickness) and detonation properties (Chapman-Jouget velocity, 1D detonation thickness) are given in Table 1 for several different methane-air mixtures. We solve the steady-state laminar flame equations (Eqs. (3.5), (3.6)) and the one-dimensional ZND equations for a propagating detonation wave (Eqs. (3.7)–(3.10)) using the two-component reaction model (Eq. 3.13) to obtain a set of parameters for which  $T_b$ ,  $S_l$ ,  $x_l$ ,  $D_{CJ}$ , and  $x_d$  fall within these target ranges for each of the three compositions. Since  $T_b$  and  $D_{CJ}$  do not depend on the reaction model, the values for  $\gamma$  and  $q$  are chosen as the same points of intersections of the curves shown in Figures 3.1a, 3.22a, and 3.24a. These values are listed in Table 7. For this two-component reaction model, the actual magnitude of the non-dimensional heat release  $q^*$  is scaled by  $\tilde{Y}_\infty$  so that  $q = q^* \tilde{Y}_\infty$  and the magnitude of the actual pre-exponential factor  $A^*$  is scaled by  $\tilde{X}_\infty$  so that  $A = A^* \tilde{X}_\infty$ .

Next, we next calibrate  $A$  and  $E_a$  for each composition based on the  $S_l$  and  $x_d$  given in the table. The use of the two-component reaction model causes only small differences in the computed detonation structure from that computed using the single-component model. The choice of reaction model, however, significantly affects the speed and thickness of a laminar flame. Values of  $A$  and  $E_a$  that give  $S_l$  and  $x_d$  in the target range for a stoichiometric mixture are plotted in Figure 3.28. These curves do not intersect

within the reasonable range of  $E_a$ . We can alter the flame speed for fixed  $A$ ,  $E_a$  by changing the thermal conductivity of the mixture. The approach we take here is to choose a point in the  $A$ - $E_a$  parameter space that gives  $x_d$  within the target range shown in Table 1. In principle, we could choose any such  $A$ ,  $E_a$  pair, but to make direct comparisons with results obtained using the single-component reaction model we choose the same  $E_a/RT_o = 67.55$  and select  $A = 1.78 \times 10^{13}$  cm<sup>3</sup>/g-s such that the computed  $x_d = 0.229$  cm. This detonation thickness is identical to that obtained using the single-component reaction model as shown in Figure 3.29. Given this set of parameters,  $q$ ,  $\gamma$ ,  $A$ ,  $E_a$ , we then increase  $\kappa_o$  to give  $S_l$  in the target range. The resulting  $\kappa_o = 3.25 \times 10^{-5}$  g/s-cm-K<sup>0.7</sup> is much larger than the actual conductivity of the methane-air mixture, but when used along with the rest of the parameter set, it gives the correct laminar flame speed and a laminar flame thickness that is comparable to experimental measurements. Comparisons between two-component model flame structures and the single-component model flame structure are made in Figure 3.30. The flames represented by the blue and black lines both propagate at the same speed, but are quite different in terms of thickness.

We next compare flame acceleration computed using single-component and two-component reaction models. Two-dimensional simulations of configuration 17.4 (cf. Section 3.1) are performed for a blockage ratio  $\xi = 0.3$ . Grid sizes are chosen so that both the smallest  $dx_{min}$  and largest  $dx_{max}$  are equal to those shown in Section 3.2 to produce converged results, i.e.,  $dx_{min} = 0.009062$  cm and  $dx_{max} = 0.145$  cm. Flame velocities as a function of position in the channel are shown for three different cases in Figure 3.31. The single-component case with parameters shown in Table 2 is given by the red line. The laminar flame speeds are identical for the two cases shown for the two-component model (green and blue lines), but the case with larger  $\kappa_o$  and smaller  $A$  (blue line) gives a much larger flame thickness (see Figure 3.30.) This leads to a restriction in the rate of growth of total flame surface area due to wrinkling, and hence a slower energy output and flame acceleration. This curve seems to more closely match the experimental data shown in the figure (light blue, purple) than either curve generated with smaller  $\kappa_o$ .

### 3.4.1b. Calibration for Non-Stoichiometric Mixtures

The calibration of non-stoichiometric values of  $\phi$  can be done in a variety of ways. Here, we discuss three different approaches. First, we assume that the transport and reaction parameters are constant over the entire range of  $\phi$ . Second, we perform the same calibration procedure used above to compute the parameters for a stoichiometric mixture to find sets of parameters for two additional equivalence ratios and then use a second-order polynomial to interpolate the results to other values of  $\phi$ . Third, we calibrate sets of parameters for four additional equivalence ratios (for a total number of calibration mixtures of five) and use fourth-order polynomials to construct the variation of the reaction parameters with  $\phi$  for all intermediate values. Each of these approaches will be discussed in more detail below.

The most straightforward approach is to use constant values of the reaction parameters  $q^*$ ,  $A^*$ ,  $\gamma$ ,  $E_a$ , and  $\kappa_o$ . The terms  $q = q^* \tilde{Y}_\infty$  and  $A = A^* \tilde{X}_\infty$  that appear in Eqs. (3.11), (3.12), and (2.3) naturally vary with  $\phi$  and thus allow for the detonation parameters to change with the mixture composition. The values of these parameters calibrated for a stoichiometric mixture are used for a range of  $\phi$  from 0.6–1.4, and Figures 3.33a and b show the resulting variations of  $D_{CJ}$  and  $x_d$  computed using this approach. These results are compared with accepted values of  $D_{CJ}$  obtained using a chemical equilibrium code [73] and of  $x_d$

based on the correlation [59] between reaction zone width and measured detonation cell sizes [14, 72] used above. The computed values of  $D_{CJ}$  and  $x_d$  deviate substantially from the accepted values for  $\phi \neq 1$ .

In the second approach, we attempt to improve the predictive capability of the reaction model for lean and rich mixtures by allowing the reaction parameters to vary with  $\phi$ . Two additional values of  $\phi$  are chosen for calibration, one lean ( $\phi = 0.72$ , 7% methane) and one rich ( $\phi = 1.43$ , 13% methane), with target detonation and flame properties given in Table 1. The procedure used to find  $A$ ,  $E_a$ ,  $q$ ,  $\gamma$ , and  $\kappa_0$  for these two equivalence ratios is the same as that used to calibrate the stoichiometric mixture. These parameters are also summarized in Table 7. In performing these calibrations, we adjusted the parameters so that the computed values of  $x_l$  varied with equivalence ratio in a manner similar to that observed in experiments. The value computed for  $\phi = 1$  is somewhat larger than the target value shown in Table 1. Values of  $E_a$ ,  $\kappa_0$ , and  $A$  for the 7% and 13% calibration mixtures were adjusted to ensure both the lean and rich flames were thicker than the stoichiometric flame, in accordance with experimental measurements. The parameter sets computed and given in Table 7 do not constitute a definitive reaction model for the respective mixtures since there is some uncertainty in the experimental measurements used to calibrate them. Hence, a variety of possible model parameter sets exist that could adequately reproduce the data given in Table 1.

We then fit a second order polynomial to the calibrated values of  $A$ ,  $E_a$ ,  $q$ ,  $\kappa_0$ , and  $\gamma$  to give a continuous set of values for these parameters as a function of  $\phi$ ,

$$A = A_{ST} \exp[-18.388\phi^2 + 43.185\phi - 24.796], \quad (3.17)$$

$$E_a = E_{a,ST}(-0.6321\phi^2 + 1.8803\phi - 0.2482), \quad (3.18)$$

$$q = q_{ST}(-0.3427\phi^2 + 0.7905\phi + 0.5522), \quad (3.19)$$

$$\gamma = \gamma_{ST}(0.1283\phi^2 - 0.17\phi + 1.0417), \quad (3.20)$$

$$\kappa_o = \kappa_{o,ST}(1.3707\phi - 0.352), \quad (3.21)$$

where the subscript  $_{ST}$  indicates the parameter's value in the model stoichiometric mixture given in Table 7.

This particular choice of fitting curve is empirical and was made to most closely match the data for  $D_{CJ}$  and  $x_d$ . The transformation of  $A$  to logarithmic coordinates was done to ensure that  $A$  cannot become negative for any value of  $\phi$ . Values of  $A$ ,  $E_a$ ,  $q$ ,  $\kappa_0$ , and  $\gamma$  calculated using Eqs. (3.17–3.21) are shown in Figures 3.32a–e for a range of  $\phi$ , and the values of  $D_{CJ}$  and  $x_d$  computed using these parameters are shown in Figures 3.33a and b. This second order approach does a better job at describing both  $D_{CJ}$  and  $x_d$  for lean values of  $\phi$ , but it introduces a non-physical local minimum of  $D_{CJ}$  for rich mixtures. Additionally, the maximum  $D_{CJ}$  occurs for  $\phi = 1$  in contrast to the exact  $D_{CJ}$ , which peaks between  $\phi = 1.1$  and 1.2.

The third approach addresses this shortcoming by adding more control points, i.e, calibrated parameter sets for more mixture compositions, and seeking a higher-order polynomial fit for the reaction parameters. Two additional values of  $\phi$  are considered:  $\phi = 0.6$  and  $\phi = 1.2$ . The same calibration process used to obtain the transport and reaction coefficients for  $\phi = 0.72$ , 1, and 1.43 is used to calibrate  $\phi = 0.6$ , and  $\phi = 1.2$ . We found it impossible to obtain a set of parameters with realistic values of activation energy that produces  $x_d$ ,  $S_l$ , and  $x_l$  that are all close to the accepted values. Instead, we adjusted  $A$ ,  $E_a$ , and  $\kappa_o$  to match  $x_d$  and  $S_l$  and maintain the correct qualitative behavior of  $x_l$  in relation to the values obtained for the other control points. The transport and reaction coefficients obtained for  $\phi = 0.6$  and 1.2 are shown in Table 7.

We then fit fourth-order polynomials to all five of the control points for the various reaction parameters, resulting in the following set of equations:

$$A = A_{ST} \exp [-225.6201\phi^4 + 836.2564\phi^3 - 1131.2621\phi^2 + 674.6915\phi - 154.0657], \quad (3.22)$$

$$E_a = E_{a,ST}(-24.565\phi^4 + 92.888\phi^3 - 127.59\phi^2 + 76.484\phi - 16.216), \quad (3.23)$$

$$q = q_{ST}(2.3585\phi^4 - 7.8387\phi^3 + 8.4459\phi^2 - 2.9394\phi + 0.9737), \quad (3.24)$$

$$\gamma = \gamma_{ST}(-1.5509\phi^4 + 5.9854\phi^3 - 8.2683\phi^2 + 4.9247\phi - 0.091), \quad (3.25)$$

$$\kappa_o = \kappa_{o,ST}(-42.707\phi^4 + 161.04\phi^3 - 219.07\phi^2 + 129.13\phi - 27.391), \quad (3.26)$$

which are plotted along with the second-order fits in Figures 3.32a–e. The additional control points add local maxima and minima to the curves for the individual reaction parameters, which have no reasonable physical description. They appear as a result of trying to force a single reaction model to describe two disparate burning regimes: low-speed flames and high-speed detonations. Taken collectively and used in conjunction with Eq. (3.13), these parameters produce  $D_{CJ}$  and  $x_d$  shown in Figures 3.33a and b that exhibit the desired features of the exact  $D_{CJ}$  and  $x_d$ . Similarly good agreement is obtained for  $T_b$  and  $S_l$  (not shown), and the variation in  $x_l$  is qualitatively correct although each individual value is larger than the exact value. We caution, however, that Eqs. (3.22–3.26) should not be used outside of the range of  $\phi = 0.6$ – $1.43$  without further calibration.

### 3.4.2. Detonations in Uniform, High-Activation-Energy Mixtures

The ultimate goal of this work is to use the model developed in Section 3.4.1 to compute turbulent flame acceleration, shock-flame interaction, DDT, and detonation propagation in partially-premixed systems in which a bulk gradient in the local fuel concentration exists. This work is ongoing, and here we only present preliminary results concerning the propagation of a detonation through such a concentration gradient.

Consider a nonuniform mixture of methane and air in a 32 cm-wide by 1024 cm-long channel as shown in Figure 3.34. The mixture at the top of the channel ( $y = 32$  cm) is taken to be fuel rich,  $\phi_r$ , and that at the bottom of the channel ( $y = 0$  cm) is taken to be fuel lean,  $\phi_l$ . The initial concentration gradient is set by assuming a linear variation in  $\phi$  from  $\phi_l$  to  $\phi_r$ . The mixture is ignited directly by a strong shock with Mach number,  $M_s$ , equal to 10. The shock is placed initially 2 cm to the right of the closed end of the channel. The temperature of the compressed gas in the region behind the shock is sufficiently high to allow a detonation to ignite in a short period of time, which then propagates from left to right through the domain.

We consider first the propagation of detonation waves through several different uniform methane-air mixtures, ranging in equivalence ratio from  $\phi = 0.7$  to  $\phi = 1.1$ . For all cases, we set  $\phi_l = \phi_r$  so that there is no concentration gradient within the mixtures. The detonation propagation velocities in each mixture are shown in Figure 3.35 as a function of the  $x$ -location of the leading edge of the reaction zone in the channel. The thinner horizontal lines indicate the value of  $D_{CJ}$  for each mixture. After an initial adjustment period, equal to about 15 channel widths, the propagation velocity decays to a level consistent with  $D_{CJ}$ . There is little difference between the propagation velocities for the  $\phi = 1$  and  $1.1$  cases shown in the figure, consistent with the behavior of  $D_{CJ}$  over that range of  $\phi$ , but there is a noticeable drop in velocity for the lean cases.

The leanest case,  $\phi = 0.7$ , cannot support a detonation in this channel, and a steep drop in flame velocity occurs when the the leading shock and flame decouple after propagating together for about 180 cm (or about 6 channel widths). This is not surprising since the detonation cell size for a mixture with  $\phi = 0.7$  is close to 90 cm [14, 72], which is much larger than the size of the channel. The observed detonation failure is not related to any thermal or mechanical losses that are not included in our model. The failure occurs because of the strong instabilities of the detonation front in a system with high activation energy. Both transverse and longitudinal instabilities contribute to the spatial and temporal fluctuations of the detonation velocity. When the front slows down to  $D_{CJ}$ , and only a few triple points remain in the channel, these points can easily weaken as a result of a fluctuation. In a system with high activation energy, the induction delay behind a shock rapidly decreases as the shock weakens. Thus, the reaction in the vicinity of weakened triple points may quench, and the flame can decouple from the leading shock as a result of a fluctuation. In a very long channel without losses, the detonation would eventually reignite, but this may never happen in channels limited to practical lengths.

Figure 3.36a shows a sequence of density plots in the vicinity of the propagating reaction front as the detonation transitions to a shock-flame complex. The red parts are high-density regions containing unreacted material, which was compressed by an inert shock wave that decoupled from the reaction front. Green parts of the front are overdriven detonations. Several transverse instabilities on the detonation front are visible prior to the detonation failure. These triple points are the regions of high pressure that produce the cellular patterns observed in experiments. Numerically, we track the trajectories of these triple points by recording the maximum pressure experienced in each computational cell. An example of such a numerical smoke foil for the uniform  $\phi = 0.7$  detonation is shown in Figure 3.37a. The highest pressures are represented by the black traces in the figure. Near the left side of the smoke foil, as the detonation is just beginning to propagate, small-scale instabilities develop along the initially planar and smooth detonation front. These instabilities, most likely triggered by numerical noise in the integration routine, form cells that grow from small and regular diamonds when the detonation is initially overdriven to large, irregular quadrilaterals as the detonation approaches the CJ velocity. In the vicinity of 180 cm from the closed end of the channel the triple points weaken and disappear as the detonation fails.

A similar process occurs for the  $\phi = 0.8$  case, but the detonation is able to survive and propagate at near-CJ speed for a much longer distance than the detonation in the  $\phi = 0.7$  mixture. Shock-flame decoupling occurs around 320 cm from the closed end wall. Again, triple points all weaken and die out as they propagate along the detonation front (Figure 3.37b). This is also to be expected since the cell size for a detonation in a  $\phi = 0.8$  mixture is approximately 65 cm [14, 72], which is also larger than the height of the channel.

For the  $\phi = 0.9$  and 1.0 cases, the detonations are able to survive and propagate indefinitely through the channel at average speeds roughly equal to the CJ velocities for each mixture. It is difficult to get a precise measurement of the propagation velocity because of the influence of longitudinal and transverse instabilities. For high-activation energy mixtures, the longitudinal propagation velocity has been shown to fluctuate about the CJ velocity, locally weakening and strengthening the detonation. The transverse instabilities that give rise to triple points also cause ambiguity. At some times and locations, the leading edge of the front between two triple points is an overdriven detonation with velocity greater than  $D_{CJ}$ , and

at other times and locations a decoupled shock-flame complex with velocity less than  $D_{CJ}$ . A sequence of density fields taken from the  $\phi = 1.0$  calculations at several instants over a characteristic detonation-cell crossing time are shown in Figure 3.36b. The color mappings have the same interpretation as those given above for the  $\phi = 0.7$  case. While there are intermittent periods of shock-flame decoupling along the reaction front, there is never a global shock-flame decoupling like that shown in Figure 3.36a. Instead, a myriad of transverse instabilities are visible, the size of which vary substantially across the width of the channel. These instabilities leave behind highly irregular cellular patterns in the numerical smoke foil shown in Figure 3.37c. The initial cellular structures are relatively small and regular, but later complex multi-level structures appear that show no clear distinction between large-scale cells caused by the large primary triple points on the reaction front and small-scale cells caused by the smaller secondary triple points that form between the primary instabilities. A close-up view of the cellular structure is shown in Figure 3.38a. This is compared with a portion of an experimental smoke foil of roughly the same dimensions obtained for a near-stoichiometric methane-air mixture [14] (Figure 3.38b). The multilevel cellular structures are also found on the experimental smoke foil, but the cells in the photograph seem to be more complete than those found on the numerical smoke foil. Similar multilevel instabilities have also been computed using a single-component reaction model [10] and seem to be unique to mixtures with very large effective activation energies.

Due to the irregularity of the cells produced by this high-activation energy mixture, there is no noticeable difference between the structures shown in Figure 3.37c for  $\phi = 1$  and those obtained for  $\phi = 0.9$  and  $1.1$ . For the rich ( $\phi = 1.1$ ) mixture,  $D_{CJ}$  and  $\lambda$  do not vary noticeably from those in a stoichiometric mixture.

### 3.4.3. Detonations in a Concentration Gradient

We next consider nonuniform mixtures of methane and air in the same two-dimensional channel configuration. The mixture at the top of the channel ( $y = 32$  cm) is taken to be fuel rich, and that at the bottom of the channel ( $y = 0$  cm) is taken to be fuel lean. Between these two extremes,  $\phi$  varies linearly from  $\phi_r$  to  $\phi_l$ . Three different cases are investigated: (1)  $\phi_l = 0.7$  and  $\phi_r = 1.3$ , (2)  $\phi_l = 0.8$  and  $\phi_r = 1.2$ , and (3)  $\phi_l = 0.9$  and  $\phi_r = 1.1$ . The behavior of the detonation is different for each of the three cases, the reaction wave propagation velocities of which are shown in Figure 3.40. For case 1, the propagation velocity abruptly changes from  $\approx 1700$  m/s to  $\approx 1000$  m/s in a manner similar to that shown in Figure 3.35 for the  $\phi = 0.7$  case. For cases 2 and 3, the detonations are able to survive and propagate at speeds between  $D_{CJ}(\phi_l)$  and  $D_{CJ}(\phi_r)$ . The same basic reaction zone structure is formed for each of the three cases and is shown in Figure 3.39. The leading edge of the reaction zone is an unstable detonation front. Away from the center of the channel, where  $\phi = 1$ , excess fuel and oxidizer pass through the propagating detonation wave. These reactants mix downstream and burn in a turbulent diffusion flame that trails behind the leading detonation. We note here that the burning in this diffusion zone is only qualitative. Since we are neglecting the diffusive terms in the reactive Navier-Stokes equations, burning is caused by numerical diffusion in the integration routine. A large degree of turbulent mixing occurs in this region, which also assists with keeping the trailing diffusion flame active.

We begin by considering case 1, for which the variation in composition  $d\phi = \phi_r - \phi_l = 0.6$ . The results shown in the previous section indicate that a detonation cannot propagate in a mixture with  $\phi = 0.7$  or  $0.8$  for the channel size being used. The numerical smoke foil shown in Figure 3.41a shows how the cellular pattern caused by the propagating detonation wave in the case 1 mixture evolves from detonation initiation to the final decay. Initially, the detonation is overdriven, allowing a multitude of smaller cells to form within the channel. Throughout the first two-thirds of the the smoke foil, there is a noticeable difference in the sizes of the cells formed near the top of the channel, where the mixture is rich, and those formed near the bottom, where the mixture is lean. The size of cells for the lean equivalence ratios encountered in case 1 are known to be substantially larger than those for the rich mixtures encountered in case 1. Hence, the appearance of larger cells near the bottom of the channel is physically consistent with experimental observations in hydrogen-oxygen mixtures [89]. As the detonation slows to a steady propagation speed, the cell sizes grow throughout the channel, and just prior to the detonation failure there is little difference between the sizes of cells near the top of the channel and those near the bottom of the channel. Failure occurs as triple points propagate from the more reactive mixtures at the top of the channel to the less reactive mixtures near the bottom and all die before they can reflect off the bottom wall.

The smoke foil for case 2 ( $\phi_l = 0.8$ ,  $\phi_r = 1.2$ ) shows a system in which the survival of the detonation is tenuous (Figure 3.41b). Although it has managed to propagate for a distance equivalent to 10 channel widths, there is no guarantee that it will continue to propagate indefinitely. For this case strong triple points that originate in the more reactive mixture near the top of the channel propagate into the less reactive mixture near the bottom of the channel. Sometimes these triple points die out, but some can survive and be reflected back into the system. For some portions of the smoke foil, there is a single triple point that propagates between the two channel walls. Here, we have an added level of complexity in that the reactivity of the mixture changes across the channel, and chance fluctuations in the propagation speed of the detonation could be sufficient to cause the triple point to die. This behavior causes drastic distortions of the detonation surface as large regions of reaction zone decouple from the leading shock at any particular instant.

Case 3 ( $\phi_l = 0.9$ ,  $\phi_r = 1.1$ ) is more robust than cases 1 and 2. The mixture throughout the channel is everywhere sufficiently reactive for detonation propagation to occur. Accordingly, there is less fluctuation in the average propagation velocity (Figure 3.40), the magnitude of which seems to be slightly less than the CJ velocity obtained for any of the compositions present within the gradient. The cellular patterns left behind by this propagating detonation, a portion of which is shown in Figure 3.41c, are quite similar to those obtained for the near-stoichiometric uniform mixtures (cf. Figure 3.38a). A hierarchy of cellular structures can be found, the largest of which appear to be incomplete. A sequence of density plots over a distance roughly equal to one channel width is shown in Figure 3.42. The detonation wave appears to behave in a manner similar to that observed for a uniform stoichiometric mixture.

#### 3.4.4. Conclusions and Future Directions

A single-step, two-component reaction model for nonuniform methane-air mixtures was developed. Reaction and transport coefficients were calibrated to reproduce properties of detonations and laminar flames over a range of unburned mixture compositions. Chapman-Jouget detonation velocities and reaction zone widths were found to match closely exact values within this limited range of  $\phi$ . This model was used to compute

the propagation of detonation waves in a two-dimensional channel filled with various uniform methane-air mixtures and several mixtures in which the fuel concentration varied across the channel width.

The two leanest uniform mixtures that were considered ( $\phi = 0.7$  and  $0.8$ ) did not support detonation propagation. After relaxing to near-CJ velocities, instabilities in the detonation front caused the reaction zone to globally decouple from the leading shock wave. Mixtures closer to stoichiometric ( $\phi = 0.9, 1,$  and  $1.1$ ) were able to support a detonation in the 32 cm channel. Propagation velocities for these three cases were similar and, on average, were very close to their respective CJ velocities. The trajectories of triple points were mapped using a numerical smoke foil technique. The cellular structures formed for these three mixtures were nearly identical. Large-scale cells were found to be incomplete and composed of a hierarchy of smaller cellular structures, which is characteristic behavior for extremely high activation-energy mixtures.

The reaction zone structure formed by a detonation propagating through nonuniform methane-air mixtures in which the gradient in fuel concentration is normal to the direction of propagation was also investigated for three different linear concentration gradients centered about the stoichiometric concentration. The reaction zone structure, which involved two distinct burning regimes, was similar for all three cases. The leading edge of the reaction zone is an unstable detonation wave. Behind the detonation, excess fuel and oxidizer that are not consumed by rich and lean parts of the detonation front mix and burn in a turbulent diffusion flame. The resulting reaction-zone structure is qualitatively similar to the triple flame detonation wave (TFDW) described by Calhoun and Sinha [91]. Transverse waves were found to propagate along the detonation front in a manner similar to that observed in uniform mixtures. When the initial detonation was overdriven, multiple cells were able to fit inside the channel, and their size varied from smaller to larger between the regions with more and less reactive mixtures, respectively, which is similar to the behavior observed in analogous experiments [89].

The shape of the detonation front was similar for all three gradients considered, and did not exhibit the curved structure observed in experiments [89, 90]. This is most likely due to the small system size used in these calculations. The distortions in the detonation front caused by the transverse instabilities were large compared to the width of the channel, and local variations in reaction front velocity were large compared to differences in CJ velocities over the range of  $\phi$  considered. Thus, any observed variations in the shape of the reaction front are dominated by detonation instabilities. For larger systems compared to the detonation cell size (such as those considered in experiments [89, 90]), where many triple points can form and interact, the influence of channel size would be less pronounced. Propagation velocity would be slower in the very lean and very rich portions of the gradient and would lead to a curved detonation. In future work, we plan to perform a more systematic study of this system-size effect as well as to explore the effect of the various properties of the gradient on detonation propagation. Two important questions are how does the magnitude of the gradient affect the detonation cellular structures and does the presence of the turbulent diffusion flame help to support detonation propagation.

More investigation is needed in order to discuss how characteristics of the concentration gradient affect the structure, propagation speed, and cellular instabilities of two-dimensional detonations, and, likewise, how the concentration gradient affects turbulent flame acceleration and DDT.

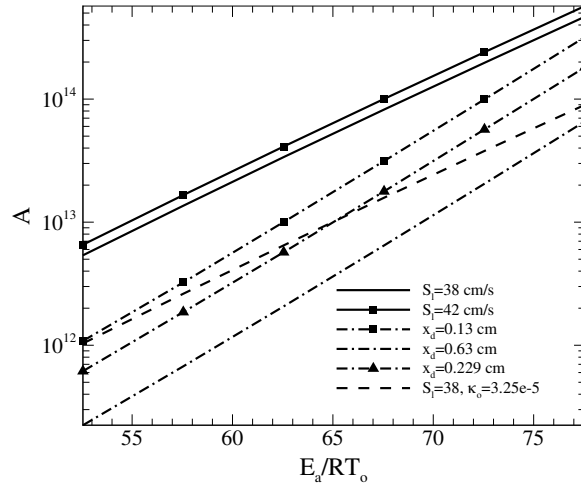


**Figure 3.28.** Curves of constant  $x_d$  and  $S_l$  in the  $E_a$ - $A$  parameter space computed using 1D steady-state flame and ZND detonation codes in conjunction with the two-component reaction model with  $qM/RT_0 = 39.0$  and  $\gamma = 1.197$ . The two curves for  $x_d$  with bold dash-dot lines indicate uncertainty in correlation between detonation cell size and  $x_d$ . A third dash-dot line shows constant  $x_d = 0.229$  cm, the value used for calibration of the single-component reaction model. The two solid curves for  $S_l$  are computed assuming  $\kappa_o = 6.25 \times 10^{-6}$  g/s-cm-K<sup>0.7</sup>. The dashed curve for  $S_l = 38$  cm/s is computed for a higher  $\kappa_o = 3.25 \times 10^{-5}$  g/s-cm-K<sup>0.7</sup>.

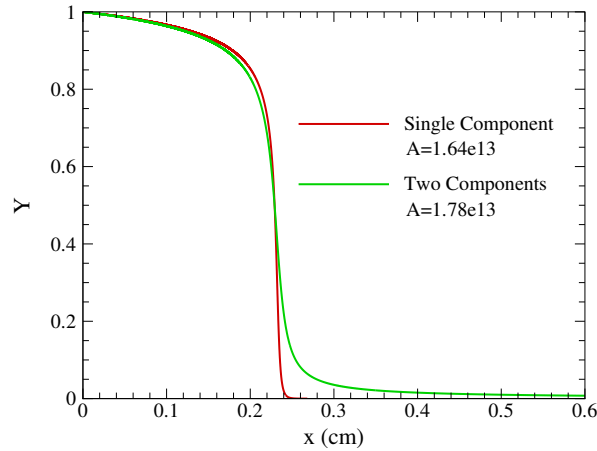


**Figure 3.29.** One-dimensional detonation structures computed using the single-component reaction model with  $A = 1.64 \times 10^{13}$  cm<sup>3</sup>/g-s (red line) and the two-component reaction model with  $A = 1.78 \times 10^{13}$  cm<sup>3</sup>/g-s (green line). The same  $q$ ,  $\gamma$ , and  $E_a$  were used for both calculations (cf. Table 2 and Table 7). In both cases,  $x_d = 0.229$  cm.

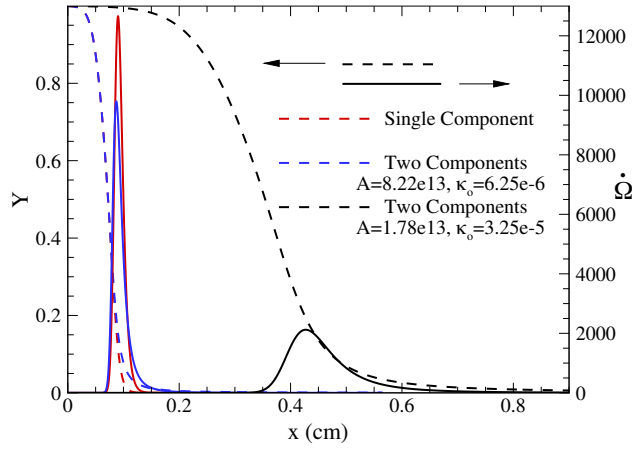


**Figure 3.30.** One-dimensional laminar flame structures computed for various  $A$ ,  $E_a$  parameter sets. Dashed lines indicate reaction rates and correspond to the right  $y$ -axis. Solid lines indicate fuel mass fractions and correspond to the left  $y$ -axis. Red lines represent the flame structure obtained using a single-component reaction model and the parameters in Table 2. Flame structures computed using two-component models with the same  $q$ ,  $\gamma$ , and  $E_a$  are shown for which  $S_l = 40.35$  cm/s and  $x_d = 0.229$  cm (black lines) and for which  $S_l = 40.35$  cm/s and  $x_d = 0.05$  cm (blue lines). For the former case,  $\kappa_o$  was taken to be larger than that of air in order to match  $S_l$  and  $x_d$  with the same set of parameters.

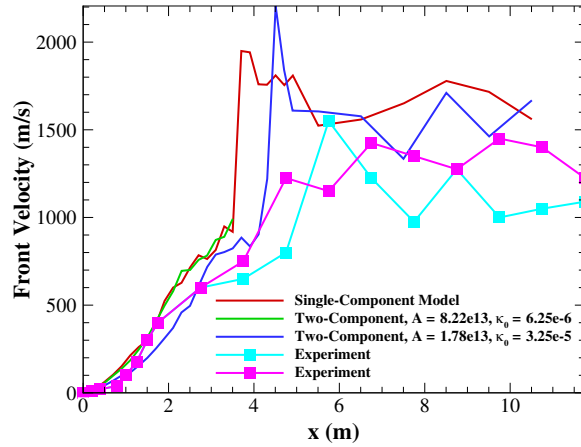


**Figure 3.31.** Velocity of the leading edge of the flame front as a function of position in Configuration 17.4 with  $\xi = 0.3$  computed using the three reaction models described in Figure 3.30. Experimental data for two 9.5% methane-air mixtures are taken from [72]

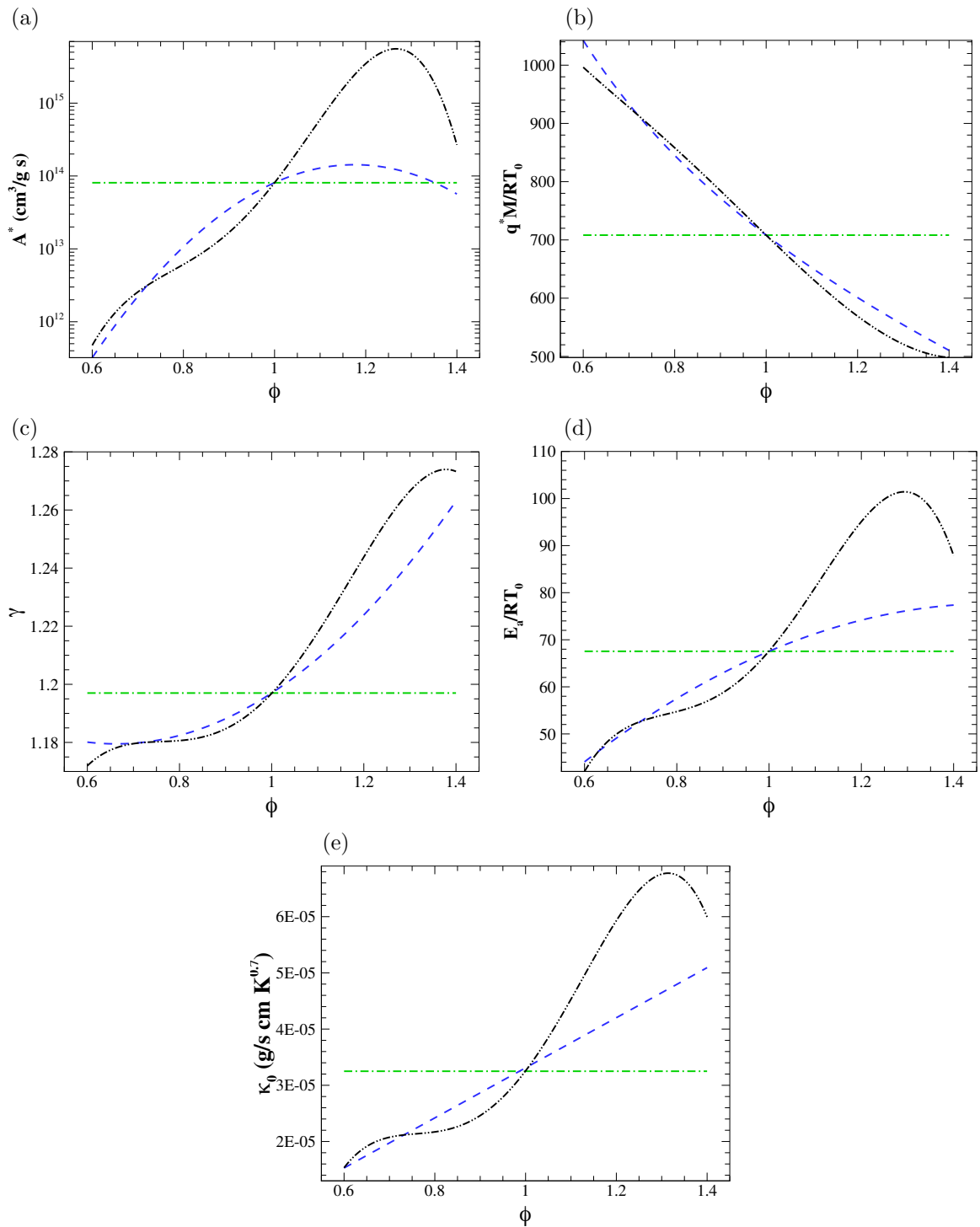


**Figure 3.32.** Values of (a)  $A^*$ , (b)  $q^*M/RT_0$ , (c)  $\gamma$ , (d)  $E_a/RT_0$ , and (e)  $\kappa_0$  as a function of  $\phi$  computed using Eqs. (3.17–3.21) (dashed blue lines), Eqs. (3.22–3.26) (dash-dot-dot black lines), and constant parameters (dash-dot green lines).

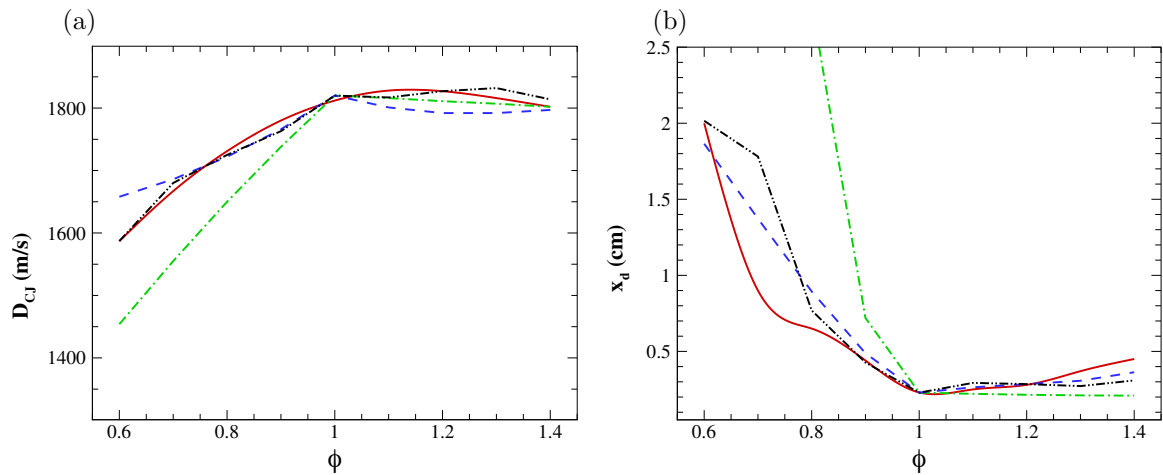


**Figure 3.33.** (a)  $D_{CJ}$  and (b)  $x_d$  computed using one-dimensional ZND equations assuming constant reaction and transport parameters (dash-dotted green lines), Eqs. (3.17–3.21) (dashed blue lines), and Eqs. (3.22–3.26) (dash-dot-dot black lines) compared to target values (solid red lines).

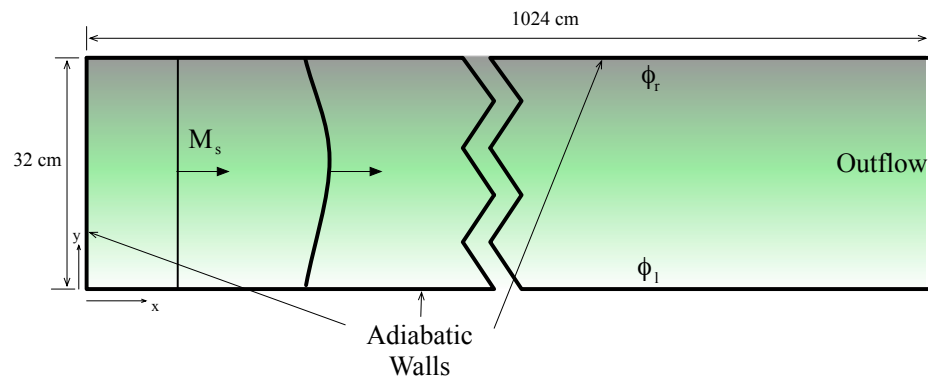


**Figure 3.34.** Schematic of computational domain for detonation propagation through a gradient in fuel concentration. The equivalence ratio of the mixture varies linearly from a maximum of  $\phi_r$  at the top of the channel to a minimum of  $\phi_l$  at the bottom of the channel. A detonation is ignited directly by a strong shock with Mach number  $M_s = 10$  near the closed end of the channel. For all cases, the width of the channel is 32 cm, and its length is 1024 cm.

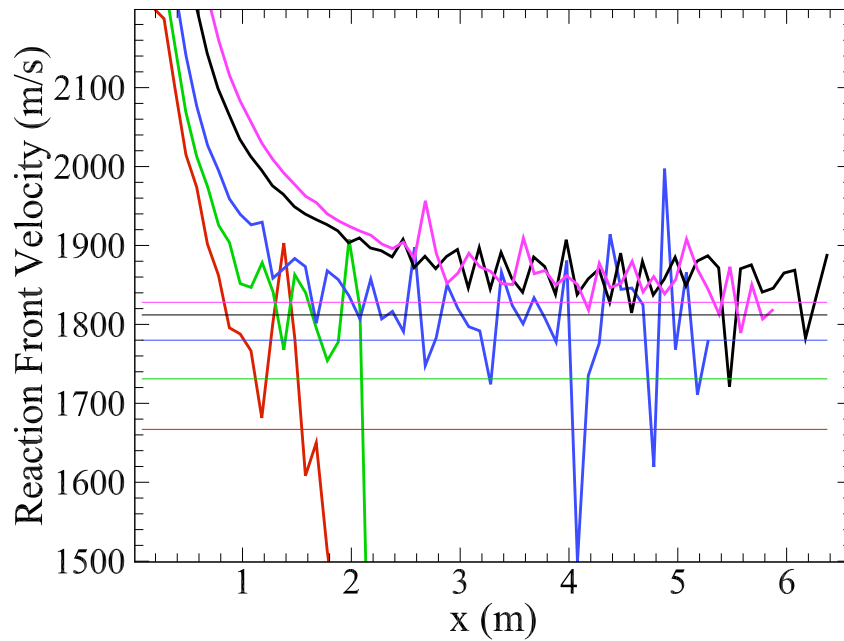


**Figure 3.35.** Velocity of the leading edge of the reaction front as a function of its distance from the closed end of the channel for uniform ( $\phi_l = \phi_r$ ) methane -air mixtures with  $\phi = 0.7$  (red lines), 0.8 (green lines), 0.9 (blue lines), 1.0 (black lines), and 1.1 (purple lines) along with the value of  $D_{CJ}$  for each mixture (thin horizontal lines of the same color).

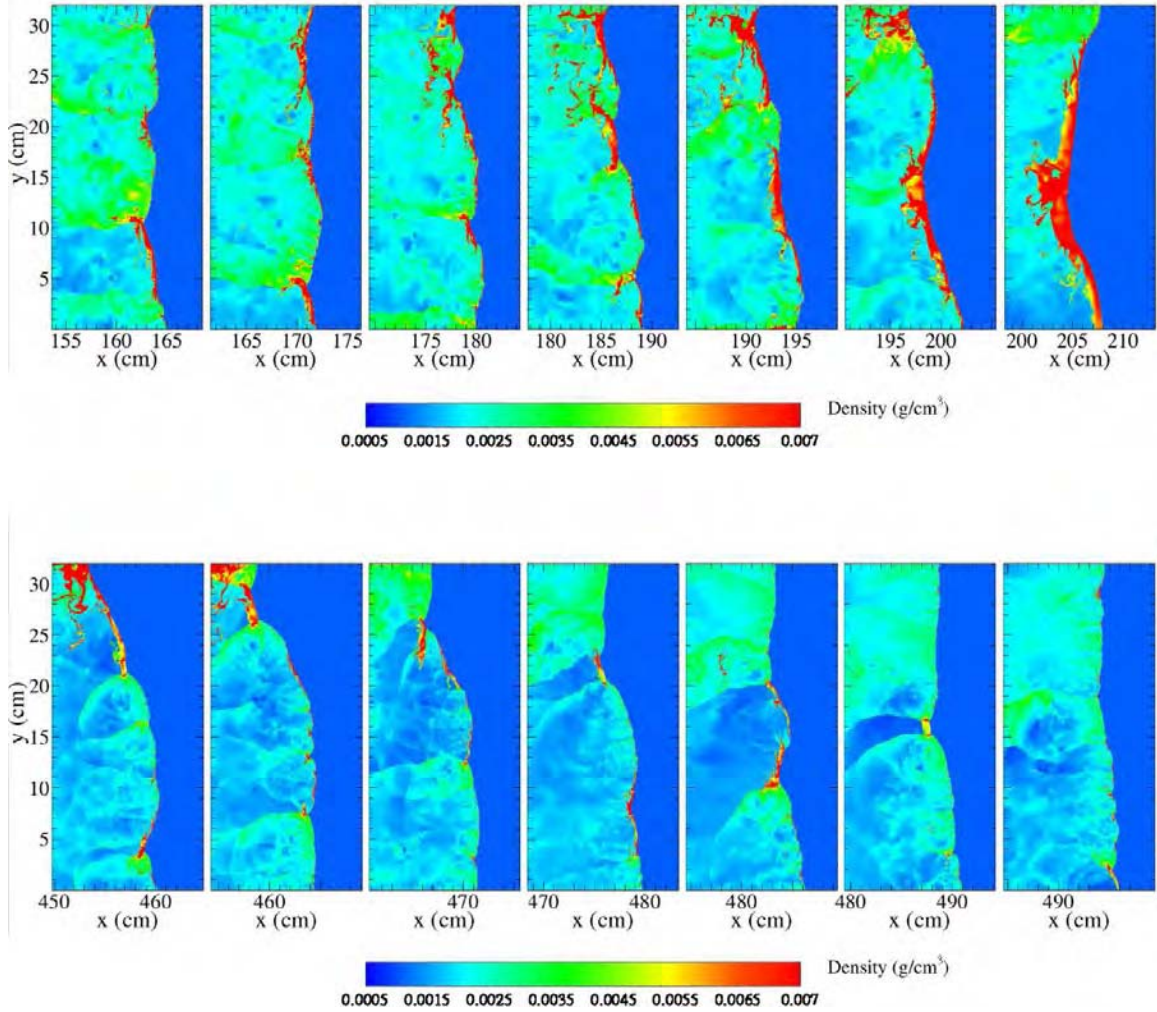


**Figure 3.36.** Selected density maps of the full channel width in the vicinity of the reaction front at several instants in time for a detonation propagating through a uniform (a)  $\phi = 0.7$  and (b)  $\phi = 1.0$  mixture.

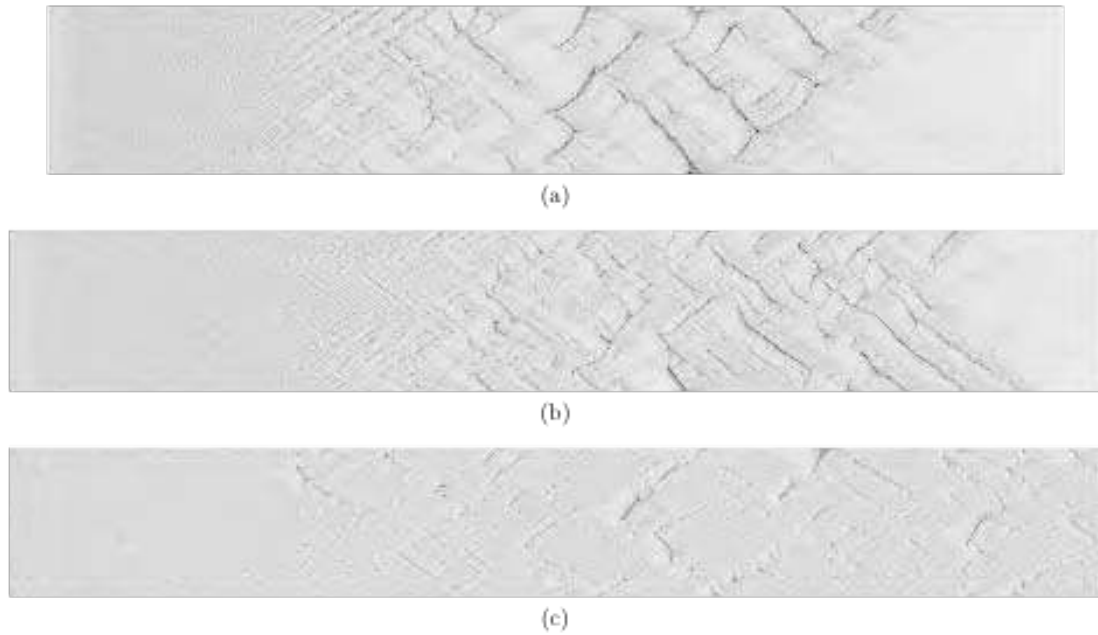


**Figure 3.37.** Numerical smoke foils produced by detonations propagating through uniform mixtures with (a)  $\phi = 0.7$ , (b)  $\phi = 0.8$ , and (c)  $\phi = 1.0$ .

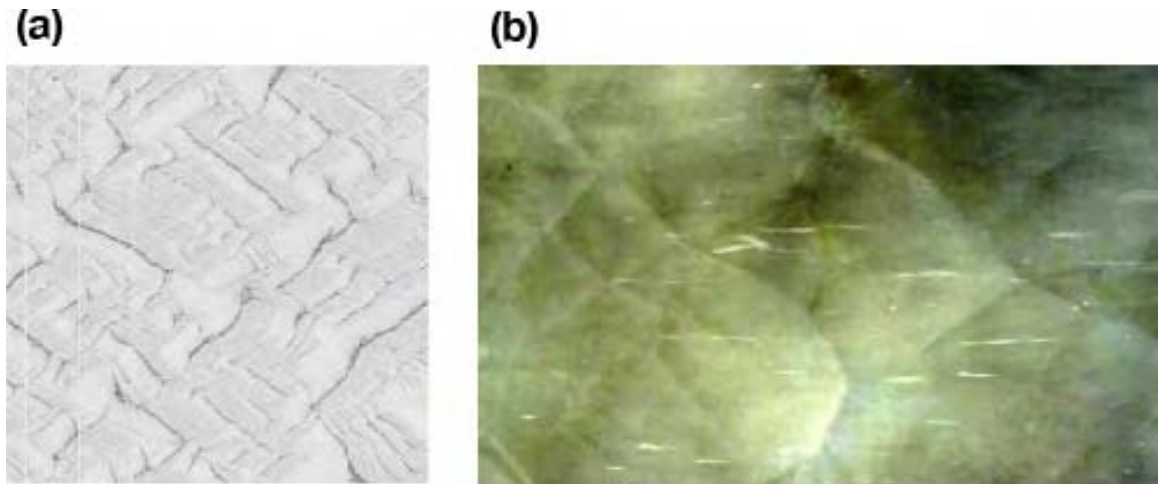


**Figure 3.38.** Close-up view of cellular structures recorded on (a) a numerical smoke foil produced by a detonation propagating through a uniform stoichiometric ( $\phi = 1$ ) mixture and (b) a portion of an experimental smoke foil generated by detonation of a uniform near-stoichiometric (10% methane) mixture. Experiments were conducted in a 1.05 m diameter and 73 m long, partially-closed tube with smoke foil attached at the open end. The dimensions of the numerical smoke foil and the portion of the experimental smoke foil shown in (b) are roughly the same 32 cm wide by 48 cm long. The direction of detonation propagation was from left to right in the figure. Photo courtesy of R. Karl Zipf (NIOSH).

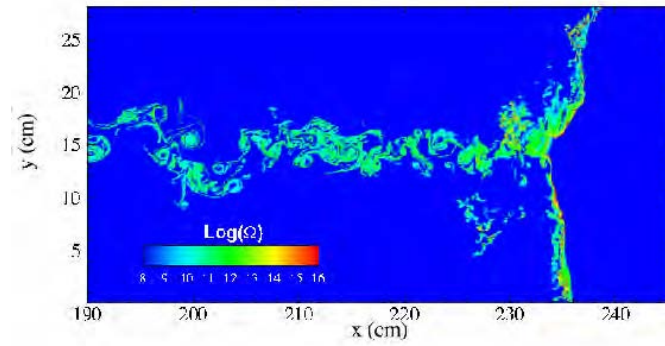


**Figure 3.39.** Maps of the logarithm of the reaction rate for a detonation propagating through a 32cm-wide channel with a gradient in fuel concentration that varies linearly from  $\phi_r = 1.1$  to  $\phi_l = 0.9$ .

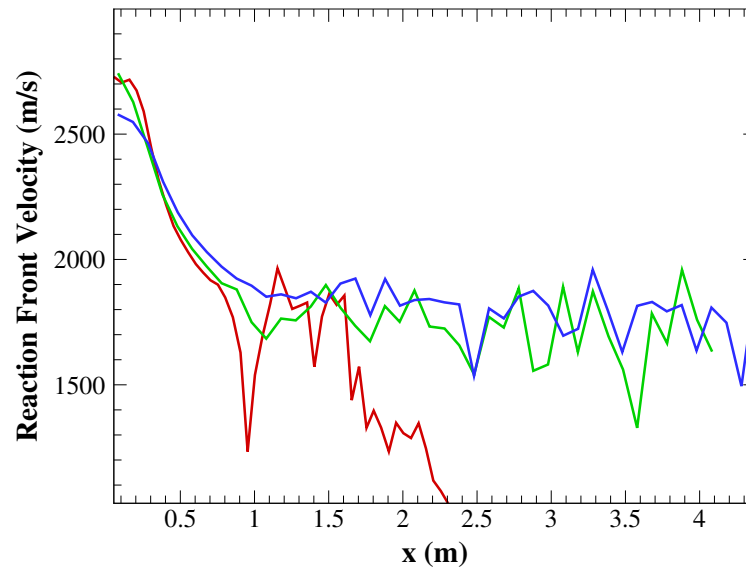


**Figure 3.40.** Velocity of the leading edge of the reaction front as a function of its distance from the closed end of the channel for methane -air mixtures with concentration gradients  $\phi_r = 1.3$  and  $\phi_l = 0.7$  (red line),  $\phi_r = 1.2$  and  $\phi_l = 0.8$  (green line), and  $\phi_r = 1.1$  and  $\phi_l = 0.9$  (blue line).

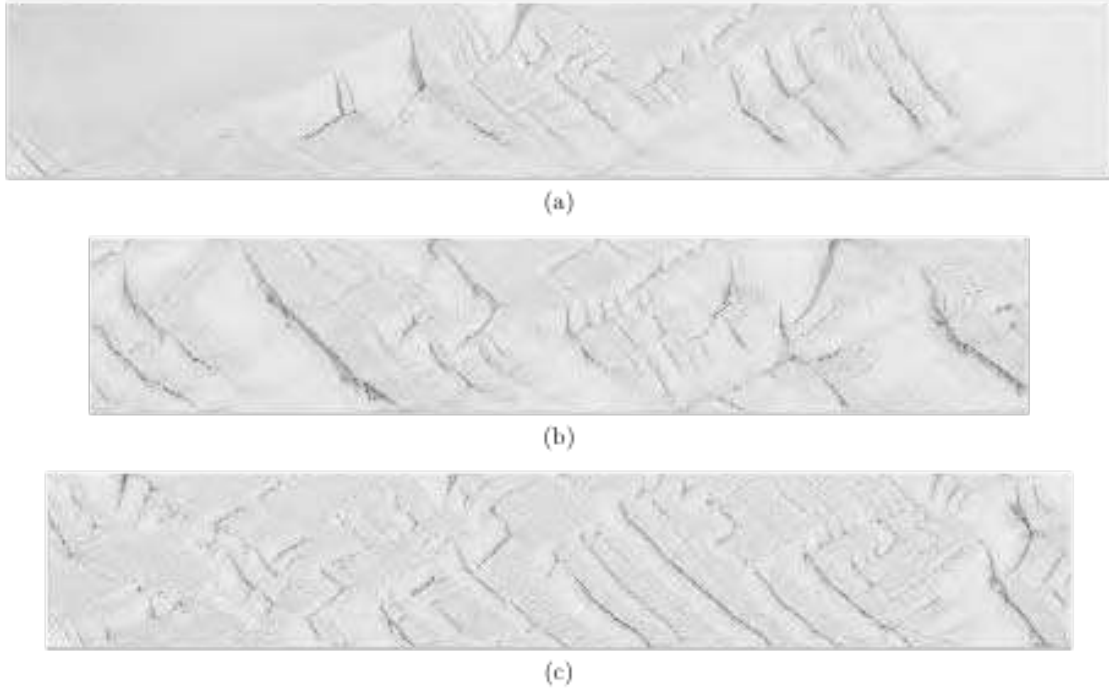


**Figure 3.41.** Numerical smoke foils produced by detonations propagating through concentration gradients of (a)  $\phi_r = 1.3$  and  $\phi_l = 0.7$ , (b)  $\phi_r = 1.2$  and  $\phi_l = 0.8$ , and (c)  $\phi_r = 1.1$  and  $\phi_l = 0.9$ .

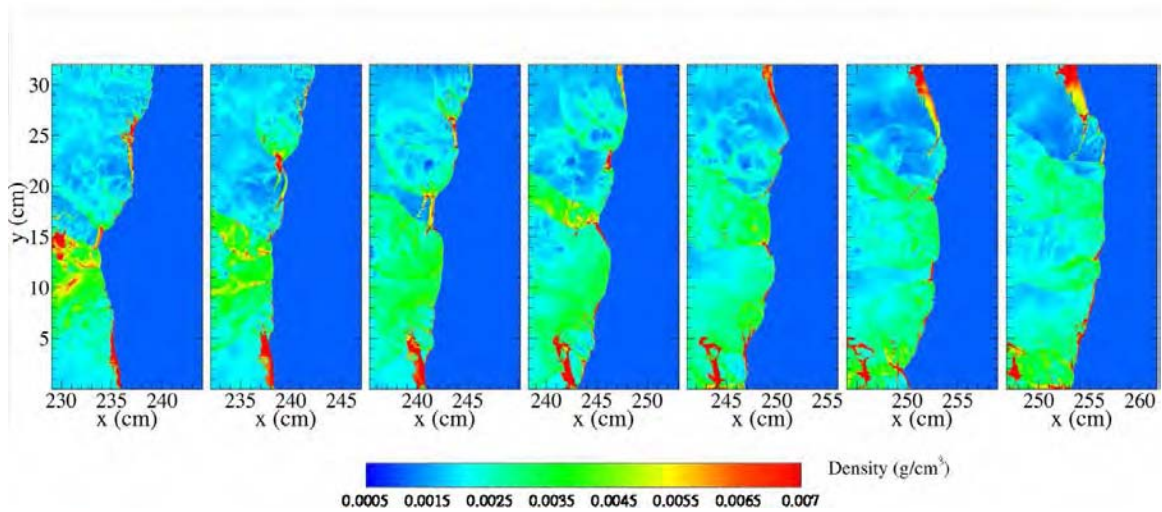


**Figure 3.42.** Selected density maps of the full channel width in the vicinity of the detonation front at several instants in time as it propagates through a concentration gradient with  $\phi_r = 1.1$  and  $\phi_l = 0.9$ .

## 4. Measuring Detonability

### 4.1 Background

This work was initiated to address safety concerns related to explosive gas mixtures that form in coal mines. These are essentially mixtures of air and natural gas (NG) released from coal beds. Similar explosive mixtures may form during production, transportation, or utilization of NG. Though accidental NG explosions occur in deflagration regimes, the worst-case scenario involves detonations that can be extremely destructive and generate dynamic pressures up to 10 MPa on reflections. It is therefore very important to know at what conditions NG-air mixtures can or cannot detonate. These conditions include (1) the composition of the mixture, (2) the pressure and temperature of the mixture, (3) the size and the geometry of confinement, and (4) the method of detonation initiation.

Here we will largely ignore the condition (2) since we only consider NG-air mixtures at 0.1 MPa and temperatures around 298 K, within seasonal outdoor variations. The remaining three conditions may vary, and we will discuss them below. The DDT as a method for detonation initiation will be discussed separately in section 4.1.3.

#### 4.1.1 Effect of NG Composition on Detonability of NG-air Mixtures

The composition of NG is not strictly defined and typically includes 82-99% of CH<sub>4</sub> by volume depending on the gas origin [96, 97], as well as ethane, propane, and smaller amounts of even higher hydrocarbons. A few percent of nitrogen and CO<sub>2</sub> can also be present. A typical coalbed gas (often called coalbed methane) usually contains less than 2% of ethane and heavier hydrocarbons, but sometimes may include up to 15% of CO<sub>2</sub> [98, 99].

The variability of NG composition results in large uncertainties in explosive properties of NG-air mixtures. It has been shown, for example, that small additives of ethane, propane, and higher alkanes significantly decrease ignition delays in CH<sub>4</sub>-O<sub>2</sub> and CH<sub>4</sub>-air mixtures [96, 97, 100]. For example, the induction length  $\delta$  of a ZND detonation in stoichiometric methane-ethane-air mixtures computed in [100] can be approximated as

$$\delta/\delta_0 = 1 - 13.52 * x + 167.5 * x^2 - 1370 * x^3 + 5846 * x^4 - 9625 * x^5 \quad (4.1)$$

where  $\delta_0 = 2.41$  cm is the induction length for CH<sub>4</sub>-air, and  $x \leq 0.2$  is the volume fraction of ethane in the methane-ethane mixture. According to this equation, 8% ethane in the fuel reduces the induction length by a factor of 2.

The NG used in GETF experiments described in Section 4.3 contained 1.5–1.7% of ethane and only trace amounts of higher hydrocarbons. According to Eq. (4.1), 1.5–1.7% of ethane in NG decreases the induction delay by a factor of 0.8 compared to a pure CH<sub>4</sub>.

Ignition delays usually correlate with the energy required for the detonation initiation and the detonation cell size, both of which characterize the detonability of the mixture. Thus, the detonability of NG-air varies with NG composition, and can significantly differ from that of CH<sub>4</sub>-air. For example, the strong effect of

ethane on the initiation energy has been shown in [101] for stoichiometric methane-ethane-air mixtures. When the ethane concentration in fuel decreased from 30% to 10% by volume, the minimum energy required for the detonation initiation in cylindrical geometry increased exponentially from 12.5 kJ/cm to 25 kJ/cm. A rough extrapolation to lower ethane concentrations shows that the initiation energy may increase by two orders of magnitude for pure CH<sub>4</sub>-air. A similar extrapolation of experimental results [102] obtained for CH<sub>4</sub>-O<sub>2</sub>-N<sub>2</sub> mixtures using the same experimental setup gives the initiation energy for CH<sub>4</sub>-air around 7.5 MJ/cm. Both of these extrapolations are far-fetched and can be wrong by an order of magnitude, but the results show that NG composition can drastically change the detonability of NG-air mixtures.

#### 4.1.2 Detonability of Natural Gas-Air Mixtures

Because of the stability of the methane molecule, CH<sub>4</sub>-air is the most insensitive hydrocarbon-air mixture with respect to detonation initiation. There are still no confirmed reports of successful initiation of self-supported detonations in unconfined NG-air or methane-air mixtures. An earlier report [103] that claimed detonation initiation using 1 kg of TNT inside a 3 m rubber sphere filled with methane-air was analyzed in [104] with a conclusion that the observed detonation was most likely decaying. There is also some uncertainty in the exact mixture composition since the purity of methane used in experiments [103] is not specified. Report [105] describes “erratic, uneven detonations” initiated in bags filled with NG-air mixtures using 1001-1020 g of high explosive. These unsteady detonation regimes were observed only for NG concentrations 8.6-8.8%, though tested mixture concentrations ranged from 5.2% to 12.5%. Extrapolation of experimental results [104] obtained for various CH<sub>4</sub>-O<sub>2</sub>-N<sub>2</sub> mixtures suggests that detonation initiation in unconfined methane-air would require about 22 kg of tetryl. Large-scale experiments [106] have shown that 37 kg of Composition B did not initiate a detonation in a stoichiometric methane-air (9.5% CH<sub>4</sub>) in an unconfined hemispherical geometry.

There are only two published works in which high explosives were used to initiate methane-air detonations in tubes. Early experiments [107] carried out at the Bureau of Mines Experiment Station at Pittsburgh have shown that 50 g of a high explosive (65% ammonium nitrate/14.6% TNT/20.3% sodium chloride) initiate a detonation-like wave inside a 30.5 cm diameter tube filled with a methane-air mixture containing 9.1% of CH<sub>4</sub>. The wave velocity measured in the 3.65 m long tube varies between 1820 and 1950 m/s, which is slightly higher than the calculated  $D_{CJ}$ =1801 m/s. The authors conclude that the observed regime is not a “true” detonation and it is partially supported by the energy of the initiator.

A longer, 11.2 m tube of the same 30.5 cm diameter was used in experiments [108], in which detonations were initiated using 50 g and 70 g of a slightly more powerful high explosive (50% ammonium nitrate / 50% TNT). The author observed the detonation propagation using multiple optical windows, and concluded that steady-state detonations are possible for mixtures containing from 6.3% to 13.5% of methane. The methane used in these experiments was, in fact, a natural gas that contained ~ 2% of higher hydrocarbons.

The difficulties encountered in initiating self-supporting detonations in methane-air using high explosives may create a perception that methane-air mixtures can only detonate under extraordinary circumstances not seen in the practical world. A number of experiments with different methods of detonation initiation have shown that this perception is wrong. Detonations in methane-air have been ignited in confined conditions using booster detonations in more sensitive gas mixtures [109, 110] or deflagration-to-detonation transition

(DDT) in smooth [2, 111] or obstructed [72, 112–114] channels. Still, available experimental data on detonations in methane-air mixtures are very limited because detonation experiments using these mixtures usually require large facilities. Ideally, a detonation tube should be wide enough to fit several detonation cells, and the tube length should be sufficient to observe a self-supporting quasi-steady-state detonation.

Detonation cell sizes measured in a 183 cm diameter tube [110] for 9.6% methane-air mixture are about 28 cm. Cell sizes measured in a 52 cm diameter tube [72] vary between 13 and 29 cm for the stoichiometric mixture, and can increase to the tube width for lean (8.5% CH<sub>4</sub>) and rich (12% CH<sub>4</sub>) mixtures. The wide range of measured cell sizes reflects the fact that cellular structures in methane-air are very irregular.

In smaller tubes, methane-air detonations can only propagate in a spinning mode. This mode, initiated in a 6.35 cm wide square tube with a hydrogen-oxygen booster, has been used in [109] to determine initiation energies for methane-air mixtures of different concentrations. The minimum initiation energy of 9 MJ/m<sup>2</sup> has been obtained for 11% CH<sub>4</sub>. Lower and upper detonability limits determined for methane-air in the same experiments are 8% and 14.5% CH<sub>4</sub>. The smallest tube diameter in which a methane-air detonation was ever observed is 3.6 cm [114]. Detonability limits reported in [114] for a 5 cm diameter tube are 7.5% and 11.5% CH<sub>4</sub>.

The range of methane concentrations and tube diameters discussed are related to the ability of NG-air mixtures and particular geometries to support detonation propagation, no matter how this detonation is initiated. For practical systems, however, it is often important to know whether a detonation can develop from a weak ignition source, that is, whether a DDT can occur for a particular geometry and mixture composition.

#### *4.1.3 Experimental Studies of DDT*

There are several ways DDT has been studied experimentally. In the first type of experiments, an energetic gas is contained in a long channel closed at one end, and ignited with a spark near the closed end. The resulting, initially laminar flame accelerates, becomes turbulent, and eventually may produce a detonation. (See, e.g., [115]). Two basic scenarios of DDT were observed: sometimes a detonation appears inside the region containing the turbulent flame, and sometimes it forms in the preheated, compressed material between a leading shock wave and the flame. Experiments [116, 117] have shown that for these scenarios boundary layers play a key role in the flame acceleration and turbulence generation.

A second type of experiment (based on the work of Markstein [118]) used a shock-flame interaction to create the turbulent flame more quickly [39, 119–121]. A flame was ignited by sparks at a distance from a reflecting wall, and then a shock was released at the opposite end of the tube. The flame interacted first with the incident shock and later with the shock reflected from the end wall. Shock-flame interactions distorted the flame, making it turbulent and increasing the energy-release rate in the system. These experiments showed a number of specific DDT-related phenomena and well-defined trends on which simulations could be focused. For example, whether and where DDT occurred in the system depended on the Mach number of the incident shock. For the lowest Mach numbers, the reflected shock was amplified by the turbulent flame, but there was no DDT. For intermediate Mach numbers, DDT occurred between the flame brush and the reflected shock. For the highest Mach numbers, DDT occurred inside the flame brush. Whenever DDT occurred, the transition was through a very rapid explosion whose details could not be determined from the

experiment.

A substantial body of experimental work has since shown that the presence of obstacles along the walls of the channels results in much faster flame acceleration and transition to a detonation than if no obstacles were present. Channels with obstacles provide a convenient environment in which DDT can be studied in a controlled manner. This technique was first used in experiments [122, 123], and it has been extensively applied in combustion research since then [60–71, 124, 125]. Today it has become a model for evaluation of fuel safety using laboratory experiments. Turbulent flames propagating in channels with obstacles often accelerate to supersonic velocities, and may trigger detonations if the channel is large enough. The distance to DDT in these experiments depends on the mixture reactivity, channel width, and obstacle configurations. A detailed discussion of experimental results obtained for different mixtures, including generalized correlations, can be found in the recent review [126].

Finally, controlled experiments attempting to observe unconfined DDT [127–129] showed that a transition to detonation induced by turbulent flames in systems without walls or obstacles is rather difficult. This can be partially attributed to the lack of shock-reflecting surfaces. It can also be partially due to geometrical effects of expansion: shocks proceeding from a deflagration might be weakened, or turbulence might be damped too much by the expansion, and so they become unable to precondition the gas for DDT. Wagner and coworkers [127] report experiments in which deflagrations were forced to DDT by passing through screens of specified mesh sizes. The screens created turbulence of the required scale and intensity. These experiments suggest that an unconfined deflagration could make the transition to detonation under the right conditions.

A related problem that was studied experimentally is initiation of detonations by turbulent jets [128, 130–133]. In these experiments, a jet of hot combustion products was injected into an unburned, cold mixture. The turbulence created by the interaction of this jet and the background gas created a nonuniform, preconditioned region in which detonation could occur. These experiments provide important information on the critical size of the region capable of triggering DDT when the effects of reflected shocks and interactions with walls are minimal.

The most extreme case of unconfined DDT is an initially laminar flame inside a very large volume of a reactive mixture with no pre-existing turbulence or shocks. In the absence of effective mechanisms for turbulence generation, such as shock-flame interactions and wakes, laminar flames become turbulent through other, relatively slow mechanisms, such as Darrieus-Landau and thermal-diffusive instabilities. In the presence of gravity, the buoyancy-driven Rayleigh-Taylor (RT) instability might become a dominant mechanism for turbulence generation. The developing turbulence, however, might be damped by expansion. The size of an unconfined system in which DDT could be observed is expected to be relatively large. It has been suggested, for example, that DDT might occur in very large vapor clouds [134, 135].

Analysis of experimental data shows that turbulence plays an important role in DDT. Several apparently different mechanisms for the DDT have been described, each including the effects of turbulence and formation of shocks. On large scales, turbulence deforms the flame front and increases its surface area. On small scales, it can broaden the flame front and cause mixing. The result is an extended turbulent “flame brush” in (or near) which a series of explosions occurs. One of these explosions finally leads to a detonation. Other routes to detonation may include an explosion in the boundary layer, or an explosion in the region between the

leading shock and flame brush.

This summary of observational evidence gives a general picture of when and where DDT might occur, and the importance of fluid instabilities in creating the turbulent background in which a detonation is more likely to appear. Available experimental data, however, do not directly show how a detonation appears. Studies of intrinsic mechanisms by which detonations form require a combination of experimental, numerical, and theoretical approaches [5].

## 4.2 Gas Explosion Test Facility at NIOSH Lake Lynn Laboratory

Experiments were carried out at the Gas Explosion Test Facility (GETF) at NIOSH Lake Lynn Laboratory (LLL). The facility consists of the detonation tube, supporting systems for gas injection, mixing, sampling and analysis, the ignition system, the diagnostic equipment, and a remote control system. Pictures of the facility are shown in Figure 4.1, and a schematic diagram is shown in Figure 4.2.

### 4.2.1 Detonation Tube

The tube is located in the upper quarry of LLL, and is fabricated from sections of hot-rolled and welded industrial steel pipe. The total length of the tube is 73 m, and the internal diameter is 105 cm. The straight tube rests in plane on 18 equally-spaced concrete blocks weighing about 1.8 t each, and is attached to these blocks with 9.5 mm galvanized steel cable. The tube is inclined about 2 deg, so that the open end is about 2.5 m higher than the closed end.

The closed end is permanently sealed with a 12.7 mm welded steel plate, and rests against a 14 t concrete block poured between the tube and a 5-m-high earthen berm, as shown in Figure 4.1 (left). The total weight of the pipe, concrete supports, and the earthen berm that resists the tube recoil is at least 175 t. The open end of the tube is located about 15 m from the 20-m-high quarry wall. A 15 t concave ramp deflector fabricated from curved steel H-beams is installed at about 2 m from the open end, leaning against another berm. The deflector is designed to direct shock waves upward into the atmosphere in order to minimize strong shock reflections from the quarry walls.

The steel pipe has a wall thickness of 9.5 mm, minimum yield strength of 248 MPa, and an ultimate tensile strength of 414 MPa. For stoichiometric methane-air mixtures, the quasi-static Chapman-Jouguet detonation wave pressure is 1.66 MPa, and that pressure could persist for time periods longer than 0.1 second. Based on hoop stress calculations with this quasi-static pressure, the safety factor against deformation is about 2.70, and the safety factor against rupture is 4.50. Higher pressure pulses with shorter durations affect the tube walls in the vicinity of the detonation front, during shock reflections, and during the detonation initiation. The highest dynamic pressure recorded so far at GETF is about 7 MPa, and the tube shows no evidence of deformation or damage.

#### 4.2.2. Gas Mixing and Analysis

A very important part of GETF is the gas mixing system that enables creation of homogeneous methane-air test mixtures inside the tube with predefined equivalence ratios. The mixing system consists of an enclosed blower fan, an intake manifold, and an exhaust manifold. The 2.25 kw blower fan delivers 26.5 m<sup>3</sup>/min operating at 27.2 cm of water static pressure. Manifolds are made with 10 cm diameter pipe, and they are connected to the detonation tube through 7.5 cm inlet and outlet riser pipes. The riser pipes are equipped with manual 10 cm ball valves that can be used to balance the flow from each inlet and outlet; however, in these experiments, all the valves were open. There are also two remotely operated ball valves between the blower fan and manifolds. These are open during the mixing process, but closed before ignition to protect the fan.

Prior to filling the explosion tube with methane to obtain the desired test mixture composition, a 0.15-mm-thick plastic diaphragm is placed over the open end of the tube. Natural gas is introduced into the intake manifold at the beginning of the mixing process.

As shown in the schematic in Figure 4.2, the intake manifold has six evenly-spaced inlets, with three located on each side of the blower fan. The exhaust manifold has seven outlets, with three on one side of the blower fan and four on the other. The first riser pipe located about 100 cm from the closed end of the tube is an outlet, that is mixture flows out of the manifold into the tube. The second riser is an inlet, in which mixture flows into the manifold from the tube. The third riser is an outlet; the fourth riser is an inlet, and so on. The last riser located about 82 cm from the open end, is an outlet.

When the blower fan operates, the gas mixture in the tube is drawn into the inlet risers, through the intake manifold, through the blower, through the exhaust manifold, and then reinjected through the outlet risers. Since both inlets and outlets are distributed along the length of the detonation tube, the system has multiple recirculation circuits that merge in the intake manifold and split in the exhaust manifold, thus providing efficient gas mixing. The volume of the detonation tube is 63.4 m<sup>3</sup>. The 2.25 kw blower fan moves 26.5 m<sup>3</sup>/min, and thus the air change time is less than 3 min. To achieve a homogeneous test mixture, typical mixing times range from 30 to 45 min.

A sample draw system enables the remote collection and analysis of samples of the test mixture. During gas mixing, samples are drawn continuously from the closed end, middle, and open end of the tube back to an infrared gas analyzer (Siemens Ultramat 23) located about 300 m away from the detonation tube in the control building. Collected samples are then returned to the detonation tube by a reinjection line, except for a small portion passing through the gas analyzer. The sample draw system provides real-time gas concentrations at three different locations along the tube and assures homogeneity of the test mixture.

The mixture composition in the tube is controlled in three different ways. First, a pre-calculated amount of natural gas is injected into the tube using a conventional natural gas meter (Sensus 135 S-275). Second, gas samples are analyzed with the remote infrared gas analyzer during mixing. Finally, two samples of the gas mixture are drawn after the mixing is completed, and later analyzed off-site using gas chromatography. In most experiments with this detonation tube, the desired concentration of natural gas in the test mixture was created with the accuracy  $\pm 0.2\%$  by volume.

#### 4.2.3. Ignition

To ignite a detonation in the NG-air test mixture, a large plastic bag filled with a stoichiometric methane-oxygen mixture is placed at the closed end of the tube. The bag is made of 0.15 mm plastic film and has a cylindrical shape with a diameter of about about 1 m. The bag volume typically varies between about 3 m<sup>3</sup> and 6 m<sup>3</sup> from one series of experiments to another. Smaller bags, 1.5, 0.75, and 0.375 m<sup>3</sup>, were also used in several experiments to test the effect of the ignition energy.

To inflate the bag, separate methane and oxygen tanks are used to meter pre-calculated amounts of each gas via orifices into the bag. Gas was administered through separate lines with check valves and flash back arrestors in each line. The bag is inflated remotely after NG-air mixing in the tube is complete.

Detonation in the stoichiometric methane-oxygen mixture is easily initiated with a non-electric #8 blasting cap containing about 0.45 g pentaerythritol tetranitrate (PETN) and placed at about 0.5 m from the closed end of the tube. The methane-oxygen mixture has a detonation cell size of 2-3 mm, propagates with a velocity close to  $D_{CJ} = 2490$  m/s, burns all the mixture in the bag, and generates a strong shock in the tube. This shock may or may not ignite a detonation in the NG-air test mixture, depending on the test mixture composition and the size of the igniter bag.

In experiments without the methane-oxygen booster bag, the NG-air test mixture was ignited directly by an electric match placed near the closed end of the tube. This type of ignition produced a flame.

#### 4.2.4. Baffles

For DDT experiments, for which there was no booster bag, orifice plates (or baffles) with blockage ratio of BR=0.6 were placed inside the tube 1 m apart. The baffles are made of 12.8 mm thick steel and connected with steel rods as shown in Figure 4.3.

#### 4.2.5. Diagnostics

The tube is equipped with 23 quartz-piezoelectric-type pressure transducers and 23 light sensors placed in pairs (pressure + light) approximately every 3 m on the tube wall, as shown in Figure 4.2. The sensors are connected to two separate 24-channel data acquisition units, one of which records all pressure signals, another records all light signals, and both units also record a synchronization signal from a signal generator.

The light sensors are silicon phototransistors (Optek NPN OP800WSL) with a rise time of about 2  $\mu$ s and a spectral response from 600 to 1100 nm. Sensors are mounted at the end of a small tube that is 15 cm long with an inside diameter of 0.32 cm. The field of view for the light sensor is about 5 cm on the opposite side of the 105-cm-diameter detonation tube.

The piezoelectric pressure sensors (PCB Piezotronics CA102B04) have a range of 0-6900 kPa and 1  $\mu$ s rise time. In early experiments with the detonation tube, the pressure sensors were threaded directly into the detonation tube steel. The speed of sound in mild steel is about 5900 m/s, and extraneous vibrations induced in the steel by the methane-air combustion arrive at the pressure sensor prior to the arrival of the detonation wave, which travels on the order of 1800 m/s. To reduce this noise, pressure sensors are decoupled from the tube using double-studded silicone gel anti-vibration mounts, as shown in Figure 4.4.

The data acquisition system (DAS) consists of two separate 24-channel units (National Instruments CompactRIO) with a sampling frequency of 50 kHz. This frequency limits the time resolution for all recorded

signals to  $20 \mu\text{s}$ . The time error between two signals generated by a wave propagating between two sensors located 3 m apart can reach  $40 \mu\text{s}$ . For the detonation velocity 1800 m/s, the uncertainty in position of the detonation wave is 0.072 m in 3 m or 2.4%. Therefore, the uncertainty in the measured detonation velocity is also 2.4% or  $\pm 43$  m/s. If the velocity is constant, the uncertainty is significantly reduced using multiple sensors at greater distances apart.

Before each experiment, two smoke foils are placed between 0.15 and 2.8 m from the open end of the tube. The 1.2-m by 1.2-m foils are made of 1.6-mm-thick aluminum sheets rolled to a 0.5-m radius of curvature, and secured to the inside top of the tube with bolts around the perimeter of the foils. The upstream edge of each foil is inserted into a welded metal slot. The foils are covered with soot produced by acetone flames.

#### *4.2.6. Remote Control System*

Starting from the injection of NG into the detonation tube, all operations necessary for the preparation and conduction of experiments are controlled remotely from the LLL control building located about 300 m from the tube. Firing the primary ignition circuit triggers the data acquisition system. In case the primary circuit fails to ignite the methane-oxygen bag and the test mixture, two additional independent ignition circuits are available to ignite the flammable mixture using electric matches. It is also possible to vent the test mixture to atmosphere using the gas mixing system.

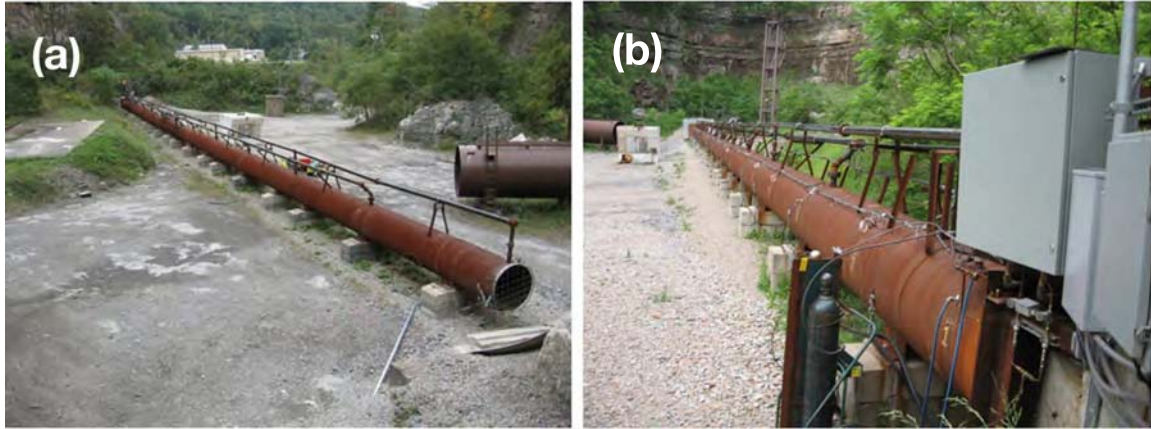


**Figure 4.1** Gas Explosion Test Facility (GETF) at NIOSH Lake Lynn Laboratory. Views from the open (a) and closed (b) ends.

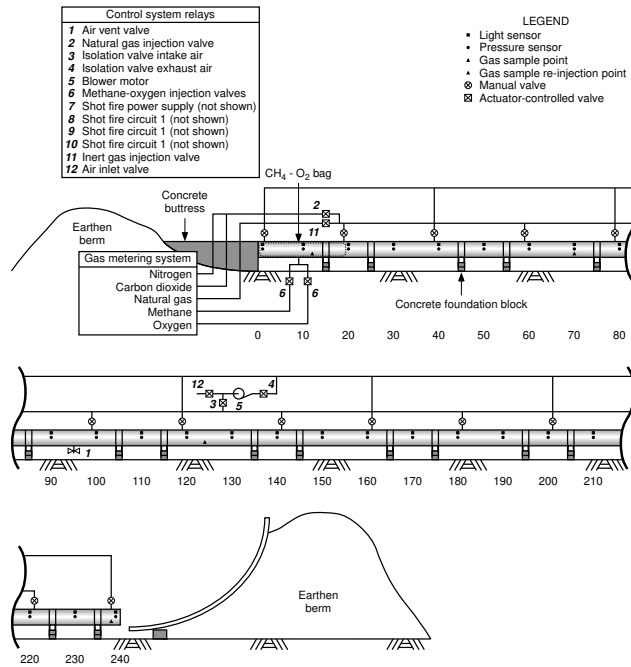


**Figure 4.2** GETF schematics.



**Figure 4.3** Steel baffles with blockage ratio  $BR=0.6$  installed inside GETF tube for DDT experiments.

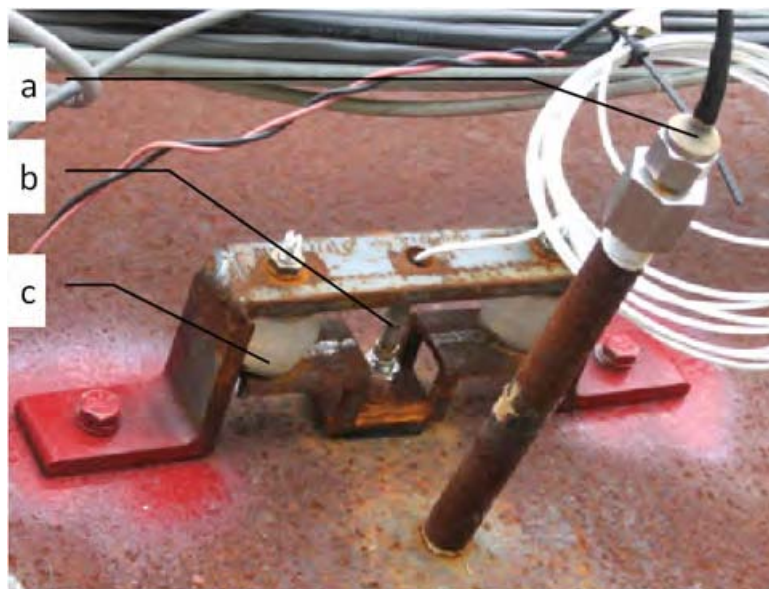


**Figure 4.4** Light (a) and pressure (b) sensors and anti-vibration mount (c).

### 4.3 Interpreting GETF results

GETF was used for two types of experiments:

1. Direct initiation of detonations in NG-air mixtures using a booster detonation in methane-oxygen. The results include detonability limits, detonation cell patterns for the full range of methane concentrations, and detonation velocities and pressures.
2. Flame acceleration and DDT in NG-air mixtures using baffles. The mixture was ignited by an electrical match. The results include flame and shock velocities, pressures, DDT distances, and smoke foil records obtained for various numbers of baffles and mixture compositions.

Here we discuss these results in more detail.

#### 4.3.1. Detonations in NG-Air Mixtures

During 2009 and 2010, more than 40 explosion tests were conducted to determine the detonation characteristics of various mixtures ranging from 4 to 19% NG in air. Each experiment attempted direct initiation of detonation in the test mixture using a bag containing about 2.9 m<sup>3</sup> of methane-oxygen mixture as an initiator. The diagnostic equipment used in these experiments allowed for the identification of detonations using four methods: 1) comparison of measured flame and shock velocities to the computed  $D_{CJ}$  values derived from data taken by pressure and light sensors placed in pairs every 3 m on the tube wall; 2) comparison of the recorded pressures to the computed pressure profiles for ZND detonations; 3) measurement of the separation between the shock and the flame using the time difference between pressure and light signals recorded at the same location; and 4) the patterns produced on smoke foils placed near the open end of the tube.

The results of direct initiation experiments are summarized in Figure 4.5, which shows the measured flame velocity versus methane concentration. The theoretical CJ detonation velocity computed with CHEETAH is also included in Figure 4.5 as a solid line. Detonation in the test mixture is sustainable for methane concentrations from about 5.3 to about 15.5% by volume. The difference between the measured and theoretical detonation velocities is less than 10 m/s or 0.6%. Beyond the detonation limits, the shock velocity decreased to about 500 to 800 m/s for mixtures less than 5% methane in air and to about 700 to 800 m/s for mixtures greater than 16% methane in air. These observed shock velocities are about  $1/2 D_{CJ}$ . Test mixtures with less than 4.9% or greater than 16.0% of methane did not sustain combustion, either by detonation or deflagration, when ignited by the strong methane-oxygen ignition source used in these experiments.

Figure 4.6 shows the measured detonation pressure versus methane concentration. The theoretical CJ detonation pressure is also included as a solid line. Again, there is good agreement between measured and theoretical values, considering that the estimates of the detonation pressure behind the main shock are  $\pm 0.3$  MPa. The maximum CJ pressure, 1.77 MPa, occurs for methane concentration about 10%, and declines as the lower and upper limits are approached. Even at the limits of 5.3 and 15.5%, CJ pressures are still high at about 1.2 MPa and 1.5 MPa, respectively. Thus, a methane-air mixture develops variable but substantial pressures over the entire detonable range.

Figure 4.7 presents measured detonation cell sizes as a function of mixture composition. Tests for mixture compositions in the range of 5.3 to 15.5% CH<sub>4</sub> produced cell patterns, and those outside the range did not. The number of cells in a foil ranged from 1 to 8, depending on the mixture. Near-stoichiometric

mixtures produced a detonation cell size of about 25 cm. With a 7% test mixture, cell size increased to about 55 cm, and with a 15.4% mixture, a single cell measuring 105-cm-wide by 170-cm-long was recorded. The variability of the cell measurements is on the order of 30% due to the irregularity of the cell patterns. Figure 4.7 also includes the computed cell size based on a model by Gavrikov et al. [59]. There is a good agreement between the measured and theoretical cell sizes considering the high variability of the cell size measurements.

Cell patterns left on smoke foils by developed detonations were very irregular and showed secondary cell structures inside primary cells. Figures 4.8–4.10 show examples of experimental and computed cell patterns. There is a good agreement between the experimental and numerical results including the cell irregularity (Figure 4.8), secondary patterns inside main cells (Figure 4.9), and fine cell structures produced by transverse detonations (Figure 4.10).

The most important practical result of these experiments is the new extended range of detonability for methane-air mixtures observed in the large, 105 cm diameter tube. The new range, 5.3 to 15.5% CH<sub>4</sub>, almost encompasses the entire normal combustion limits of 5 to 16% methane in air as reported by Cashdollar et al. [136]. Figure 4.11 summarizes detonability limits measured for methane-air mixtures by different research groups in tubes of different diameters  $d$ , and using different detonation initiation methods. Matsui [114] used DDT with a Schelkin spiral, Wolanski et al. [109] used hydrogen-oxygen booster, Kogarko [108] used a high explosive, and Zipf et al. [14] used methane-oxygen booster. Most of the data fit nicely on a bell-shaped curve which shows wider limits for larger systems. Similar curves were obtained by Matsui [114] for other hydrocarbons and hydrogen.

Kuznetsov et al. [113] studied the flame acceleration in obstructed channels. Though detonations were not observed in these experiments, the boundary between subsonic and supersonic flames shown by cross points in Figure 4.11 is very close to the curve that represents detonability limits. This may imply that supersonic flames in obstructed channels partially rely on shock compression for an accelerated energy release. For mixtures that cannot detonate, the energy release does not accelerate enough in response to the shock compression, and therefore supersonic flames do not develop.

#### 4.3.2. DDT in NG-Air Mixtures

The initial series of DDT experiments in GETF show that detonations in 105 cm diameter tube can develop from a weak ignition source. When 9 or more baffles with blockage ratio BR=0.6 were installed at the beginning of the tube, detonations developed in the smooth section of the tube starting at about 50 m from the closed end. These detonations were identified using pressure and light sensors, and smoke foils the same way as in the direct initiation experiments. The mechanism of DDT in the smooth section is different from that in our simulations performed for the obstructed tube. The simulations predict that DDT will occur in the obstructed section at about 20 m, that is, with at least 20 baffles installed. So far, the experiments were carried out with up to 18 baffles, and produced detonations only in the smooth section, far from the obstructed area. The pressures at the end of the 18-baffle section were very high, indicating that several more baffles may initiate detonations in the obstructed section. These pressures lead to significant damage of the last several baffles. We expect that a new series of experiments with reinforced baffle mounts will show the DDT in the obstructed area.

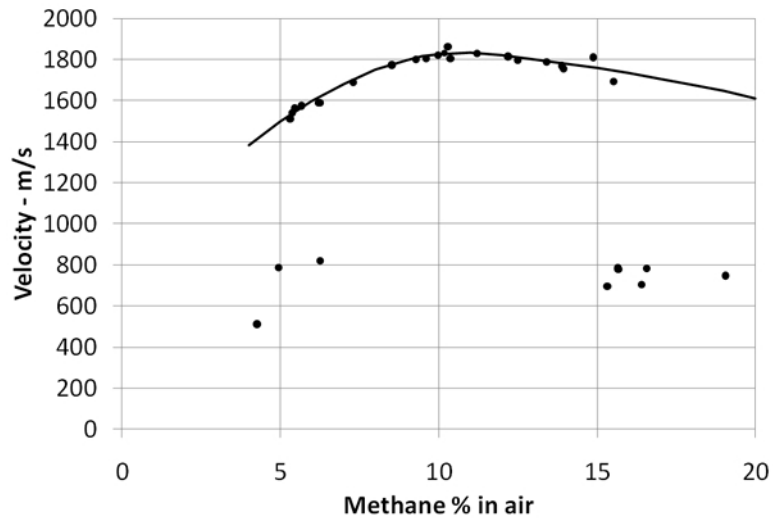


**Figure 4.5** Flame velocity measured in direct initiation experiments (points) as a function of mixture composition. Solid line shows computed CJ velocity.

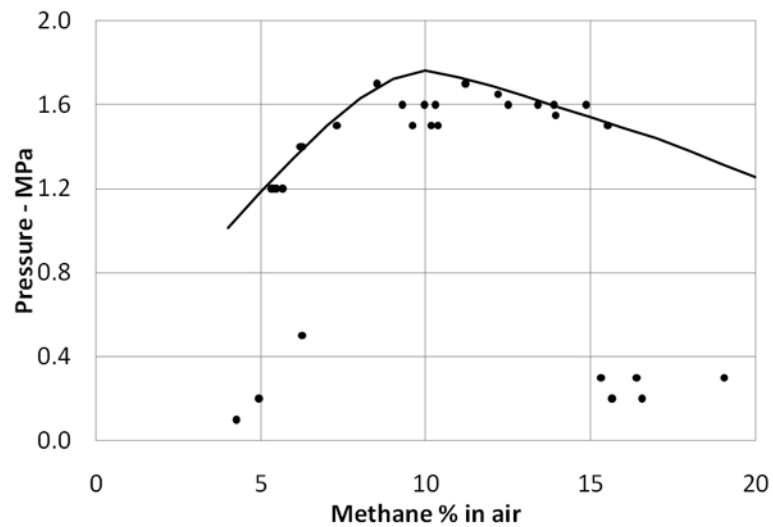


**Figure 4.6** Pressure measured behind the main peak in direct initiation experiments (points) as a function of mixture composition. Solid line shows computed CJ pressure.

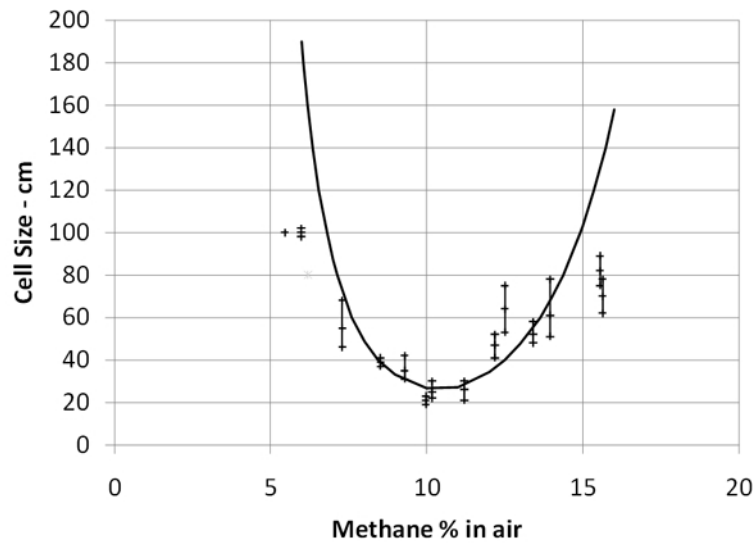


**Figure 4.7** Detonation cell size measured in direct initiation experiments. (low, high, and average data points). Solid line shows computed cell size based on a model by Gavrikov et al. [59].

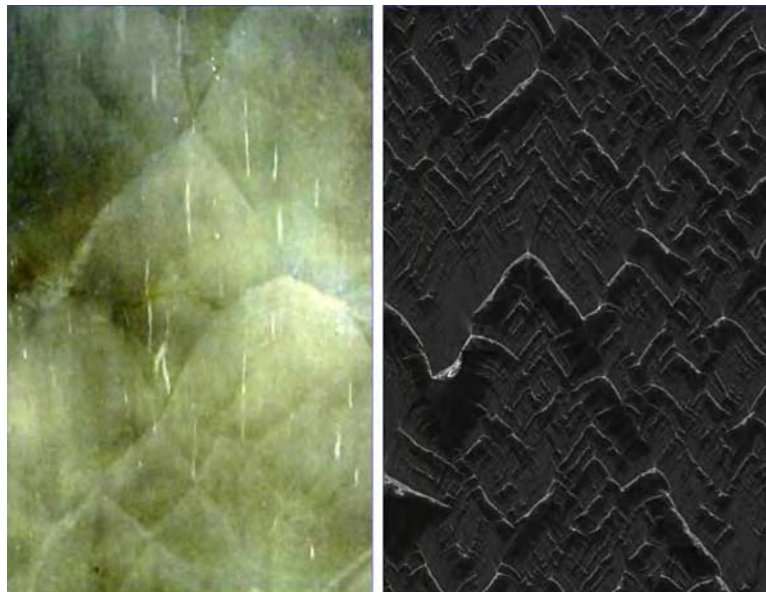


**Figure 4.8** Experimental (left) and computed (right) detonation cells. The fragment of experimental smoke foil is 25 cm wide and obtained for 10.4%  $\text{CH}_4$ .

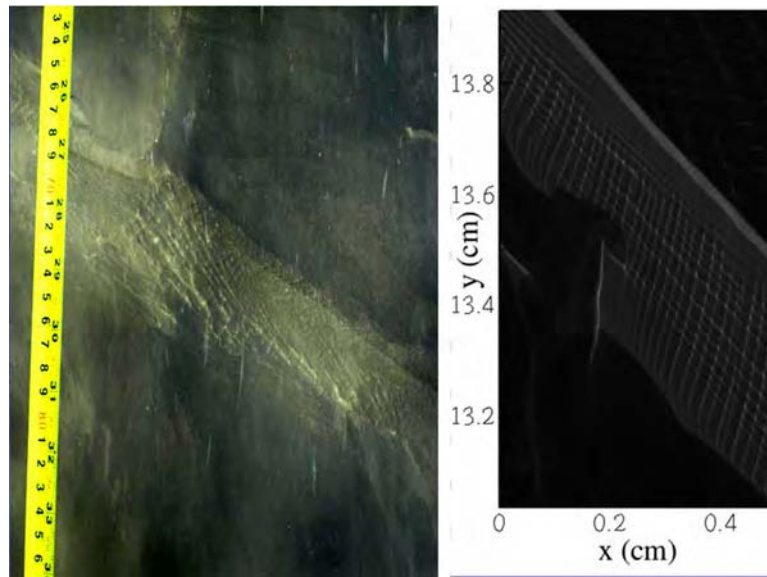


**Figure 4.9** Experimental (left) and computed (right) secondary detonation cells. The fragment of experimental smoke foil is 28 cm wide and obtained for 6.2%  $\text{CH}_4$ .



**Figure 4.10** Experimental (left) and computed (right) fine cellular structures produced by transverse detonations. The fragment of experimental smoke foil is 18 cm wide and obtained for 15.5%  $\text{CH}_4$ .

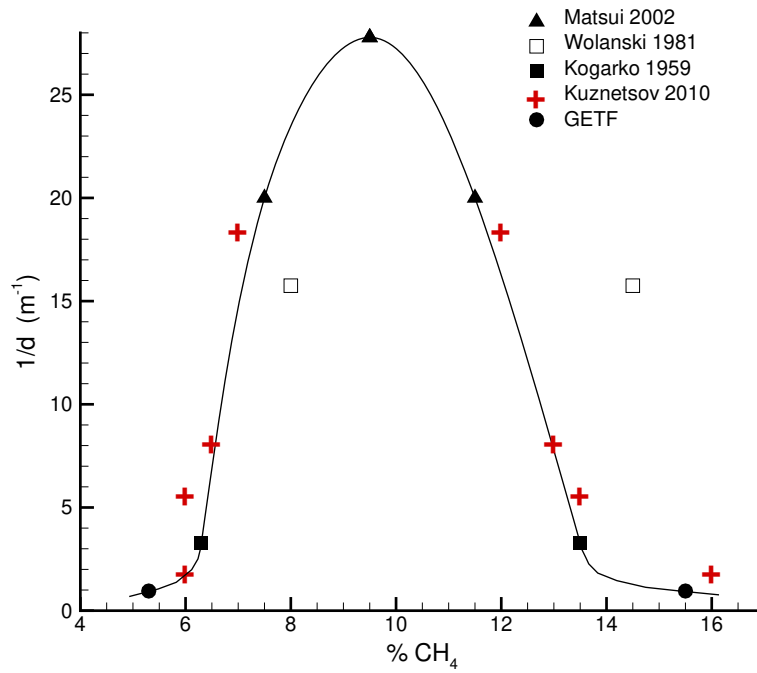


**Figure 4.11** Detonability limits measured for methane-air mixtures by different research groups in tubes of different diameters  $d$ . Solid line is the best fit for most of experimental points. Cross points show the boundary between subsonic and supersonic flames in obstructed channels.

## 5. Application to Coal Mining

Accidental gas explosions in underground coal mines generate pressures that can result in the loss of human life. To prevent these explosions, the operational area of mines are constantly ventilated to keep methane concentrations below the lower flammability limit. Unventilated, abandoned areas are usually sealed off with concrete walls (seals). The seals are designed to withstand explosion pressures if an accidental explosion occurs in a sealed area. It is, therefore, important to know the conditions under which explosions develop and the maximum pressures these explosions can generate.

The main objective of this work is to predict these maximum pressures. In particular, a detonation is considered as the worst-case explosion scenario, one that can generate extremely high pressures ranging from 1.2–1.7 MPa at the Chapman-Jouguet point (Figure 4.6) to 10 MPa at reflections. The ability of a mixture of a reactive gas and air to develop a detonation depends on several conditions that can be separated in two main groups.

The first group defines *absolute detonability*, which is the ability of a mixture to support a detonation in principle, no matter how this detonation is ignited. The conditions determining absolute detonability include the mixture composition, the background pressure and temperature, and the system size.

The second group defines *conditional detonability*, which is the ability of a mixture to develop a detonation for a particular geometry and ignition source. For weak ignition sources that do not initially involve strong shocks and detonations, conditional detonability is defined by the ability of a system to undergo a deflagration-to-detonation transition (DDT).

In the *Introduction* to this report, we asked an overriding question that is related both to the absolute detonability of the gas mixture and conditional detonability of the particular system:

*Given a large enough volume of a flammable mixture of NG and air, such as may exist in a coal mine, can a weak spark ignition develop into a detonation?*

First, we answer this overriding question in part: We have shown both computationally and experimentally that for systems at the coal mine scale, where tunnels measure up to 3 m high, 6 m wide and hundreds of meters long, detonation of methane-air mixtures is supportable across a range of compositions from 5.3 to 15.5 % methane in air. The least dimension of coal mine tunnels, the height, is usually greater than 1 m, and this dimension is much larger than the detonation cell size, which is about 20 cm for a stoichiometric mixture of methane in air. While it may require more energy and be more difficult to develop or initiate a detonation in methane-air mixtures near the detonation limits, it is possible to achieve this. Such detonations propagate in a stable manner as long as a detonable methane-air mixture is available.

Below we summarize the results of this study in terms of the absolute and conditional detonability, discuss DDT, and return with a more general answer to the overriding question.

### 5.1. Absolute Detonability

Direct initiation experiments at GETF have shown that NG-air mixtures containing between 5.3 and 15.5% of NG can detonate in a tube with a diameter of 105 cm. These detonability limits become narrower for smaller systems (Figure 4.11), and are likely to widen for larger systems. In particular, larger detonability limits are expected in coal mining tunnels, which can be up to 3 m high and 6 m wide.

As the system size increases, detonations are able to propagate in leaner and richer mixtures. Though the energy required for detonation initiation increases sharply for mixtures far from stoichiometric, the chemical energy available for the detonation initiation through DDT also increases with the system size. Even if the system geometry does not allow DDT near the detonation limits, systems with concentration gradients may develop detonations through DDT at some locations with near-stoichiometric concentrations. These detonations may then spread to lean or rich mixtures in other locations.

The importance of the observed wider detonability limits for larger systems goes well beyond large-scale explosions and coal mine applications. When detonability is concerned, the effect of a larger scale is often similar to the effect of a higher pressure, as recently shown in experiments [113]. In other words, we should expect wider detonability limits in small systems at elevated pressures. This means that the wider detonability limits should be applied to the design of engines that burn methane-air mixture at increased pressures.

## 5.2. Deflagration-to-Detonation Transition

Even if the mixture composition is within the detonability limits, it does not mean that a detonation will develop for a given geometry. Unconfined NG-air clouds, which might form when NG leaks from a vessel into the open air, are very unlikely to develop detonations from a weak ignition source. In this case, there is nothing to contain the pressure generated by the propagating flame or to generate strong turbulence. NG-air clouds in a coal mine are generally *not* unconfined, except perhaps for the smallest clouds that might form at an active face. In confined spaces, such as coal mine tunnels, detonations can develop more easily, especially when obstructions are present. DDT in NG-air mixtures was observed in smooth and obstructed channels of various diameters that range from 3.6 cm [114] to 105 cm (GETF experiments).

The important parameter characterizing the ability of a given mixture to develop a detonation in a given geometry is  $L_{DDT}$ , the run-up distance to DDT from the ignition source. This parameter is closely related to the minimum volume of reactive mixture required for the detonation development.

In smooth tubes, flames develop relatively slowly, especially when ignited by a weak spark without a pre-existing background turbulence. For methane-air mixtures, this type of ignition in smooth tubes produces a continuous flame acceleration, but DDT was not observed when the tube length was 30 m and the diameter was 40 cm [2], and in GETF experiments without obstacles for which the tube length is 73 m and the diameter is 105 cm. The observed continuous flame acceleration indicates that detonations would most likely appear in longer tubes, which means that  $L_{DDT}$  is greater than 30 m, for  $d = 40$  cm, and greater than 73 m for  $d = 105$  cm, but most likely finite.

The idealized case of a weak ignition in a straight smooth channel without turbulence is unlikely to occur in coal mines. Typical mine tunnels have very rough walls with crosscut openings to other tunnels, can be partially obstructed by rocks or mining equipment, and may have a pre-existing turbulence due to the forced ventilation. In these conditions, the flame developments would be significantly accelerated. Even in smooth channels, the flame evolution is accelerated if the ignition is more violent. This does not change the mechanism of flame acceleration and DDT, but accelerates the process by introducing initial turbulence.

For example, DDT in smooth tubes, or smooth sections of partially obstructed tubes was observed for a more violent flame ignition. In experiments [2], the gas was ignited by a turbulent flame jet generated by

combustion in a separate vessel connected to the main tube. In experiments [112], a high-speed flame jet was created by placing a series of obstructions (Shchelkin spiral) at the beginning of the tube. Obstructions (baffles) in GETF experiments played a similar role by promoting the flame acceleration to several hundred meters per second at the end of the obstructed section of the tube. For all three cases considered here, the flame development at the beginning of a smooth section starts from a fast turbulent flame jet. The subsequent flame development eventually leads to DDT, which occurs many tube diameters away from the beginning of the smooth section. The distances  $L_{DDT}$  measured from the beginning of the smooth section are shown by open points in Figure 5.1 and approximated by line 1 as a function of tube diameter  $d$ .

For obstructed tubes (line 2), the initial flame is ignited by a spark near the closed end of the tube, and propagates through a series of obstructions until DDT occurs. So far, there are only two experimental data points obtained by Kuznetsov [72] for the blockage ratio  $BR=0.3$  and the distance between obstacles  $S = d$ . Our numerical simulations for the same parameters and  $d = 1.05$  m give  $L_{DDT}/d = 17$ .

Figure 5.1 shows that the presence of multiple obstructions may reduce  $L_{DDT}$  by several times. A rough extrapolation to  $d = 3$  m (which approximately corresponds to the mining tunnel size) gives  $L_{DDT}/d \sim 30$  for smooth tunnels with violent initiation, and  $\sim 10$  for obstructed tunnels with weak spark ignition. In realistic mine conditions, a violent initiation may occur, for example, if the flame is ignited and accelerated in a heavily obstructed area, and then enters a relatively smooth tunnel.

These estimations are valid for simple geometries and uniform obstacle spacing at  $S = d$ . Changing  $S$  may reduce  $L_{DDT}/d$ . For example, the computations performed for  $BR = 0.3$  and  $d = 105$  cm give  $L_{DDT}/d = 20$  for  $S = d$  and  $L_{DDT}/d = 13$  for  $S = d/2$ . Complex geometries, such as crosscut tunnels, rough walls, mining equipment, or partially collapsed areas can further reduce  $L_{DDT}$ .

Now we return to answer the overriding question of whether DDT can arise in coal-mine conditions. We have shown both computationally and experimentally that it is possible for a detonation to develop from a weak spark for certain NG-air mixtures in certain experimental conditions. Theoretically and computationally, it appears that DDT will develop in obstructed and smooth tubes over a range of NG air compositions. Preliminary data from GETF experiments verify that DDT is achievable in obstructed tubes with a diameter of 1 m. By all indicators in Figure 5.1, these results will extend to the coal mine scale where tunnels measure up to 3 m high, 6 m wide, and are hundreds of meters long.

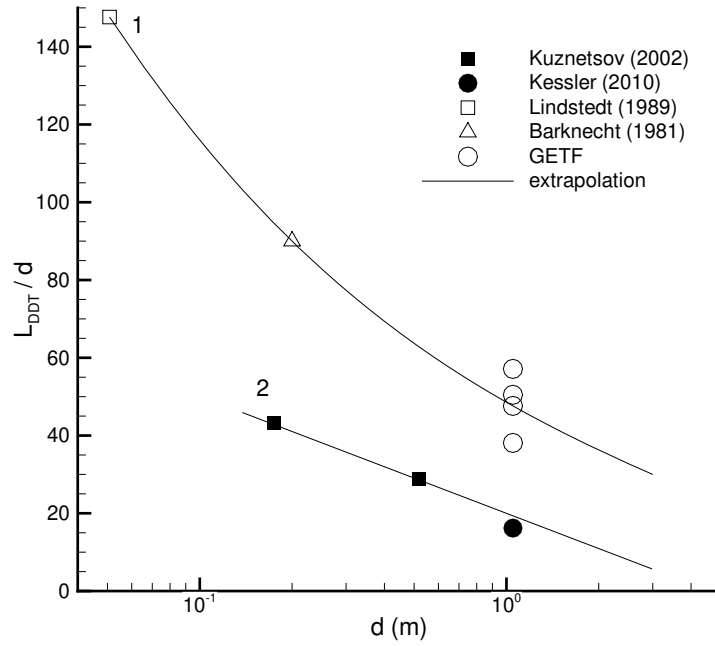


**Figure 5.1** Run-up distance to DDT  $L_{DDT}$  as a function tube diameter measured or computed by different research groups in smooth (1) or obstructed (2) tubes of different diameters  $d$ . GETF data (open circles) are obtained in experiments with 9, 10, or 11 baffles placed near the closed end of the tube and uniformly spaced at  $S = d = 1.05$  m.  $L_{DDT}$  is measured from the last baffle. Cross points show a rough extrapolation to the scale of a typical coal mine tunnel.

## 6. Future Work

This report describes the NRL research efforts to answer the fundamental safety question: *Given a large enough volume of a flammable mixture of NG and air, such as may exist in a coal mine, can a weak spark ignition develop into a detonation?* The completion of the four specific tasks performed to address this question has made substantial progress towards providing an answer.

1. Computations that solved the reactive Navier-Stokes equations applied to DDT in stoichiometric methane-air mixtures showed that it is possible to calculate the complex fluid dynamics of reactive flows in obstructed channels and simulate, from first principles, the development of DDT. Many of the physical events that lead to DDT can now be calculated and are well understood. Furthermore, the simulations agree well with experiments both in the published literature and recently available with the GETF.
2. The mechanics of DDT in methane-air mixtures contain a probabilistic element connected with the complexity and inherent randomness of fluid turbulence, the appearance of hot spots from which detonations develop, and other features of combustion processes. The computations can replicate the stochasticity of the DDT process and the variability within experimental observations of DDT. (See Section 3.2.2c of this report.)
3. Combustion processes leading to DDT in fuel-lean and fuel-rich methane-air mixtures can be computed by solving the reactive Navier-Stokes equation. The results of these computations agree well with experimental observations indicating that we have an excellent fundamental understanding of the processes.
4. Computational models have been developed and tested for simplified detonation problems for methane-air mixtures with concentration gradients.

Recent experimental work by NIOSH, performed in conjunction with theoretical and computational work performed by NRL has extended the known detonability limits for methane-air mixtures to the 5.3 to 15.5% range. DDT has been achieved in the 105 cm diameter tube.

The work completed so far by NRL, which was performed in conjunction with recent experimental work by NIOSH, has made substantial progress toward answering the fundamental underpinning question about DDT stated above. We have *not yet* proved conclusively that substantial accumulations of NG and air in coal mine tunnels could develop into detonation when ignited by a weak spark. We are, however, very close to providing a definitive, scientifically sound answer to this vexing question.

In order to be able to make the definitive statement on DDT in coal mines, we need to solve three critical problems. We have to be able to:

(1) Ensure that numerical models calibrated on small-scale experiments with obstructed channels will give the correct scaling when used for larger geometries typical of coal mine tunnels. This will require the model validation using GETF data (GETF experiments have not yet shown DDT in the obstructed section of the tube), and possibly performing large-scale experiments in LLEM tunnels.

(2) Understand and predict the flame behavior, DDT, and detonation propagation in mixtures with spatially nonuniform compositions that are likely to form in real-life configurations. Such nonuniform com-

positions may form, for example, when layers of methane accumulate at the top of a horizontal tunnel without completely mixing with air. Solving this problem is within capabilities of the current numerical models.

(3) Understand the mechanism of DDT in a smooth section of a channel. *This is one of the key unresolved problems in combustion.* This type of DDT is observed in GETF experiments, but is not reproduced by the current models. Addressing this question will require a development of more sophisticated numerical models, possibly with a detained resolution of boundary layers, and a detailed analysis of GETF results, possibly involving additions diagnostics.

An extended NRL and NIOSH effort would aim to produce the definitive peer-reviewed technical papers on methane-air detonation and DDT applied to coal mines.

## **Acknowledgments**

We would like to especially thank R.K. Zipf for his many critical suggestions and stimulating conversations. We also thank R.K. Zipf, M.J. Sapko, W.P. Marchewka, K.M. Mohamed, E.S. Weiss, J.D. Addis, F.A. Karnack, and D.D. Sellers for their dedicated work to develop the GETF facility and experiments. Computer resources were provided by the Department of Defense High Performance Computing Modernization Program. We thank Y. Sarrazin, S.B. Dorofeev, J.E. Shepherd, and A.Yu. Starikovskiy for their invaluable suggestions that helped with the design of the GETF facility end experiments. We thank F.A. Williams, D. Bradley, F. Schauer, and M. Kuznetsov for valuable discussions.

## References

- [1] R.K. Zipf, M.J. Sapko, J.F. Brune, *Explosion Pressure Design Criteria for New Seals in U.S. Coal Mines*, IC-9500, NIOSH, July 2007.
- [2] W. Bartknecht, *Explosion*, Berlin, Germany: Springer-Verlag; 1981.
- [3] D.M. Johnson, “The potential for vapour cloud explosions—Lessons from the Buncefield accident,” *Journal of Loss Prevention in the Process Industries* in press, doi:10.1016/j.jlp.2010.06.011.
- [4] G.W. McMahon, J.R. Britt, J.L. O’Daniel, *CFD Study and Structural Analysis of the Sago Mine Accident*, Technical Report, US Army Corps of Engineers, Engineer Research and Development Center, Geotechnical and Structures Laboratory, May 2007.
- [5] E.S. Oran, V.N. Gamezo, “Origins of the deflagration-to-detonation transition in gas-phase combustion,” *Combustion and Flame* 148 (2007) 4–47.
- [6] V.N. Gamezo, T. Ogawa, E.S. Oran, “Flame acceleration and DDT in channels with obstacles: Effect of obstacle spacing,” *Combustion and Flame* 155 (2008) 302–315.
- [7] V.N. Gamezo, T. Ogawa, E.S. Oran, “Numerical simulations of flame propagation and DDT in obstructed channels filled with hydrogen-air mixture,” *Proceedings of the Combustion Institute* 31 (2007) 2463–2471.
- [8] T. Ogawa, V.N. Gamezo, E.S. Oran, “Flame acceleration and transition to detonation in an array of square obstacles,” Proceedings of Eighth International Symposium on Hazards, Prevention, and Mitigation of Industrial Explosions, Yokohama, Japan, Sept. 5-10, 2010.
- [9] D.A. Kessler, V.N. Gamezo, E.S. Oran, “Simulations of flame acceleration and deflagration-to-detonation transitions in methane-air systems,” *Combustion and Flame* 157 (2010) 2063–2077.
- [10] D.A. Kessler, V.N. Gamezo, E.S. Oran, “Multilevel detonation cell structures in methane-air mixtures,” *Proceedings of the Combustion Institute*, to appear (doi:10.1016/j.proci.2010.07.071), 2011.
- [11] D.A. Kessler, V.N. Gamezo, E.S. Oran, “Simulations of flame acceleration and deflagration-to-detonation transitions in large-scale methane-air mixtures,” Eastern States Section Meeting of the Combustion Institute, College Park, MD, Oct. 2009.
- [12] D.A. Kessler, V.N. Gamezo, E.S. Oran, “Simulation of deflagration-to-detonation transition in premixed CH<sub>4</sub>-air in large-scale channels,” AIAA Paper 2009-439, 47th AIAA Aerospace Sciences Meeting, Orlando, FL, Jan. 2009.
- [13] D.A. Kessler, V.N. Gamezo, E.S. Oran, “Flame acceleration and deflagration-to-detonation transitions of stoichiometric, lean, and rich methane-air mixtures in obstructed channels,” Proceedings of the 6th U.S. National Combustion Meeting, Ann Arbor, MI, May 2009.
- [14] R.K. Zipf Jr., V.N. Gamezo, M.J. Sapko, W.P. Marchewka, K.M. Mohamed, E.S. Oran, D.A. Kessler, E.S. Weiss, J.D. Addis, F.A. Karnack, D.D. Sellers, “Methane-Air Detonation Experiments at NIOSH Lake Lynn Laboratory.” Proceedings of Eighth International Symposium on Hazards, Prevention, and Mitigation of Industrial Explosions, Yokohama, Japan, Sept. 5-10, 2010.
- [15] E.S. Oran, J.P. Boris, *Numerical Simulation of Reactive Flow*, Second Edition, New York: Cambridge University Press, 2001.
- [16] E.S. Oran, J.P. Boris, *Numerical Simulation of Reactive Flow*, First Edition, New York: Cambridge University Press, 1987.
- [17] J. von Neumann, R.D. Richtmyer, “A method for the numerical calculation of hydrodynamic shocks,” *Journal of Applied Physics* 21 (1950) 232–257.
- [18] D. Potter, *Computational Physics*, New York: Wiley, 1973.
- [19] J.P. Boris, D.L. Book, “Flux-corrected transport I: SHASTA—A fluid transport algorithm that works,” *Journal of Computational Physics* 11 (1973) 38–69.

- [20] C.R. Devore, “Flux-corrected transport for multidimensional compressible magnetohydrodynamics,” *Journal of Computational Physics* 92 (1991) 142–160.
- [21] J.P. Boris, “On large eddy simulations using subgrid turbulence models.” In *Wither turbulence? Turbulence at the crossroads*, ed. J.L. Lumley, *Lecture Notes in Physics* 257 (1989) 344–353, Berlin: Springer-Verlag.
- [22] F.F. Grinstein, L.G. Margolin, W.J. Rider, *Implicit Large Eddy Simulation*, New York: Cambridge University Press, 2007.
- [23] M.J. Berger, J. Olinger, “Adaptive mesh refinement for hyperbolic partial differential equations,” *Journal of Computational Physics* 53 (1984) 484–512.
- [24] M.J. Berger, P. Colella, “Local adaptive mesh refinement for shock hydrodynamics,” *Journal of Computational Physics* 82 (1989) 64–84.
- [25] S.B. Pope, *Turbulent Flows*, Cambridge, UK: Cambridge University Press, 2000.
- [26] C.J. Lea, H.S. Ledin, *A review of the state of the art in gas explosion modeling*, Buxton, U.K.: Health & Safety Laboratory Report HSL/2002/02, 2002.
- [27] N.R. Popat, C.A. Catlin, B.J. Arntzen, R.P. Lindstedt, B.H. Hjertager, T. Solberg, “Investigations to improve and assess the accuracy of computational fluid dynamic-based explosion models,” *Journal of Hazardous Materials* 45 (1996) 1–25.
- [28] J.R. Bakke, *Numerical simulation of gas explosions in two-dimensional geometries*, Ph.D. Thesis, Faculty of Mathematics and Natural Sciences, University of Bergen, 1986.
- [29] Gexcon US, inc. <http://www.gexconus.com/index.cfm?id=217344>
- [30] A.C. Van den Berg, *REAGAS—A code for numerical simulation of reactive gas dynamics in gas explosions*, Report No. PML 1989-IN48, TNO Prins Maurits Laboratory, 1989.
- [31] M. Gittings, et al., *SAGE Users Manual*, LA-R-04-2959, Los Alamos National Laboratory.
- [32] G.W. McMahon, J.R. Britt, R.E. Walker, “Methane explosion modeling in the Sago Mine,” *Mining Engineering* July (2010) 51–62.
- [33] G. Tsatsaronis, “Prediction of propagating laminar flames in methane, oxygen, nitrogen mixtures,” *Combustion and Flame* 33 (1978) 217–239.
- [34] J.R. Bakke, *Gas explosion simulation in Piper Alpha module C using FLACS*, Lord Cullen’s Public Inquiry, 1989, unpublished.
- [35] D.D. Drysdale, R. Sylvester-Evans, “The explosion and fire on the Piper Alpha platform, 6 July 1988. A case study,” *Philosophical Transactions of the Royal Society of London A* 356 (1998) 2929–2951.
- [36] E.J. Draper, G.E. Fairlie, *AutoReaGas modeling of gas explosions in mines*, report prepared by Century Dynamics Ltd. for NIOSH, 2006.
- [37] O.R. Hansen, *FLACS modeling for NIOSH: simulations of existing and planned tests at Lake Lynn experimental mines*, report prepared by Christian Michelsen Research AS for NIOSH, 2006, unpublished.
- [38] E.S. Oran, J.H. Gardner, “Chemical acoustic interactions in combustion systems,” *Progress in Energy and Combustion Science* 11 (1985) 253–276.
- [39] T. Scarinci, J.H. Lee, G.O. Thomas, R. Bambrey, D.H. Edwards, “Amplification of a pressure wave by its passage through a flame front,” *Progress in Astronautics and Aeronautics* 152 (1993) 3–24.
- [40] Ya.B. Zeldovich, V.B. Librovich, G.M. Makhviladze, G.I. Sivashinsky, “On the development of detonation in a nonuniformly heated gas,” *Astronautica Acta* 15 (1970) 313–321.
- [41] A.M. Khokhlov, E.S. Oran, G.O. Thomas, “Numerical simulation of deflagration-to-detonation transition: The role of shock-flame interactions in turbulent flames,” *Combustion and Flame* 117 (1999) 323–339.
- [42] A.M. Khokhlov, E.S. Oran, A.Yu. Chtchelkanova, J.C. Wheeler, “Interaction of a shock with a sinusoidally perturbed flame,” *Combustion and Flame* 117 (1999) 99–116.

- [43] A.M. Khokhlov, E.S. Oran, “Numerical simulation of detonation initiation in a flame brush: The role of hot spots,” *Combustion and Flame* 119 (1999) 400–416.
- [44] V.N. Gamezo, A.M. Khokhlov, E.S. Oran, “The influence of shock bifurcations on shock-flame interactions and DDT,” *Combustion and Flame* 126 (2001) 1810–1826.
- [45] V.N. Gamezo, A.M. Khokhlov, E.S. Oran, “Effects of wakes on shock-flame interactions and deflagration-to-detonation transition,” *Proceedings of the Combustion Institute* 29 (2002) 2803–2808.
- [46] V.N. Gamezo, E.S. Oran, A.M. Khokhlov, “Three-dimensional reactive shock bifurcations,” *Proceedings of the Combustion Institute* 30 (2005) 1841–1847.
- [47] G. Thomas, G. Oakley, R. Bambrey, “An experimental study of flame acceleration and deflagration transition in representative process piping,” *Process Safety and Environmental Protection* 88 (2010) 75–90.
- [48] A. Teodorczyk, P. Drobniak, A. Dabkowski, “Fast turbulent deflagration and DDT of hydrogen-air mixtures in small obstructed channel,” *International Journal of Hydrogen Energy* 34 (2009) 5887–5893.
- [49] V.N. Gamezo, T. Ogawa, E.S. Oran, “Deflagration-to-detonation transition in premixed H<sub>2</sub>-air in channels with obstacles,” 45th AIAA Aerospace Sciences Meeting, Reno, NV, 2007.
- [50] E.S. Oran, J.P. Boris, T. Young, M. Flanigan, T. Burks, T. Picone, “Numerical simulations of detonations in hydrogen-air and methane-air mixtures,” *Proceedings of the Combustion Institute* 18 (1981) 1641–1649.
- [51] C.K. Westbrook, F.L. Dryer, “Simplified reaction mechanisms for the oxidation of hydrocarbon fuels in flames,” *Combustion Science & Technology* 27 (1981) 31–43.
- [52] J.W. Dold, A.K. Kapila, “Comparison between shock initiations of detonation using thermally-sensitive and chain-branching chemical models,” *Combustion and Flame* 85 (1991) 185–194.
- [53] D.J. Hautman, F.L. Dryer, K.P. Schug, I. Glassman, “A multi-step overall kinetic mechanism for the oxidation of hydrocarbons,” *Combustion Science & Technology* 25 (1981) 219–235.
- [54] W.P. Jones, R.P. Lindstedt, “Global reaction schemes for hydrocarbon combustion,” *Combustion and Flame* 73 (1988) 233–249.
- [55] E.S. Oran, A.M. Khokhlov, “Deflagrations, hot spots, and the transition to detonation,” *Philosophical Transactions of the Royal Society of London A* 357 (1999) 3539–3551.
- [56] V.N. Gamezo, T. Ogawa, E.S. Oran, “Deflagration-to-detonation transition in H<sub>2</sub>-air mixtures: Effect of blockage ratio,” AIAA Paper 2009-440, 47th AIAA Aerospace Sciences Meeting and Exhibit, Orlando, FL, Jan. 2009.
- [57] G.E. Andrews, D. Bradley, “The burning velocity of methane-air mixtures,” *Combustion and Flame* 19 (1972) 275–288.
- [58] G.E. Andrews, D. Bradley, “Determination of burning velocity by double ignition in a closed vessel,” *Combustion and Flame* 20 (1973) 77–89.
- [59] A.I. Gavrikov, A.A. Efimenko, S.B. Dorofeev, “Detonation cell size predictions from detailed chemical kinetic calculations,” *Combustion and Flame* 120 (2000) 19–33.
- [60] O. Peraldi, R. Knystautas, J.H. Lee, “Criteria for transition to detonation in tubes,” *Proceedings of the Combustion Institute* 22 (1986) 1629–1637.
- [61] A. Vesper, W. Breitung, S.B. Dorofeev, “Run-up distances to supersonic flames in obstacle-laden tubes,” *Journal de Physique IV* 12 (2002) 333–340.
- [62] W. Breitung, S. Dorofeev, A. Kotchourko, R. Redlinger, W. Scholtyssek, “Integral large scale experiments on hydrogen combustion for severe accident code validation-HYCOM,” *Nuclear Engineering and Design* 235 (2005) 253–270.
- [63] R. Knystautas, J.H.S. Lee, J.E. Shepherd, A. Teodorczyk, “Flame acceleration and transition to detonation in benzene-air mixtures,” *Combustion and Flame* 115 (1998) 424–436.

- [64] A. Teodorczyk, J.H.S. Lee, R. Knystautas, "Propagation mechanism of quasi-detonations," *Proceedings of the Combustion Institute* 22 (1988) 1723–1731.
- [65] A. Teodorczyk, J.H.S. Lee, R. Knystautas, "Photographic study of the structure and propagation mechanisms of quasi-detonations in rough tubes," *Progress in Astronautics and Aeronautics* 133 (1990) 233–240.
- [66] A. Teodorczyk, "Fast deflagrations and detonations in obstacle-filled channels," *Biul. Inst. Tech. Ciepl. Politech. Warsz.* 79 (1995) 145–178.
- [67] M.S. Kuznetsov, V.I. Alekseev, S.B. Dorofeev, "Comparison of critical conditions for DDT in regular and irregular cellular detonation systems," *Shock Waves* 10 (2000) 217–223.
- [68] S.B. Dorofeev, M.S. Kuznetsov, V.I. Alekseev, A.A. Efimenko, W. Breitung, "Evaluation of limits for effective flame acceleration in hydrogen mixtures," *Journal of Loss Prevention in the Process Industries* 14 (2001) 583–589.
- [69] V.I. Alekseev, M.S. Kuznetsov, Y.G. Yankin, S.B. Dorofeev, "Experimental study of flame acceleration and the deflagration-to-detonation transition under conditions of transverse venting," *Journal of Loss Prevention in the Process Industries* 14 (2001) 591–596.
- [70] S.B. Dorofeev, "Flame acceleration and DDT in gas explosions," *Journal de Physique IV* 12 (2002) Pr7-3–10.
- [71] M.S. Kuznetsov, V.I. Alekseev, Y.G. Yankin, S.B. Dorofeev, "Slow and fast deflagrations in hydrocarbon-air mixtures," *Combustion Science & Technology* 174 (2002) 157–172.
- [72] M. Kuznetsov, G. Ciccarelli, S. Dorofeev, V. Alekseev, Yu. Yankin, T.H. Kim, "DDT in methane-air mixtures," *Shock Waves* 12 (2002) 215–220.
- [73] S. Gordon and B.J. McBride, *Computer Program for Calculation of Complex Chemical Equilibrium Composition, Rocket Performance, Incident and Reflected Shocks and Chapman-Jouguet Detonation*, NASA Report SP-273, 1971.
- [74] A.M. Khokhlov, "Fully threaded tree for adaptive mesh fluid dynamics simulations," *Journal of Computational Physics* 143 (1998) 519–543.
- [75] J.E. Shepherd, "Detonation in gases," *Proc. Combust. Inst.* 32 (2009) 83–98.
- [76] M.-O. Sturtzer, N. Lamoureux, C. Matignon, D. Desbordes, H.-N. Presles, "On the origin of the double cellular structure of the detonation in gaseous nitromethane and its mixtures with oxygen," *Shock Waves* 14 (2005) 45–51.
- [77] D. Desbordes, F. Joubert, F. Virost, B. Khasainov, H.-N. Presles, "The critical tube diameter in a two reaction steps detonation: the  $H_2/NO_2$  mixture case," *Shock Waves* 18 (2008) 269–276.
- [78] V.I. Manzhalei, "On the fine structure of gaseous detonation front," *Fizika Goreniya i Vzryva* 13 (1977) 470–472.
- [79] V.N. Gamezo, A.M. Khokhlov, E.S. Oran, "Secondary Detonation Cells in Systems with High Activation Energy," Proceedings of the 17th ICDERS, 1999, paper 237.
- [80] V.N. Gamezo, A.A. Vasil'ev, A.M. Khokhlov, E.S. Oran, "Fine cellular structures produced by marginal detonations," *Proceedings of the Combustion Institute* 28 (2000) 611–617.
- [81] A.M. Khokhlov, J. Austin, F. Pintgen, J. Shepherd, "Numerical Study of the Detonation Wave Structure in Ethylene-Oxygen Mixtures," AIAA Paper 2004-0792, 42nd AIAA Aerospace Sciences Meeting, Reno, NV, Jan. 2004.
- [82] C.T. Johansen, G. Ciccarelli, "Visualization of the unburned gas flow field ahead of an accelerating flame in an obstructed square channel," *Combustion and Flame* 156 (2009) 405–416.
- [83] A.E. Lutz, R.J. Kee, J.A. Miller, H.A. Dwyer, A.K. Oppenheim, "Dynamic effects of auto-ignition centers for hydrogen and  $C_{1,2}$ -hydrocarbon fuels," *Proceedings of the Combustion Institute* 22 (1989) 1683–1693.

- [84] X.J. Gu, D.R. Emerson, D. Bradley, “Modes of reaction front propagation from hot spots,” *Combustion and Flame* 133 (2003) 63–74.
- [85] K. Kailasanath, E. Oran, J. Boris, “A Theoretical Study of the Ignition of Premixed Gases.” *Combustion and Flame* 47 (1982) 173–190.
- [86] G.O. Thomas, P. Sutton, D.H. Edwards, “The behavior of detonation waves at concentration gradients,” *Combustion and Flame* 84 (1991) 312–322.
- [87] M.S. Kuznetsov, V.I. Alekseev, S.B. Dorofeev, I.D. Matsukov, J.L. Boccio JL, “Detonation propagation, decay, and reinitiation in nonuniform gaseous mixtures,” *Proceedings of the Combustion Institute* 27 (1998) 2241–2247.
- [88] I. Sochet, T. Lamy, J. Brossard, “Experimental investigation on the detonability of non-uniform mixtures,” *Shock Waves* 10 (2000) 363–367.
- [89] K. Ishii, M. Kojima, “Behavior of detonation propagation in mixtures with concentration gradients,” *Shock Waves* 17 (2007) 95–102.
- [90] D.H. Lieberman, J.E. Shepherd, “Detonation interaction with a diffuse interface and subsequent chemical reaction,” *Shock Waves* 16 (2007) 421–429.
- [91] W.H. Calhoun, Jr. N. Sinha, “Detonation wave propagation in concentration gradient,” AIAA Paper 2005-1167, 43rd AIAA Aerospace Sciences Meeting, Reno, NV, Jan. 2005.
- [92] J. Dold, “Flame propagation in a nonuniform mixture—Analysis of a slowly varying triple flame,” *Combustion and Flame* 76 (1989) 71–88.
- [93] P. Kioni, B. Rogg, K. Bray, A. Liñán, “Flame spread in laminar mixing layers—the triple flame,” *Combustion and Flame* 95 (1993) 276–290.
- [94] E. Fernández-Tarrazo, A.L. Sánchez, A. Liñán, F.A. Williams, “A simple one-step chemistry model for partially premixed hydrocarbon combustion.” *Combustion and Flame* 147 (2006) 32–38.
- [95] E. Fernández-Tarrazo, M. Vera, and A. Liñán, “Liftoff and blowoff of a diffusion flame between parallel streams of fuel and air.” *Combustion and Flame* 144 (2006) 261–276.
- [96] L.J. Spadaccini, M.B. Colket III, “Ignition delay characteristics of methane fuels,” *Progress in Energy and Combustion Science* 20 (1994) 431–460.
- [97] N. Lamoureux, C.-E. Paillard, “Natural gas ignition delay times behind reflected shock waves: Application to modelling and safety,” *Shock Waves* 13 (2003) 57–68.
- [98] A.G. Kim, *The composition of coalbed gas*, U.S. Department of the Interior, Bureau of Mines, RI 7762, NTIS No. PB221574, 1973.
- [99] M.A. Trevits, G.L. Finfinger, “Coalbed gas: An analysis of the relationship between gas content, gas composition, and mine emissions,” *Proceedings of the Fourth U.S. Mine Ventilation Symposium, SME-AIME*, 1989, 519–524.
- [100] C.K. Westbrook, W.J. Pitz, “Effects of propane on ignition of methane-ethane-air mixtures,” *Combustion Science and Technology* 33 (1983) 315–319.
- [101] R. Vander Molen, J.A. Nicholls, “Blast wave initiation energy for the detonation of methane-ethane-air mixtures,” *Combustion Science and Technology* 21 (1979) 75–78.
- [102] J.A. Nicholls, M. Sichel, Z. Gabrijel, R.D. Oza, R. Vander Molen, “Detonability of unconfined natural gas-air clouds,” *Proceedings of the Combustion Institute* 17 (1979) 1223–1234.
- [103] S.M. Kogarko, V.V. Aduahkin, A.G. Lyamin, “Investigation of spherical detonation of gas mixtures,” *Combustion, Explosion, and Shock Waves* 1 (1965) 15–22.
- [104] D.C. Bull, J.E. Elsworth, G. Hooper, C.P. Quinn, “A study of spherical detonation in mixtures of methane and oxygen diluted by nitrogen,” *Journal of Physics D: Applied Physics* 9 (1976) 1991–2000.
- [105] E.B. Vanta, J.C. Foster, G.H. Parsons, *Detonability of some natural gas-air mixtures*, Air Force Armament Laboratory, Eglin. AFB, FL, Report AFATL-TR-74-80, 1974.

- [106] M.C. Parnarouskis, C.D. Lind, P.P.K. Raj, J.M. Cece, "Vapor cloud explosion study," Proceedings of the 6th International Conference on Liquefied Natural Gas, Vol. 2, Session III, paper 12, Kyoto, 1980.
- [107] W. Payman, W.C.F. Shepherd, "Explosion waves and shock waves IV. Quasi-detonation in mixtures of methane and air," *Proceedings of the Royal Society of London A* 158 (1937) 348–367.
- [108] S. M. Kogarko, "Detonation of methane-air mixtures and the detonation limits of hydrocarbon-air mixtures in a large-diameter pipe," *Soviet Physics - Technical Physics* 3 (1959) 1904–1916.
- [109] P. Wolanski, C.W. Kauffman, M. Sichel, J.A. Nicholls, "Detonation of methane-air mixtures," *Proceedings of the Combustion Institute* 18 (1981) 1651–1660.
- [110] I.O. Moen, J.W. Funk, S.A. Ward, G.M. Rude, and P.A. Thibault, "Detonation length scales for fuel-air explosives," *Progress in Astronautics and Aeronautics* 94 (1984) 55–79.
- [111] M. Gerstein, E.D. Carlson, F.U. Hill, "Natural gas-air explosions at reduced pressures," *Industrial and Engineering Chemistry* 46 (1954) 2558–2562.
- [112] R.P. Lindstedt, H.J. Michels, "Deflagration to detonation transitions and strong deflagrations in alkane and alkene air mixtures," *Combustion and Flame* 76 (1989) 169–181.
- [113] M. Kuznetsov, V. Alekseev, I. Matsukov, T.H. Kim, "Ignition, flame acceleration and detonations of methane-air mixtures at different pressures and temperatures," Proceedings of 8th International Symposium on Hazards, Prevention, and Mitigation of Industrial Explosions, Yokohama, Japan, Sept. 2010, paper ISH-118.
- [114] H. Matsui, "Detonation propagation limits in homogeneous and heterogeneous systems," *Journal de Physique IV* 12 (2002) Pr7-11–17.
- [115] P. Urtiew, A.K. Oppenheim, "Experimental observations of the transition to detonation in an explosive gas," *Proceedings of the Royal Society of London A* 295 (1966) 13–28.
- [116] M. Kuznetsov, V. Alekseev, I. Matsukov, S. Dorofeev, "DDT in a smooth tube filled with a hydrogen-oxygen mixture," *Shock Waves* 14 (2005) 205–215.
- [117] M. Kuznetsov, M. Liberman, I. Matsukov, "Experimental study of the preheat zone formation and deflagration to detonation transition," *Combustion Science and Technology* 182 (2010) 1628–1644.
- [118] G.H. Markstein, *Nonsteady Flame Propagation*, New York: MacMillan, 1964, Chapter D.
- [119] T. Scarinci, G.O. Thomas, *Some Experiments on Shock-Flame Interactions*, Department of Physics, University of Wales, Report Number UCW/det905, Aberystwyth, Wales, UK, 1990.
- [120] G.O. Thomas, C.J. Sands, R.J. Bambrey, S.A. Jones, "Experimental observations of the onset of turbulent combustion following a shock-flame interaction," Proceedings of the 16th ICDERS, 1997, 2–5.
- [121] G.O. Thomas, R. Bambrey, C. Brown, "Experimental observations of flame acceleration and transition to detonation following shock-flame interaction," *Combustion Theory and Modelling* 5 (2001) 573–594.
- [122] W.R. Chapman, R.V. Wheeler, "The propagation of flame in mixtures of methane and air, Part IV. The effect of restrictions in the path of the flame," *Journal of the Chemical Society (Resumed)* (1926) 2139–2147.
- [123] H. Robinson, R.V. Wheeler, "Explosions of methane and air - propagation through a restricted tube," *Journal of the Chemical Society (Resumed)* (1933) 758–760.
- [124] J.H. Lee, R. Knystautas, C.K. Chan, "Turbulent flame propagation in obstacle-filled tubes," *Proceedings of the Combustion Institute* 20 (1984) 1663–1672.
- [125] Y.K. Liu, J.H. Lee, R. Knystautas, "Effect of geometry on the transmission of detonation through an orifice," *Combustion and Flame* 56 (1984) 215–225.
- [126] G. Ciccarelli, S.B. Dorofeev, "Flame acceleration and transition to detonation in ducts," *Progress in Energy and Combustion Science* 34 (2008) 499–550.
- [127] H.G. Wagner, "Some experiments about flame acceleration," Proceedings of the International Specialists Conference on Fuel-Air Explosions, University of Waterloo Press, 1981, 77.

- [128] R. Knystautas, J.H.S. Lee, I.O. Moen, H.G. Wagner, "Direct initiation of spherical detonation by a hot turbulent gas jet," *Proceedings of the Combustion Institute* 17 (1978) 1235–1245.
- [129] A.A. Boni, M. Chapman, J.L. Cook, J.P. Schneyer, "On combustion generated turbulence and transition to detonation," in: L. Kennedy (Ed.), *Turbulent Combustion*, AIAA Reston, VA, 1978, 379.
- [130] S.B. Dorofeev, A.V. Bezmelnitsin, V.P. Sidorov, J.G. Yankin, I.D. Matsukov, "Turbulent jet initiation of detonation in hydrogen–air mixture," Proceedings of the 14th ICDERS, vol. 2, University of Coimbra, Coimbra, Portugal, 1993, D2.4.1–D2.4.10.
- [131] F. Carnasciali, J.H.S. Lee, R. Knystautas, "Turbulent jet initiation of detonation," *Combustion and Flame* 84 (1991) 170–180.
- [132] I.O. Moen, D. Bjerketvedt, A. Jenssen, P.A. Thibault, "Transition to detonation in a large fuel-air cloud," *Combustion and Flame* 61 (1985) 285–291.
- [133] S.P. Medvedev, A.N. Polenov, S.V. Khomik, B.F. Gelfand, "Initiation of upstream-directed detonation induced by the venting of gaseous explosion," *Proceedings of the Combustion Institute* 25 (1994) 73–78.
- [134] J.H.S. Lee, I.O. Moen, "The mechanism of transition from deflagration to detonation in vapor cloud explosions," *Progress in Energy and Combustion Science* 6 (1978) 359–389.
- [135] I.O. Moen, J.H.S. Lee, B.H. Hjertager, K. Fuhre, R.K. Eckhoff, "Pressure development due to turbulent flame propagation in large-scale methane-air explosions," *Combustion and Flame* 47 (1982) 31–52.
- [136] K.L. Cashdollar, I.A. Zlochower, G.M. Green, R.A. Thomas, M. Hertzberg, "Flammability of methane, propane, and hydrogen gases," *Journal of Loss Prevention in the Process Industries* 13 (2000) 327–340.

